Czech Technical University in Prague
Faculty of Mechanical Engineering

Dissertation

Physical Modelling of Combustion Engine Process and Gas Exchange for Real-Time Applications

by

Jan Fortl, M.Sc.

Doctoral Study Programme: *Mechanical Engineering*

Field of study
Machines and Equipment for Transportation

Supervisor
Prof. -Ing. Jan Macek, DrSc

Expert Supervisor
doc. Ing. Oldřich Vítek, Ph.D.

2022 Prague

Abstract

The large majority of gas exchange models used for engine torque control within the Engine Control Unit (ECU) is data oriented. This means that they use look-up tables, or other more sophisticated methods (e.g., neuronal networks), to access calibration data during the engine operation. They require high calibration effort (e.g., in case of look-up tables, complexity is growing exponentially with the number engine actuators) and are usually limited to mean value information on engine stroke events. The use of physical based models is typically not possible due to low CPU performance of costly optimized production ECU's.

This work investigates the possibility to calculate a crank angle resolved, physical based, 1D and 0D thermodynamic engine simulation directly on a serial ECU (240MHz) in real-time. Transient flow in intake and exhaust manifolds, including pressure wave propagation, is described by conservation laws for mass, momentum and energy. Defined set of differential equations is solved by Runge-Kutta integration methods with a fixed time integration step.

A commercial 4-cylinder, turbocharged, spark-ignited engine is used for stationary as well as transient experiments. A detailed 1D model is defined, that satisfies accuracy requirements (e.g., deviation of in-cylinder air mass <5%) in a wide range of operating conditions. Different levels of simplifications between 1D and 0D are assessed in terms of the trade-off accuracy and real-time capability.

Anotace (CZ)

Velká většina modelů výplachu válce používaných pro řízení točivého momentu motoru v rámci řídicí jednotky (ECU) je datově orientovaná. To znamená, že pro přístup ke kalibračním datům během provozu motoru používají vyhledávací tabulky nebo jiné sofistikovanější metody (např. neuronové sítě). Tyto modely vyžadují velké úsilí při kalibraci (např. v případě vyhledávacích tabulek roste složitost exponenciálně s počtem stupňů volnosti motoru) a jsou obvykle omezeny na informace o středních hodnotách. Použití fyzikálních modelů obvykle není možné kvůli nízkému výkonu CPU, používaných v ECU z důvodů nízkých produkčních nákladů.

Tato práce zkoumá možnost výpočtu fyzikálních, termodynamických 1D a 0D simulací přímo na sériovém ECU (240 MHz) v reálném čase. Přechodné proudění v sacím a výfukovém potrubí, včetně šíření tlakové vlny, je popsáno zákony zachování hmoty, hybnosti a energie. Definovaná soustava obyčejných diferenciálních rovnic je řešena integračními metodami Runge-Kutta s fixním časem integračního kroku.

Komerční čtyřválcový, přeplňovaný, zážehový motor je pužit pro stacionární i přechodné experimenty. Je definován podrobný 1D model, který splňuje požadavky na přesnost (např. odchylka hmotnosti vzduchu ve válci < 5 %) v širokém rozsahu provozních podmínek. Různé úrovně zjednodušení mezi 1D a 0D jsou posuzeny z hlediska přesnosti a schopnosti operovat v reálném čase.

Acknowledgements

I would like to thank to my supervisor Prof. Inj. Jan Macek, DrSc, for his patience throw out the years when giving consultations, as well as the ability to provide pragmatic solutions even for complex problems. I also want to thank to Prof. Dr. Josef Kainz who initiated the topics in field of physical-based modelling at Vitesco Technologies in Regensburg, as well as Prof. Dr.-Inj. Fredrik Borchsenius, with whom the cooperation was always very productive and fun. I want to thank Mr. Johannes Beer, the head of Engine Systems, Advanced System Engineering department at the Vitesco Technologies in Regensburg and all colleges for their advice and great technical support. My special acknowledgments go to my wife Eyana for the sacrifice of many long weekends and for her support and encouragement. Finally, I want to thank to the holy spirit, sent by the living God as promised by his only son Jesus, who gives whatever we need and provides inspiration.

Contents

Nomenclature

Variables

u	$\left[\frac{m}{s}\right]$	Flow velocity in x-direction in the middle of cross-section
a	$\left[\frac{m}{s}\right]$	Local speed of sound
p	$[Pa]$	Pressure
ρ	$\left[\frac{kg}{m^3}\right]$	Density
T	$[K]$	Temperature
x	$[m]$	Space coordinate
t	$[s]$	Time
A	$[m^2]$	Cross-section area of pipe (circular)
κ	$[-]$	Specific heat capacity ratio
R	$\left[\frac{J}{kg \cdot K}\right]$	Ideal gas constant
c_p	$\left[\frac{K}{kg \cdot K}\right]$	Specific heat capacity at constant pressure
f_r	$\left[\frac{N}{kg}\right]\left[\frac{m}{s^2}\right]$	Friction force per unit mass
$\dot{q}_H$	$\left[\frac{W}{kg}\right]\left[\frac{m^2}{s^3}\right]$	Heat flux per unit mass
q, q_t, q_x	$[unit]$	General state vector and its partial derivative with respect to time and space
$\dot{q}$	$[unit/s]$	First time derivative of general state vector = change of state rate
Δt	$[s]$	Integration time step
Δx	$[m]$	Space discretization
M	$[kg]$	Mass of gas inside control volume

V	$[m^3]$	Volume
c_S	$[-]$	Stochiometric air-fuel ratio
λ	$[-]$	Air-fuel equivalence ratio
p_{mi}	$[bar]$	Indicated mean effective pressure (IMEP)
x_{RG}	$[-]$	Internal residual gas fraction (iEGR)
W	$[J]$	Mechanical piston work
Q	$[J]$	Heat energy
E	$[J]$	Internal energy
P	$\left[\frac{J}{s}\right]$	Mechanical power
T_q	$[Nm]$	Mechanical torque
$\dot{m}$	$\left[\frac{kg}{s}\right]$	Mass flow rate
h	$\left[\frac{J}{Kg}\right]$	Specific enthalpy
e	$\left[\frac{J}{Kg}\right]$	Specific internal energy
α	$\left[\frac{W}{m^2 \cdot K}\right]$	Heat transfer coefficient
η	$[-]$	Efficiency
μ	$[-]$	(Empirical) flow discharge coefficient
n	$[rpm]$	Rotational speed (engine crank shaft or turbocharger)
ω	$[rad/s]$	Angular speed (engine crank shaft or turbocharger)
φ	$[rad]$	Angular position (engine crank shaft or turbocharger)
d	$\left[\frac{Nm}{rad/s}\right]$	Mechanical damping constant
I	$[kg \cdot m^2]$	Rotational inertia mass

Abbreviations

ECU	Engine control unit
RT	Real-time factor
RMSE	Root mean squared error
PE	Percentage error
FVM	Finite volume method
1D	One-dimensional, the space coordinate refers to the pipe axis
0D	Zero-dimensional
CFL	Courant-Lewy-Friedrichs stability condition
SiL	Software-in-the-loop
HiL	Hardware-in-the-loop

Subscripts

∞	Steady-state
in	Intake
ex	Exhaust
u	Upstream
d	Downstream
Air	Air component of gas fraction
Ab	Air burned – gas fraction
Au	Air unburned – gas fraction
Fb	Fuel burned – gas fraction
Fu	Fuel unburned
1	Position (pressure/temperature) before compressor
2	Position (pressure/temperature) after compressor

3	Position (pressure/temperature) before turbine
4	Position (pressure/temperature) after turbine
t, e. g. p_{1t}	Total (stagnation) pressure
s, e. g. Δh_{sC}	Isentropic state change, for example the isentropic compressor enthalpy difference
C	Compressor stage
T	Turbine stage
TC	Turbocharger

Introduction

For spark ignited engines, torque control is realized in the Engine Control Unit (ECU) by managing the cylinder charge exchange, while keeping the air-fuel ratio stoichiometric in order to minimize exhaust emissions [1] [2]. For this purpose, the ECU needs a real-time capable model, giving an accurate prediction on the in-cylinder air mass based on current sensor information.

During the development of engine as a mechatronic system, requirements on short development cycles, lowering of production and calibration costs as well as high requirements on quality must be balanced. From the modelling perspective, it follows that different configurations (degrees of freedom) of gas exchange systems have to be covered in a restricted period of time. Therefore, smart solutions, as well as modularity and adjustability of modelled subsystems play a key role in the development process to meet future CO_2 legislations.

In principle, there are two modelling strategies: 1. data driven models and 2. physical models [3]. Data driven models start from the result, typically approximated measured or simulated data, directly accessed from the memory. On the other hand, physical models rely on fundamental physical laws and natural constants. The level of used physical description for the application is usually in conflict with the runtime performance. In practice, a suitable compromise between model complexity and the storage of calibration data must be found. Kainz [4] introduced at least four limiting criteria for the purpose of ECU model implementation:

1. Model quality (e.g., accuracy)
2. Calibration effort (e.g., number of data samples from measurements)
3. Calibration storage memory (ROM)
4. Real-time capability (limited by processor (CPU) performance)

The simplest example of data driven models are look-up tables, which are very efficient in a view of CPU performance. These modelling methods (combined with semiempirical mean value models) are widely used in today's ECUs. However, the memory used is increasing exponentially with the number of model inputs (e.g., engine actuators). This resulted in the development of polynomial approximation models and neural networks (e.g., LMN [5], LOLIMOT [6] [4]). These are typically integrated within a calibration tool chain to be trained with experimental data and/or data obtained from sophisticated simulation tools.

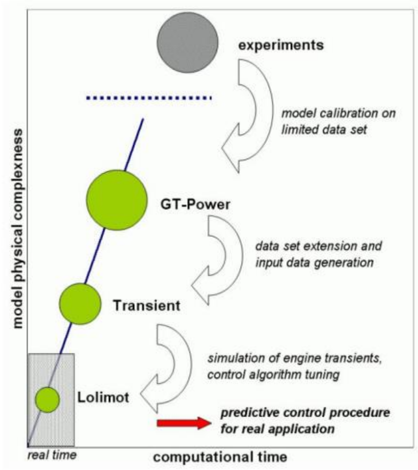

Fig. 1 Example of workflow used for calibration of LOLIMOT (Local Linear Model Network) model used for real-time engine control [6]

Neuronal network models have become widely popular in the last couple of years, especially due to their robustness and applicability of similar structures to completely different problems solved. Nevertheless, they remain still being data driven models, and therefore, require high calibration effort. Monte-Carlo methods can be used to avoid a factorial combinations of needed parameter combinations to provide the training data, yet the needed datasets are typically high (10^4 < combinations). Beside this, each input and output have to be modelled individually. When a modelled variable is missing in the training data set, whole tool chain must be repeated. The memory used by the neuronal network models is not growing exponentially with the number of inputs as it is the case of look-up tables but

One way to overcome the limitation of data driven models is the use of physical models describing the engine and gas exchange processes based on the solution of differential equations during engine operation (Rösler 2013 [7], Ludwig 2011 [8], Friedrich 2008 [9]). The main challenge for physical based models is the reaching of real-time capability on given hardware due to low CPU performance of state-of-art production ECU’s. This relates to another problem when using physical based models: to find an appropriate level of model detail (complexity) to balance real-time performance with accuracy objectives, while keeping the calibration effort low.

This work deals with thermodynamic 1D an 0D modelling methods, suitable for crank angle resolved, real-time capable simulations of engine and gas exchange process. As a validation platform, a commercial turbocharged spark ignited (SI) engine is used. The newly developed physical based model is intended to replace/enhance older prediction models used for control purpose by Vitesco Technologies.

Chosen methodology can cover different engine configurations due to its modular structure. Main model outputs are the in-cylinder air and residual gas mass fractions for each single combustion event in addition to the states of the gas exchange system such as the exhaust back pressure and the turbocharger rotational speed. The knowledge of the in-cylinder state for each single combustion event allows a more efficient and emission optimized process control of the engine. For example, the ignition angle set point can be pre-controlled in a more accurate way based on the knowledge of the in-cylinder air mass.

1 Critical Literature Research

1.1 State-of-the-art RT Applications

Coarse History - Publications

The history of automotive real-time tools starts in the 1980s with interpolation map-based models, improved during the 1990s to data based and semi-physical real-time tools [8] [10]. Around 2000, there started the use of neuronal networks and simple physical based models [8] (semi-physical or grey-box models). The work of Friedrich [9] from 2008 presents a fully physical 0D engine model (with simple 1D approach in intake manifold) and demonstrates its advantages for real-time ECU calibration on a Hardware-in-the-Loop (HiL) test bench. A similar model detail is in the SAE 2009-01-0589 [11] from 2009, where the authors compare 0D simulation of stationary and transient operation with 1D offline calculated results. The work of Ludwig [8] from 2011 focuses on the detailed modelling of 1D gas dynamic effects. As a reference he uses Ricardo WAVE software and implements several discretization methods (Law-Wendroff, Roe's scheme, Quasi-Propagatory-Method) to compare charge-exchange calculation results and real-time performance on a HiL testbench. The work of Jakovlev [12] from 2014 uses a simple real-time 0D model coupled with a friction model and simulates cold start and low engine torque operation conditions. In 2020, interesting research in field of ICE engines for the both Automotive and Marine industry was published (Engine Modeling and Simulation [3]). The International Society for Energy, Environment and Sustainability (ISEES) founded at the Indian Institute of Technology Kanpur, India, coordinates research activities in field of ICE engines. As a part of the multinational research activities, a chapter ([3], Chapter 6. Physical and Data-Driven Models Hybridisation for Modelling the Dynamic State of a Four-Stroke Marine Diesel Engine, provided by Department of Maritime and Transport Technology, Delft University of Technology, and other institutes for Marine Engineering) was published, giving a summarizing overview on available data driven models and physical models with the objective to find an appropriate compromise for practical use in industrial applications.

Commercial RT Applications

There are several commercial black-box models available for the ICE engine simulations that provide real-time capable solutions suitable for SiL and HiL applications. Well established are

- Wave RT (https://ricardo.com/)
- GT-Power RT (https://www.gtisoft.com/)
- Simcenter AMESim (https://www.plm.automation.siemens.com)

Alternatively,

- DYNA THEMOS (www.tesis.de)

provides solutions focused more directly for the purpose of RT applications.

The main advantage of these tools is that they provide ready-to-use libraries for different levels of physical complexity. For example, results provided by 3D CFD simulations are used for dimensionless parametrization of complex 1D engine and gas exchange models, that are further simplified to fast-running 0D models and finally used for a HiL simulation or calibration of RT control-oriented models (see also example of toolchain in Fig. 1 [6] or [13]).

First in 2013 [14], and later in 2015 [15] and 2018 in an extended form [16], Ricardo presented real-time capable 1D engine application. The Ricardo software Wave RT was used to generate C-code via defined MATLAB/Simulink interface. The rapid prototyping hardware platform rCube2 (based Infineon 2 core processors with 150 MHz internal clock frequency) was used for HiL simulation to calibrate a diesel engine ECU and improve emissions [14].

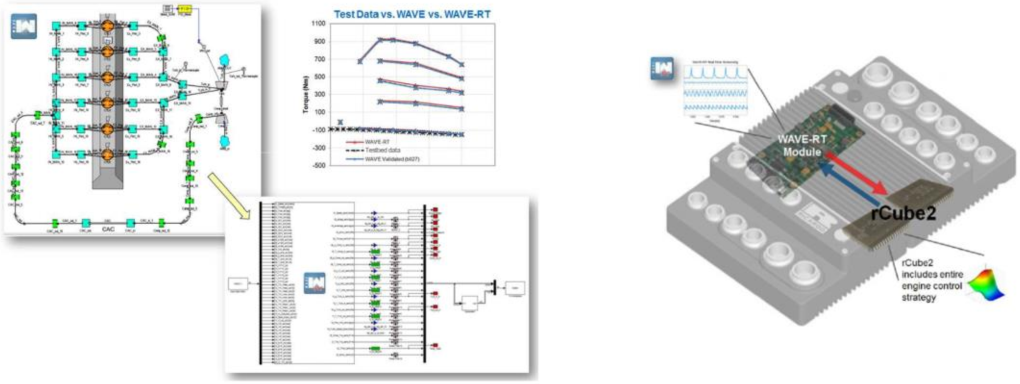

Fig. 2 Example of Wave RT user interface, used for application of 1D engine simulation, runed on rCube2 with two core processor 150MHz clock [14]

One of the most widely used engine simulation tools is the GT-Power provided by Gamma Technologies Inc. GT-Power provides bride solutions from the possibility of co-simulation with 3D over different complexities of detailed 1D engine and gas exchange models to simplifications leading to fast-running 0D models, mean value models and finally the fastest map-based models. One example of RT application was presented in by Fiat Chrysler in SIA paper 2014 [17]. A detailed 1D model, previously used for engine performance an emission optimization (thus widely validated) was simplified to a fast-running 0D model (see Fig. 3). The fast-running 0D model was used for real-time HiL simulations with the objective to calibrate an ECU of a diesel engine. As a hardware platform, dSpace Autobox with a four cores processor 2.8GHz was used.

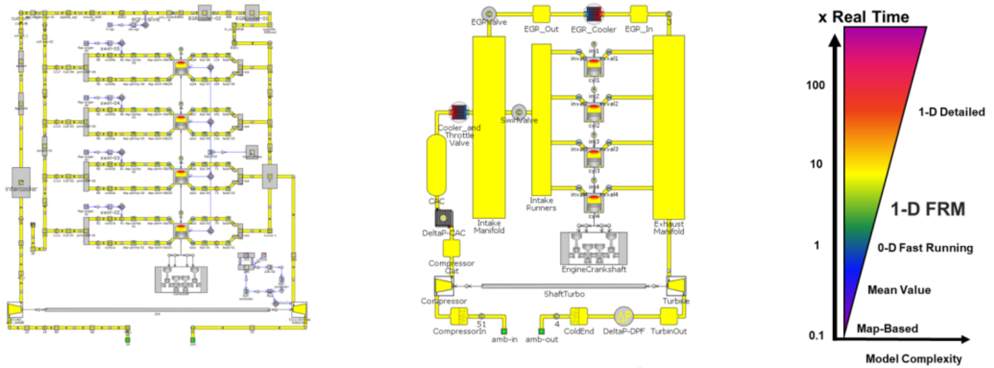

GT-SUITE detailed 1D engine model (191 subvolumes)

GT-SUITE engine FRM after simplification (17 subvolumes)

Fig. 3 Example of GT-Power user interface, simplification of 1D detailed model to a fully-physical 0D fast-running engine model (solver steps from 0.5ms to 4ms), runed on dSpace DS1006QDC with four cores processor 2.8GHz clock [17]

Another feature provided by GT-Power is the possibility to implement physical fast-running models in MATLAB/Simulink as an S-function, giving a transient response to defined input. These are then used to calibrate Mean Value Models by the use of MATLAB’s System Identification Toolbox. This procedure is also known as model-based calibration in the automotive industry [10]. Another examples of tool chins using GT-Power in real time applications, using S-Functions for MiL/SiL/HiL and ECU co-simulation or calibrating Neural Networks, are SAE 2013-01-1120 [18], SAE 2009-01-0695 [19], SAE 2005-01-0072 [20], SAE 2000-01-0934 [21].

Simcenter AMESim provides as a part of standardized solution Physical based, crank angle resolved 1D/0D models of air-path system with the possibility of simplification to 0 Mean Value Models and further Map-based engine models [22].

Last example to be mentioned is the German company TESIS that offers software tool named DYNA, which is a MATLAB/Simulink based package library for simulation of combustion engines with focus on control development. In 2007, there started a cooperation with Technical University of Berlin (Friedrich [9]) with focus on crank angle resolved engine simulation resulting in a new software package DYNA THEMOS. The research was focused on optimization of control strategies for standardized driving cycles. Friedrich used originally the simplest Euler explicit integration method for fast-running 0D simulations. In 2013, Roesler [7] improves this method using a physical based approach for orifice stabilization (keyword ‘Propfenmodel’). As a result, using Euler explicit integration with time step could be increased to 10^{-4}s, which lead to reduction of computing time. The modular approach of THEMOS engine components is real-time capable on dSPACE HiL platforms. A CAN interface is used for communication and calibration of ECU’s.

One disadvantage of the commercial engine tools to be mentioned are the high licence costs. Another typical issue is the fact that as a black-box solution, only already available libraries can be used with restricted possibility for user defined library extensions for the particular application.

1.2 Transient Flow in ICE Engine Duct Systems

Transient fluid dynamics phenomena in engine duct systems represents the most demanding part of the numerical solution, mainly due to Courant stability condition when momentum conservation is considered (in 1D simulations). There have been considerable efforts to find computationally effective numerical methods [23] [24] [25] [26] [27] [28].

Pischinger [29] defines governing equations with general validity for unsteady, non-homentropic flow including fluid friction (viscosity influence) and provides both discretization possibilities together with practical engine applications.

continuity equation – mass conservation

$$\frac{\partial\rho}{\partial t}+\rho\frac{\partial u}{\partial x}+u\frac{\partial\rho}{\partial x}+\frac{\rho u}{A}\frac{dA}{dx}=0 \tag{1.1}$$

momentum equation

$$\frac{\partial u}{\partial t}+u\frac{\partial u}{\partial x}+\frac{1}{\rho}\frac{\partial p}{\partial x}+f_r=0 \tag{1.2}$$

energy equation (assumption of ideal gas)

$$\frac{\partial p}{\partial t}+u\frac{\partial p}{\partial x}-a^2\left(\frac{\partial\rho}{\partial t}+u\frac{\partial\rho}{\partial x}\right)-(\kappa-1)(\dot{q}_H+uf_r)\rho=0 \tag{1.3}$$

From a mathematical point of view, these are 1D hyperbolic conservation laws, usually written in a more compact matrix form [30] [31]:

$$q_t+f(q_x)=s \tag{1.4}$$

, where q is a state vector with defining density, velocity and energy states or some substitutions of them (see also equation 3.56 in for the particular application, also known as the Euler equations in one space dimension).

The strongest possible simplifications that come into consideration can be done according to the acoustic theory [29]

Continuity equation (Acoustics)

$$\frac{\partial\rho}{\partial t}+\rho_0\frac{\partial u}{\partial x}=0 \tag{1.5}$$

Momentum equation (Acoustics)

$$\rho_0\frac{\partial u}{\partial t}+\frac{1}{\rho}\frac{\partial p}{\partial x}=0 \tag{1.6}$$

Energy equation (Acoustics) - definition of speed of sound

$$a_0=\sqrt{\kappa\cdot R\cdot T_0} \tag{1.7}$$

These linearized equations are suitable for systems, where only small pressure pulsations occur. Thermal effects are also neglected.

An example of the use of acoustic theory in real-time software applications is in Friedrich [9], used within the above mentioned HiL simulations based on THEMOS DYNA development activities.

For the given systems of governing 1D hyperbolic conservation laws, there exist a variety of numerical methods, using different discretization for time and space domain. Some methods are restricted by assuming different levels of simplifications (somewhere between the full system (1.1) (1.2) (1.3) and linearized equations (1.5) (1.6) (1.7)). One example of such method is the Method of Characteristics (MOC), known since the 1970s as a graphical procedure. The applications of MOC on engine duct systems are also shown in Pischinger [29]. The basic restrictions of MOC are frictionless + adiabatic (homentropic) flow with constant gas properties.

An interesting extension of MOC is the Quasi-Propagatory method (QPM), used by the commercial software Ricardo Wave. The first publication of QPM appeared in ASME Paper by Cipollone & Sciarretta in 1999 [23] and then in SAE 2001-01-0579 [25]. The method was later implemented and tested by some other authors [32] [26], with more or less success. Gustavsson published in 2014 even a source code implementation based on Madelica open-source software [32], but only as a single pipe test without solution of boundary conditions. Ludwig [8] compared in 2011 three methods applied on a steady-state engine operating conditions: 1. Quasi-Propagatory method, 2. Lax-Wendorff method, 3. Roe’s scheme. The result was, that the Roe’s scheme and Lax-Wendorff gave stable and accurate results, while the QPM provided strange errors. Unfortunately, the problem is that such comparison always depones not only on the method itself, but also on the level of understanding end resulting quality of code implementation.

According to Pischinger [29], Finite Difference Method (FDM), for example the Lax-Wendorff differential scheme, is more suitable than MOC because it does not need an iterative estimation of local correct states at element boundaries in every time step. The basic idea of FDM is to transform governing Partial Differential Equations, using suitable discretization of the flow field, into discretized equations. The resulting algebraic equation system can be resolved using a sequence of purely arithmetic operations.

There are also some exotic methods like Method of Transfer Functions (MTF), where the flow is modeled in analogy with electrical phenomena and the equations are solved using the Laplace transformation. MTF method was invented in 2008 (SAE 2008-01-2389 [33]) by the same author like the previously mentioned used QPM, also used by Ricardo Wave.

Besides these above-mentioned methods, the standard solution of governing conservation laws in form of PDE's describing the 1D hyperbolic conservation laws is the Finite-Volume-Method. Among CFD books to this topic, Randall J. LeVeque [31] is very useful for understanding and Pieter Wesseling provides both theory in connection with runnable MATLAB codes [30]. The Sod's shock tube problem is provided (for free) by Wesseling in form of a runnable source code as an example for the numerical solution for the discontinuous Riemann problem (see also section 3.4.4). The Riemann problem, defined on the discretization grid as an initial value problem, is a well-established test case for numerical methods solving the 1D pressure wave propagation. For the Riemann problem, the Riemann solvers were invented. Riemann solvers, also known as the Godunov type methods show stability benefits when compared with standard discretization shames (because they assume a discontinuity at each element boundary and contain its analytical solution). Among Riemann-type solvers, the Roe's scheme (also tested by Ludwig [8] in THEMOS DYNA) is very popular. The Roe's shame assumes that the flux-terms in (1.4) can be linearized as follows [30]:

$$q_t + A \cdot q_x = s \tag{1.8}$$

, where A is the so-called Roe's matrix (see also linearized equations (3.59)). Roe also provided an approximation to obtain matrix A for the set of governing equations (1.1) (1.2) (1.3) on a given grid.

For the purpose of this work, the Final-Volume-Method is used for the solution of 1D flow in engine manifolds. The upwind discretization scheme is used as a standard discretization method applied on the full set of governing equations (section 3.4.1). Later, simplifications according to acoustic theory are assumed and solved with the Godunov method (which is identical with Roe's scheme in case of already linearized matrix A, see section 3.4.2).

More details on the assumed simplifications and differential schemes used to transform governing equations into set of ODE’s, later solved by standard Runge-Kutta methods, are shown in Appendix – Theory page 106 – 111.

To improve the text readability, main parts of the literature research were put directly next to the particular application in the next sections.

2 Objective

Based on the literature research, the large majority of physical based real-time engine applications is used to calibrate data-oriented control models (look-up tables, neuronal networks etc.) used then for the purpose of the engine control during operation [6] [34] [7] [9] [8] [12] [17] [20]. With some exceptions like Ricardo Wave software [16], which is a commercial black-box model, there are no available codes with a potential to be real-time capable on an engine production ECU that has usually a restricted processor performance due to manufacturing costs. Most real-time applications using thermodynamic engine models require specialized HiL hardware like dSpace with high processor performance (e.g., CPU > 1GHz). There is also no available work that would transparently show the structure of computational effort (e.g., CPU load) of individual model components or modules.

The objective of this work is to

- create a physical model, based on differential equations, yielding detailed, crank angle resolved information on engine in-cylinder gas mixture and charge exchange including performance of a turbocharger, suitable for predictive model-based control of a turbocharged ICE. The model has to be real-time capable on a state-of-the-art production ECU. Required model calibration data should be less demanding than standard data-based models.

The simulations should be validated with steady-state and transient engine measurements to assure required model accuracy and information on engine process like comparable commercial engine codes.

As an accuracy criterion,

- the commonly used fresh in-cylinder charge should be compared to measurements to achieve deviations lower than 5% within the entire engine operation range of a state-of-art turbocharged four-cylinder SI engine

As a target hardware,

- a state-of-art production three core ECU with 240MHz processor clock should be used. Only one core is intended for the model calculation (solution of differential equations in real-time).

To keep the general validity of proposed models (physical based description) as high as possible,

- only global calibration parameters, valid as a single constant for the entire engine operating range should be used. As far as application allows, only generally valid natural constants and physically interpretable parameters derived from geometry, or standardized component measurements should be used for the model calibration.

Besides the air-mass as a validation criterion for model accuracy, other engine performance indicators as well as engine measurements of pressures and temperatures should be used for model validation. Especially the high-sampled intake and exhaust manifold pressures should be used to match transient pressure wave propagation effects.

Because of the fact, that the transient 1D pressure propagation phenomena is the most time-consuming part of the numerical solution, but crucial aspect of the engines filling behaviour, it should be considered first. Theoretical real-time performance on target hardware should be assessed and shown in a transparent manner. The model should then be simplified to allow the real-time capability, but keeping the accuracy and inherited features from the detailed model at a reasonable level.

3 Theory, Basic Physical Assumptions

3.1 Numerical Solver

The numerical solver is supposed to predict behaviour of the engine gas exchange system and its control in near future. A system can be classified in the theory of signal processing to either static or dynamic. Static systems are memory-less because the system output is only dependent upon the present input. On the other hand, the dynamic system requires memory because the output depends also on passed values. Typically, this memory manifests in form of an internal state. This state changes on a specific rate which depends on the state itself and the inputs. This property is crucial for the numerical solution in real-time because in comparison to dynamic systems, static systems usually require very low computation time. Therefore, dynamic the behaviour is limiting for real-time applications. From the modelling perspective, the whole engine is divided into components to enable a modular composition with two kinds of components:

- **Static:** signal components (just functional relations, no change of gas state)
- **Dynamic:** thermodynamic components (have change of gas state)

Static signal components represent signal sources or functional relations, for example constant boundary conditions. Thermodynamic engine components such as cylinders, valves, pipes or manifolds are defined individually by sets of ‘Ordinary Differential Equations’ (ODEs). From the mathematical point view, the system is formulated as an initial value problem.

State vector:
(example: pressure, density, velocity, temperature)

$$q = q(t) = (q_1, q_2, \dots, q_n), with\ n\ variables \quad \textbf{(3.9)}$$

Problem formulation:
(evaluation of ODEs)

$$\dot{q} = f_{ODE}(t, q) \quad \textbf{(3.10)}$$

Problem solution:
(example: Euler/Heun)

$$q(t) = \int_0^{tEnd} \dot{q}\, dt \quad \textbf{(3.11)}$$

Each of the thermodynamic components is described by a set of state variables like pressure, density, etc. that may change in time. All these variables are stored into one single state vector (equation (3.9)) with n degrees of freedom. The terminology for ‘degrees of freedom’ for a differential equation system collides with engine actuator ‘degrees of freedom’ used in automotive context (see course of dimensionality in Chapter 0-Intro, Kainz [5] [4]). Because of this fact, integer number n is used to count the number of calculated ordinary differential equations (which is identical with number of its degrees of freedom). For example, a system with thermodynamic volume connected to simple acoustic pipe with 2 elements and constant boundary condition (Fig. 4) is described by a system of eight ordinary differential equations $n = 8\ ODEs$.

The initial value problem is formulated in the simulation code according to equation (3.10) with the function f_{ODE}. Function input is the current time t and the current state vector q from which the code obtains a time derivative of state $\dot{q}$. The current state vector must be composed from individual engine components, containing the description of physical conservation laws. The problem is that the gas state of one component depends on its neighbours, thus has variable boundary conditions. For instance, q_{Volume} in Fig. 1 depends on q_{Pipe} and vice versa. In a causal modelling approach [35] the inputs of one component are linked to the outputs of another by means of either an identity relation (e.g., pressure) or conservation laws (e.g., mass flow). This communication happens via uniformly defined input and outputs on component ports.

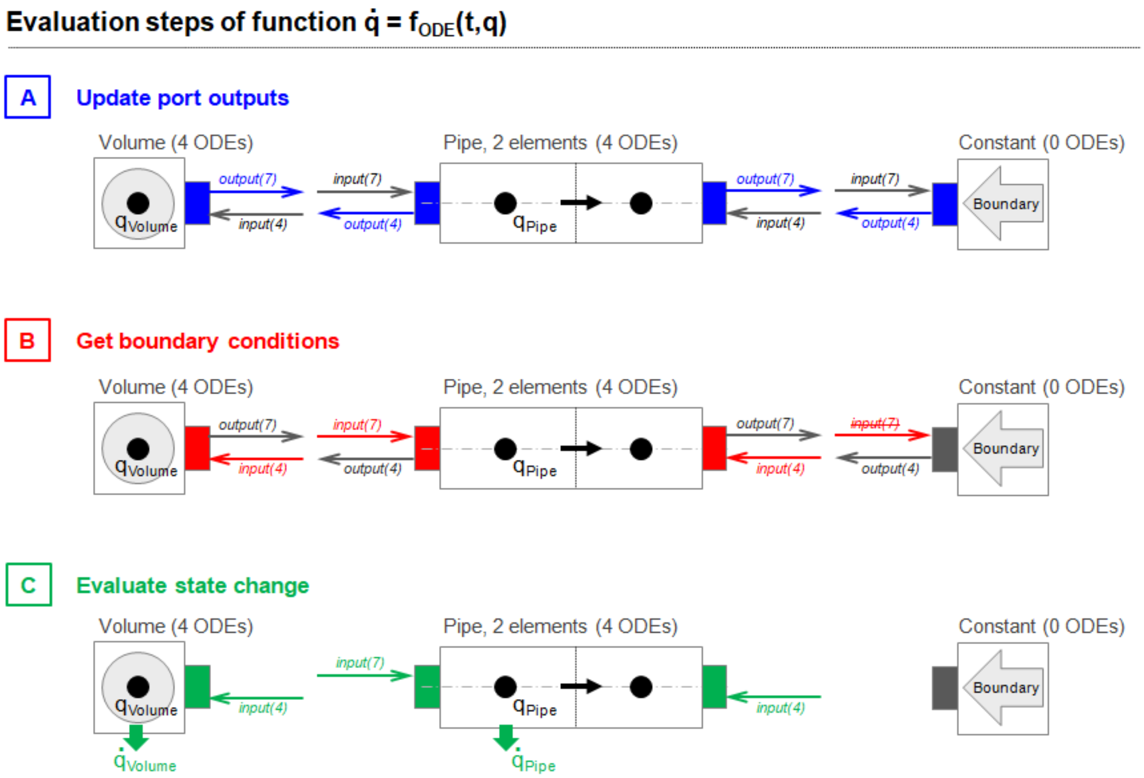

Fig. 4 Evaluation steps of function f$_{ODE}$ containing ordinary differential equations of each component and three steps (A, B, C) using causal modelling technique for ports communication

For example, a system with three components in Fig. 4 is represented by state vector $q = (q_{Volume}, q_{Pipe})$. Let's assume that we know current state from previous iteration. Then function f_{ODE} is evaluated in three steps:

A. **Update port outputs** $q\ \&\ inputs^{OLD} \rightarrow outputs^{NEW}$

B. **Get boundary conditions** $inputs^{NEW} \equiv outputs^{NEW}$
$q\ \&\ inputs^{NEW} \rightarrow\ boundary\ conditions^{NEW}$

C. **Evaluate state change rate** $q\ \&\ boundary\ conditions^{NEW} \rightarrow \dot{q}$

In the step A., each component has to deliver uniform outputs at communication ports based on the current state and the old inputs from their neighbour (boundary) elements. According to causal condition in B., current inputs correspond exactly to complementary neighbour components. From uniform inputs at current time, component specific boundary conditions (non-uniform) can be calculated. Finally, the most processor time consuming evaluation of state change C. is delivered.

When the function f_{ODE} is able to deliver $\dot{q}$ at any time step, the initial value problem can be resolved in time as stated in equation (3.11). This is in particular done by the Heun integration scheme, which is a 2nd order explicit Runge-Kutta integration method. At adequate step size because of being of order 2, Heun comes with significant better approximate behaviour compared to Euler method while having quite low computational cost: it is still explicit and needs only two evaluations of f_{ODE} per time step. For programming purpose, the Heun's integration is rewritten into four straight-forward expressions:

1. **Evaluation of ODEs at present time (including A. B. C.)** $$\dot{q}_{pre}^{k} = f_{ODE}(t, q^{k}) \qquad \textbf{(3.12)}$$
2. **Predictor step (Euler)** $$q_{pre}^{k+1} = q^{k} + \Delta t \cdot \dot{q}_{pre}^{k} \qquad \textbf{(3.13)}$$
3. **Evaluation of ODEs at future time (including A. B. C.)** $$\dot{q}_{corr}^{k+1} = f_{ODE}\left(t + \Delta t, q_{pre}^{k+1}\right) \qquad \textbf{(3.14)}$$
4. **Corrector step (Heun)** $$q^{k+1} = q^{k} + \frac{\Delta t}{2} \cdot \left(\dot{q}_{pre}^{k} + \dot{q}_{Corr}^{k+1}\right) \qquad \textbf{(3.15)}$$

The numerical solver uses a constant time step Δt to integrate conservation laws for mass, momentum and energy, formulated in each component. The integration time step is usually kept as high as possible in real-time applications because it directly affects the number of computational operations per second and therefore the necessary computing time (see section 5.6). Solution of the momentum equation in engine pipe systems has to satisfy Courant-Friedrichs-Lewi (CFL) [29] [31] stability condition.

Courant-Friedrich-Lewi stability condition

$$\frac{(a+|u|)\cdot\Delta t}{\Delta x} < 1 \qquad \textbf{(3.16)}$$

For this reason, the integration time step is often limited to some maximum stable value when pipe components are used. On the other hand, other components would remain stable even with a significantly higher time step. To overcome this problem, a global integration procedure is defined for all components (see Fig. 5, Left), but selected pipe components are resolved with a local pipe integration algorithm (see Fig. 5, Right). To remain stable, pipe components being limited by short length or high local speed of sound due to high gas temperature use locally different (smaller) integration time step than pipe components with propitiatory conditions:

Local pipe integration time step

$$\Delta t_{pipe} = \frac{\Delta t}{dtPipeFak} \ , dtPipeFak \in N \tag{3.17}$$

Fig. 5 shows a graphical representation of the Heun’s integration (steps 1. 2. 3. 4. described with equations (3.12) to (3.15)). At the current time with index k, component boundary conditions are updated at the ports (steps A. B.) before evaluating all differential equations to do a predictor step (step C.). Then the boundary conditions are evaluated once again (steps A. B.) to fulfil a corrector step (step C.). When the local pipe integration is active, the local solver overtakes integration of pipe states in vector q_{Pipe}^{k} until the final time is almost reached. For example, with $\Delta t_{pipe} = \frac{\Delta t}{4}$, local solver evaluates 3 integrations and delivers the state q_{Pipe}^{k+3}. The final integration time step of pipe q_{Pipe}^{k} together with all other component states is then executed by the global integration solver. During the local integration, the boundary conditions are assumed to be constant, so as only evaluation of step C. is necessary (but not A. and B.). This simplification is theoretically not correct, since the component specific boundary conditions also depend on changed pipe state, but solver tests on engine model showed that there is no significant difference in solution when keeping boundaries constant during local integration.

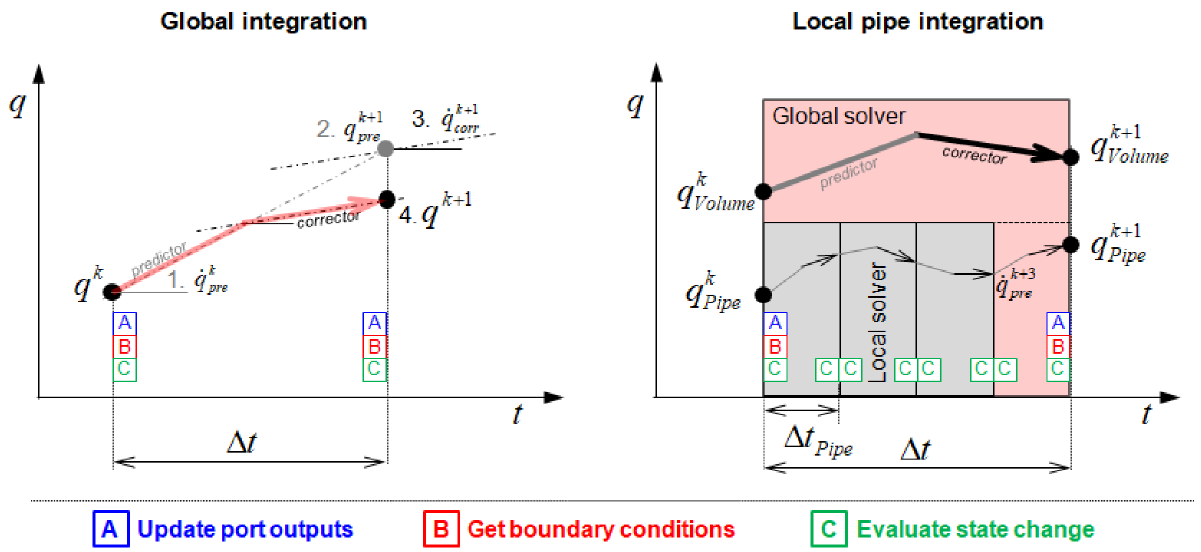

Fig. 5 Left: Principle of implemented Heun's integration method with components communication on ports specified in steps A, B and C
Right: Locally different (smaller) integration time step used to avoid instability of pipes due to high CFL numbers in real-time applications

An important aspect of the solver to be mentioned is that both the global and local solvers still allocate hardware memory of one single state vector for all differential equations (see definition in equation (3.9)), so as minimum hardware memory is needed.

3.2 Engine Process Simulation

Fundamentals of the gas exchange process described in Heywood [36], Merker [1] and Pischinger [29] are applied to the four-stroke cycle engine, including scavenging effects. The purpose of the exhaust and inlet processes is to remove the burned gasses at the end of the power stroke and admit the fresh charge for the next cycle. The indicated power of an internal combustion engine at a given speed is proportional to the mass flow rate of air (Haywood [36] chapter 6). Thus, prediction of trapped in-cylinder air mass is the primary goal of a gas exchange simulation.

In a spark-ignited engine, the intake system typically consists of an air-filter, a throttle, optionally fuel injectors in each individual intake ports, and intake manifold. During the induction process, pressure losses occur as the mixture passes throw and by each of these components. There is an additional pressure drop across the intake port and valve. The exhaust system typically consists of an exhaust manifold, exhaust pipe, often a catalytic converter for emission control, and a muffler or silencer [36]. Fig. 3 illustrates the intake and exhaust gas flow process in a conventional spark-ignition engine. These flows are pulsating.

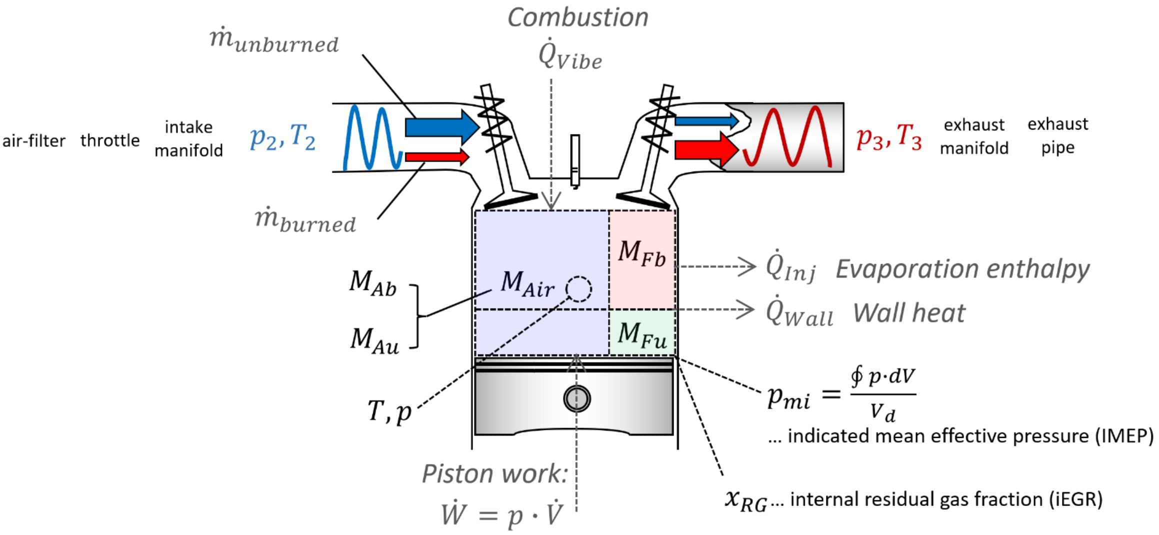

Fig. 6 Principle of gas exchange process, definitions of air-fuel composition and energy flow of the two-zone combustion model

The gas mixture is assumed to be composed by three specie components in the simulation. The air, burned fuel and unburned fuel:

$$M = M_{Air} + M_{Fb} + M_{Fu} \tag{3.18}$$

A so called two-zone model is assumed for engine cylinders, converting the unburned zone into a burned zone during combustion. Each zone is spatially homogeneous, separated by a massless and infinitesimally thin flame, and no heat transfer takes place between the two zones [3]. For the purpose of fast-running simulations, the only the fuel is divided into burned and unburned fraction within the model (being an integrated state variable). Assumed to be in the same ratio like the burned-fuel and unburned-fuel fractions, the burned and unburned air-mass is then obtained during postprocessing

$$M_{Au} = M_{Air} - c_S \cdot M_{Fb} \tag{3.19}$$

, while using of the stochiometric air-fuel ratio $c_S = 14$ obtained from fuel measurements.

Besides the masses defining a gas mixture, temperature is used as a thermodynamic state variable (see T in Fig. 6). It is assumed that all gas fractions are distributed homogenously and have therefore an equal temperature [1].

With the masses and the temperature, the thermodynamic gas state is already fully defined. Density is then obtained by its definition

$$\rho = \frac{M_{Air} + M_{Fb} + M_{Fu}}{V} \tag{3.20}$$

and (total) pressure results from the assumption of an ideal gas equation.

$$p_t = \frac{\left((M_{Air} + M_{Fb}) \cdot R_{gas} + M_{Fu} \cdot R_{fuel}\right) \cdot T}{V} \tag{3.21}$$

The overall engine operation parameters of greatest interest which can be determined from a thermodynamic analysis of the engine operating cycle are among others the indicated mean effective pressure (IMEP) [36]

$$p_{mi} = \frac{\oint p_{cyl} \cdot dV}{V_d} \tag{3.22}$$

And the internal residual gas fraction (iEGR) [36] [1]

$$x_{RG} = \frac{M_{Fb} \cdot (c_S + 1)}{M} \tag{3.23}$$

Both the p_{mi} and the x_{RG} are obtained from the cylinder thermodynamic states during the engine simulation.

These overall parameters depend on the design of the engine subsystems such as manifolds, valves and ports, as well as engine operating conditions. The individual engine components are modelled with the causal modelling technique already described in the section 3.1.

3.2.1 Thermodynamic Volumes

The control volumes are modelled by using of the open thermodynamic system concept (useful theory is Heywood [36], Merker [1] or Avinash [3], applications in context of real-time applications were described in Friedrich [9], Ludwig [8] or Rösler [7]). Momentum conservation is not considered, thus, the model is classified as 0D.

The volume model consists of together 4 ODEs. Following boundary conditions are used:

- Inputs: $\dot{m}_i$, T_{up} … mass flow (air, burned-fuel, unburned-fuel), ups. temp.
- Outputs: M_{Air} , M_{Fb} , M_{Fu} , T … three mass fractions, temperature

Control volumes are considered as cylindrical solenoids, thus neglecting dissociation effects and the kinetic energy of the flows entering/exiting the receivers [3]. The change of masses is then modelled with the mass conservation law (3 ODEs).

$$\frac{d}{dt}\begin{pmatrix} M_{Air} \\ M_{Fb} \\ M_{Fu} \end{pmatrix} = \begin{pmatrix} \Sigma\, \dot{m}_{Air,i} \\ \Sigma\, \dot{m}_{Fb,i} \\ \Sigma\, \dot{m}_{Fu,i} \end{pmatrix} \tag{3.24}$$

Inflowing masses are positive, outflowing masses negative. The mass flows are calculated in the connected (other) components and transferred to this component via the ports. Connecting of multiple mass flows (for example inlet and outlet, or 4 inlet ports connected to one intake manifold) is possible, the subscripts “i” refers to each of the mass flow stream. Note that the mass rate of change does not need to be integrated since it only represents the difference between entering and exiting mass flow rates.

The energy conservation law (without thermodynamic work)

$$\frac{dE}{dt} = \sum \dot{m}_i \cdot h_i + Q \tag{3.25}$$

gets the form

$$\begin{aligned} &\frac{d}{dt}\Big((M_{Air} + M_{Fb}) \cdot e_{gas} + M_{Fu} \cdot e_{fuel}\Big) \\ &\qquad = \sum \big(\dot{m}_{Air,i} + \dot{m}_{Fb,i}\big) \cdot h_{gas,i} + \sum \dot{m}_{Fu,i} \cdot h_{fuel,i} - Q_{Wall} \end{aligned} \tag{3.26}$$

The specific internal energy end enthalpy is assumed to be a gas property, dependent on the temperature and richness factor [37].

$$\begin{aligned} e_{gas} &= e(T,\ l_i) \\ h_{gas} &= h(T,\ l_i) \qquad \textit{with} \qquad l_i = \tfrac{1}{\lambda} \end{aligned} \tag{3.27}$$

with the burned air-fuel ratio

$$\lambda = \frac{M_{Air}}{c_S \cdot M_{Fb}} \tag{3.28}$$

Specific enthalpies h_i in equation (3.26) are always evaluated upstream. The derivative of the energy conservation law yields a differential equation (1 ODE) for the temperature coupled with the derivatives of the masses. The mass derivatives can be eliminated using mass conservation laws.

The functional dependence of used gas properties is based on polynomial approximations of data published by Grill 2006 [37] (see Fig. 54 in Appendix - Theory).

3.2.2 Engine Cylinders

The cylinder volume is an extension of previously described thermodynamic volume model. Geometrical displacement volume is defined as function of crank angle. The model is described by mass and energy conservation (without momentum), is therefore classified as 0D two-zone model [1]. The cylinder model consists of together 4 ODEs. Following boundary conditions are used:

- Inputs: $\dot{m}_{in,i}$, $\dot{m}_{ex,i}$, $\dot{m}_{inj}$, $T_{up,in}$, $T_{up,ex}$, φ_{crk} , N_{eng}
- Outputs: M_{Air} , M_{Fb} , M_{Fu} , T … three mass fractions, temperature

For the in-cylinder process, apart from the assumptions on the working medium described before, valve leakage and blow-by is further neglected. Furthermore, the temperatures at the cylinder wall T_{Wall} (mean value of cylinder piston wall and head temperature), as well as the injected fuel temperature T_{inj} are considered all uniform and constant.

The conservation laws for masses are (3 ODEs):

$$\frac{d}{dt}\begin{pmatrix} M_{Air} \\ M_{Fb} \\ M_{Fu} \end{pmatrix} = \begin{pmatrix} \dot{m}_{Air,in} - \dot{m}_{Air,ex} \\ \dot{m}_{Fb,in} - \dot{m}_{Fb,ex} + \dot{m}_{Vibe} \\ \dot{m}_{Fu,in} - \dot{m}_{Fu,ex} + \dot{m}_{inj} - \dot{m}_{Vibe} \end{pmatrix} \qquad \textbf{(3.29)}$$

The combustion mass transfer $\dot{m}_{Vibe}$ is calculated using Vibe combustion model as described in literature [29] [1]. This model assumes that all unburned fuel inside the cylinder burns in one single reaction.

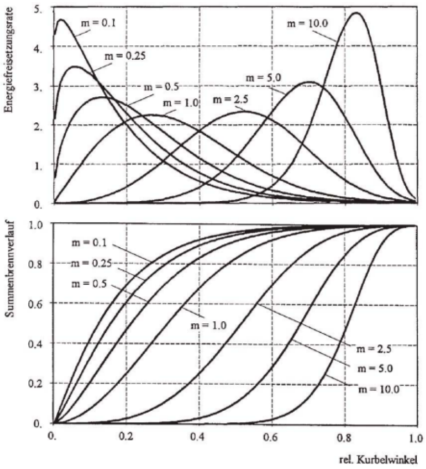

- **Vibe-Ersatzbrennverlauf**

$$\frac{Q_B(\varphi)}{Q_{B,ges}} = 1 - e^{-a\left(\frac{\varphi - \varphi_{BB}}{\Delta\varphi_{BD}}\right)^{m+1}} \quad \text{mit } \varphi_{BB} \leq \varphi \leq (\varphi_{BB} + \Delta\varphi_{BD})$$

$$\frac{\mathrm{d}Q_B}{\mathrm{d}\varphi} = Q_{B,ges}\, a\,(m+1)\left(\frac{\varphi - \varphi_{BB}}{\Delta\varphi_{BD}}\right)^{m} e^{-a\left(\frac{\varphi - \varphi_{BB}}{\Delta\varphi_{BD}}\right)^{m+1}}$$

Fig. 7 Vibe-Combustion heat release for different formfactors, copied from Merker [1]

The most complex conservation law is the energy equation.

$$\begin{aligned}
&\frac{d}{dt}\Big((M_{Air} + M_{Fb}) \cdot e_{gas} + M_{Fu} \cdot e_{fuel}\Big) \\
&\qquad = \big(\dot{m}_{Air,in} + \dot{m}_{Fb,in}\big) \cdot h_{gas,in} + \dot{m}_{Fu,in} \cdot h_{fuel,in} \\
&\qquad + \big(\dot{m}_{Air,ex} + \dot{m}_{Fb,ex}\big) \cdot h_{gas,ex} + \dot{m}_{Fu,ex} \cdot h_{fuel,ex} - p \cdot \dot{V} \\
&\qquad - \alpha \cdot A_{Wall} \cdot (T - T_{Wall}) - \dot{Q}_{Vibe}
\end{aligned} \tag{3.30}$$

Carrying out the differentiation yields derivatives of the masses which are known from the mass conservation equations. For the specific energy of air and burned fuel e_{gas} it is assumed that depends on Temperature and the fraction λ but not on pressure. Instead of λ the reciprocal value richness factor $l_i = \frac{1}{\lambda}$ is used, already defined above.

The Woschni model (1970 [38], implementation from Merker [29]), but without swirl effects, is used to calculate the heat transfer coefficient $\alpha \left[\frac{W}{m^2 K}\right]$ based on the dimensionless semiempirical correlations with the Nusselt, Reynolds and Prandtl numbers.

3.2.3 Orifices

The mass flow rate through valves and other flow devices is computed assuming subsonic or sonic flow through a flow restriction [1] [29] [36] [3]. Constant effective flow area can be set as a product of geometric reference area and a discharge flow coefficient $A_{Eff} = \mu \cdot A$. Alternatively, a relative valve opening (from 0 to 1) can be used from an external signal, for example in case of intake and exhaust valve opening area dependent on the crank angle $A_{Eff} = A_{Rel}(\varphi) \cdot A_{Ref}$. The orifice component uses the following boundary conditions:

- Inputs: M_{Air} , M_{Fb} , M_{Fu} , T … states from neighbouring components
- Outputs: $\dot{m}_i$, T_{up} … mass flow (air, burned-fuel, unburned-fuel), ups. temp.

Note that inputs for the orifice are outputs for the previously defined volume component and vice versa.

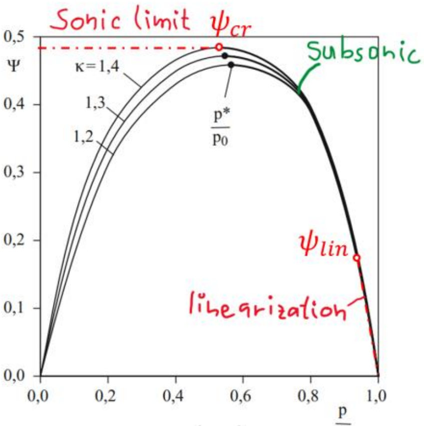

Abb. 2-11: Ausflussfunktion $\Psi\left(\frac{p_1}{p_0},\kappa\right)$

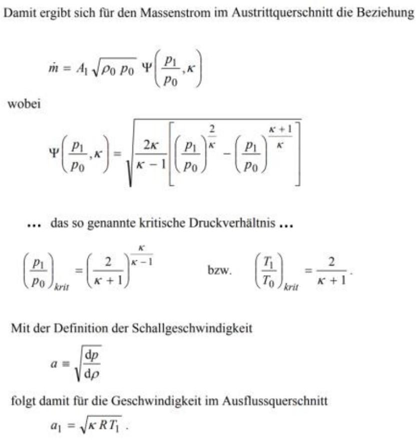

Damit ergibt sich für den Massenstrom im Austrittquerschnitt die Beziehung

$$\dot{m} = A_1 \sqrt{\rho_0 \, p_0} \; \Psi\left(\frac{p_1}{p_0},\kappa\right)$$

wobei

$$\Psi\left(\frac{p_1}{p_0},\kappa\right) = \sqrt{\frac{2\kappa}{\kappa-1}\left[\left(\frac{p_1}{p_0}\right)^{\frac{2}{\kappa}} - \left(\frac{p_1}{p_0}\right)^{\frac{\kappa+1}{\kappa}}\right]}$$

… das so genannte kritische Druckverhältnis …

$$\left(\frac{p_1}{p_0}\right)_{krit} = \left(\frac{2}{\kappa+1}\right)^{\frac{\kappa}{\kappa-1}} \qquad \text{bzw.} \qquad \left(\frac{T_1}{T_0}\right)_{krit} = \frac{2}{\kappa+1} .$$

Mit der Definition der Schallgeschwindigkeit

$$a \equiv \sqrt{\frac{\mathrm{d}p}{\mathrm{d}\rho}}$$

folgt damit für die Geschwindigkeit im Ausflussquerschnitt

$$a_1 = \sqrt{\kappa R T_1} .$$

Fig. 8 Saint-Venant flow function for different isentropic exponents κ, copied from Merker [1], with highlighted sonic, subsonic and linearized region

The mass flows rates are calculated by using the well-known Saint-Venant formula for compressible flow

$$\dot{m}_{SV} = A_{Eff} \cdot \sqrt{2 \cdot \rho_u \cdot p_u} \cdot \psi(x) \quad , \qquad \textit{with } x = \frac{p_d}{p_u}$$

$$\psi(x) \begin{cases} x \le x_{cr} \rightarrow & \psi_{cr} = \left(\frac{2}{\kappa+1}\right)^{\frac{1}{\kappa-1}} \cdot \sqrt{\frac{\kappa}{\kappa+1}} & \text{… sonic limit} \\ x > x_{cr} \rightarrow & \psi(x) = \sqrt{\frac{\kappa}{\kappa-1} \cdot \left(x^{\frac{2}{\kappa}} - x^{\frac{\kappa+1}{\kappa}}\right)} & \text{… subsonic flow} \\ x > x_{lin} \rightarrow & \psi(x) = \psi_{lin} \cdot \frac{1-x}{1-x_{lin}} & \text{… linearization} \end{cases} \qquad \textbf{(3.31)}$$

, where x refers to the ratio of the static pressure downstream of the restriction to the upstream stagnation pressure. The fluid properties in the formula are calculated as mixture of air, burned fuel and unburned fuel (polytropic ratio $\kappa = f(T, l_i)$, see Fig. 46 in Appendix - theory).

Flow is always considered subsonic or sonic but never supersonic. Therefore, the flow is limited pressure ratio lower than critical $\frac{p_d}{p_u} \leq x_{cr}$. Furthermore, the flow function is replaced by a linear function near unity (when $\frac{p_d}{p_u} \rightarrow 1$) in order to stabilize the system by avoiding of an infinite gradient of the flow function ($d\psi/dx \rightarrow \infty$).

The Saint-Venant formula yield a total mass flow (of a mixture) as function of the thermodynamic properties upstream and downstream. This mass flow is split into air, burned and unburned fuel according to composition of the working medium contained in the adjacent elements (upstream).

Optionally the mass flow can be smoothed with a first order filter, giving an additional equation (1 ODE) the solved system

$$\frac{d}{dt}(\dot{m}) = \frac{\dot{m}_{SV}(x) - \dot{m}}{T_{delay}} \qquad \textbf{(3.32)}$$

The filter may be useful to stabilize dynamics. The time delay constant T_{delay} can be also used as a calibration parameter to adjust transport delay behavior to the mass flow.

Starting from the Saint-Venant equation (3.31) for compressible flow and taking the limit $\kappa \rightarrow \infty$ for incompressible flow, one obtains

$$\dot{m}_{Ber} = A_{Eff} \cdot \sqrt{2 \cdot \rho_u \cdot p_u} \cdot \sqrt{\frac{1}{1} \cdot (x^0 - x^1)} = A_{Eff} \cdot \sqrt{2 \cdot \rho_u \cdot (p_u - p_d)} \qquad \textbf{(3.33)}$$

which is the incompressible Bernoulli's equation. For small pressure difference $\Delta p = p_u - p_d$ the error of using Bernoulli's equation as an approximation for the Saint-Venant equation is small: e.g., for $\Delta p < 100 hPa$ the error is below 6%. As both Saint-Venant and Bernoulli require basically the same inputs (except κ), a possible benefit of using the Bernoulli approximation could be the case where the pressure difference

Δp is known, while the upstream pressure p_u is known only approximately (see also section 4.2.2, Saint-Venant vs. Bernoulli Fig. 25).

3.3 Turbocharger

Turbochargers in engine simulations are often represented by characteristic maps, that are usually based on experimental data [39] [40] [6] [13] [47]. Understanding how the data was acquired has a crucial importance for correct postprocessing. The compressor and turbine map are recorded simultaneously by measuring lines of constant speed under steady-state conditions. A combustion chamber substitutes the exhaust side of the engine and provides gas at a constant temperature. The compressor stage is acting as a power brake of the turbine stage. An adjustable throttle, located at the compressor outlet enables to set a certain compressor flow rate $\dot{m}_c$ at constant turbocharger shaft speed n_{TC} [40]. Flow behavior of the compressor is then expressed as a relation of compressor pressure ratio dependent on mass flow at each individual speed. Definition of the compressor flow characteristics can be expressed as follows:

$$\Pi_c = f_{2D}\left(\dot{m}_{N,c},\ n_{N,c}\right) \tag{3.34}$$

It is a common practice that thermodynamic quantities defining the x, y and z coordinates are expressed in standardized units proposed in SAE 9222 [39]:

- $\dot{m}_{N,c} = \dot{m}_{N,c} \cdot \sqrt{\frac{T_1}{T_{1,ref}}} \cdot \frac{p_{1,ref}}{p_{1t}}$ … normalized compressor mass flow rate (x-coordinate)
- $n_{N,c} = n_{N,c} \cdot \sqrt{\frac{T_{1,ref}}{T_1}}$ … normalized compressor shaft speed (y-coordinate)
- $\Pi_c = \frac{p_{2t}}{p_{1t}}$ … compressor total downstream to total upstream pressure ratio (z-coordinate)

These reductions to normalized boundary pressure ($p_{1,ref} = 1bar$) and temperature ($T_{1,ref} = 300K$) conditions enable better comparison between different turbochargers being characterized. The compressor isentropic enthalpy difference is defined by upstream and downstream conditions:

$$\Delta h_{sC} = c_{p,air} \cdot T_1 \cdot \left[\left(\frac{p_{2t}}{p_{1t}} \right)^{\frac{\kappa_{air}-1}{\kappa_{air}}} - 1 \right] \tag{3.35}$$

Finally, the compressor isentropic efficiency is defined as a ratio between enthalpy difference for isentropic compression Δh_{sC} and the enthalpy difference for a real compression Δh_C [47].

$$\eta_{sC} = \frac{\Delta h_{sC}}{\Delta h_C} = \frac{T_1 \cdot \left[\left(\frac{p_{2t}}{p_{1t}} \right)^{\frac{\kappa_{air}-1}{\kappa_{air}}} - 1 \right]}{T_2 - T_1} \tag{3.36}$$

Fig. 9 shows the compressor characteristic map as defined in (3.34) with the efficiency defined in (3.36). The map was obtained from the hot gas stand measurement data provided by the turbocharger manufacturer.

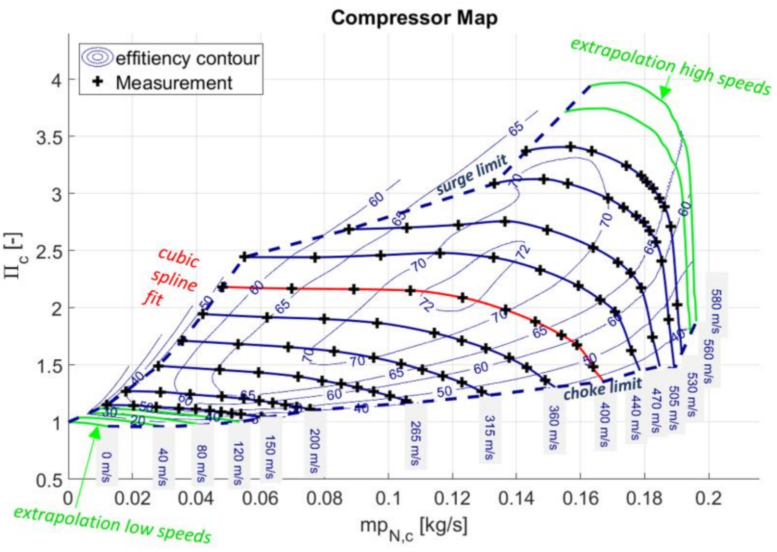

Fig. 9 Compressor map (flow rate & efficiency) obtained from steady-state hot gas stand measurements (data provided by turbocharger manufacturer)

A data oriented cubic spline fit is used to approximate the compressor maps. The MATLAB build-in interpolation is called by the function "interp1". Function argument option "pchip" is set to become shape-preserving piecewise cubic interpolation [41].

As an alternative to data oriented fit, more sophisticated physical based regressions can be used [13] [6] [47], but they are not subject of this work.

For the turbine characterization, reduced flow rate is mapped in dependence on the ratio of total pressure at turbine inlet to the static pressure at turbine outlet for each individual turbocharger speed. Definition of the turbine flow characteristics can be expressed as follows:

$$\dot{m}_{R,t} = f_{2D}(\Pi_t,\ n_{R,t}) \tag{3.37}$$

Again, the x, y and z coordinates are given in standardized units proposed in SAE 9222 [39]:

- $\Pi_t = \frac{p_{3t}}{p_4}$ … turbine total upstream to static downstream pressure ratio (x-coordinate)
- $n_{R,t} = \frac{n_{TC}}{\sqrt{T_3}}$ … reduced turbine shaft speed (y-coordinate)
- $\dot{m}_{R,t} = \dot{m}_t \cdot \frac{\sqrt{T_3}}{p_{3t}}$ … reduced turbine mass flow rate (z-coordinate)

For the turbine stage, an efficiency calculation analogous to the compressor according to equation (3.36) cannot be carried out. The outlet temperature T_4 cannot be used because – despite insulation – the occurring heat losses to external can be in the same order of magnitude like aerodynamic power converted by the rotor. This can lead to apparent efficiencies larger than unity. In addition, the temperature measurement T_4 is potentially subject to the influence of hot or cold streaks as well as swirl variations in the turbine outlet flow [40] [42]. An alternative efficiency definition, based on the ratio of the compressor power and turbine power, is utilized. At steady-state conditions, power delivered by the turbine and power consumed by the compressor is equal:

$$P_c = P_t \tag{3.38}$$

Compressor power and turbine power can be expressed in dependence on idealized isentropic state change, corresponding isentropic efficiency and mechanical efficiency:

$$\dot{m}_c \cdot \Delta h_{sC} \cdot \frac{1}{\eta_{sC} \cdot \eta_{mC}} = \dot{m}_t \cdot \Delta h_{sT} \cdot \eta_{sT} \cdot \eta_{mT} \tag{3.39}$$

Besides isentropic efficiencies, the equation (3.39) also considers mechanical efficiencies. For practical reasons, both mechanical losses of the compressor stage and the turbine stage are accounted only to the turbine. The overall turbocharger efficiency can be expressed as:

$$\eta_{TC} = \eta_{sC} \cdot (\eta_{mC} \cdot \eta_{mT} \cdot \eta_{sT}) = \eta_{sC} \cdot (\eta_m \cdot \eta_{sT}) \tag{3.40}$$

Analogically to the equation (3.35) for compressor, the turbine isentropic enthalpy difference is defined by upstream and downstream conditions:

$$\Delta h_{sT} = c_{p,gas} \cdot T_3 \cdot \left[\left(\frac{p_4}{p_{3t}} \right)^{\frac{\kappa_{gas}-1}{\kappa_{gas}}} - 1 \right] \tag{3.41}$$

This yields the commonly used definition of turbine efficiency as a product of turbine isentropic efficiency and mechanical friction losses [40] [39]:

$$\eta_T = (\eta_m \cdot \eta_{sT}) = \frac{1}{\eta_{sC}} \cdot \frac{\dot{m}_c \cdot c_{p,air} \cdot T_1 \cdot \left[\left(\frac{p_{2t}}{p_{1t}} \right)^{\frac{\kappa_{air}-1}{\kappa_{air}}} - 1 \right]}{\dot{m}_t \cdot c_{p,gas} \cdot T_3 \cdot \left[1 - \left(\frac{p_4}{p_{3t}} \right)^{\frac{\kappa_{gas}-1}{\kappa_{gas}}} \right]} \tag{3.42}$$

By substitution of already known compressor isentropic efficiency from equation (3.36) into equation (3.42), the turbine efficiency is estimated in dependence on the measured turbocharger flow conditions.

For the purpose of the data approximation, dimensionless coordinates are used:

- $\Pi_{t,sta} = \frac{p_3}{p_4}$ … turbine static upstream to static downstream pressure obtained by the centrifugal transformation to make it speed independent
- $BSR = \frac{u_4}{c_S}$ … blade speed velocity ratio with the turbine outlet circumferential velocity u_4 and the fictitious isentropic velocity $c_S = \sqrt{2 \cdot \Delta h_{sT}}$

The turbine mass flow is then assumed to be an ideal compressible nozzle flow according to the Saint-Venant function (3.31) [39]

$$\dot{m}_{R,t} = \underbrace{\mu_T(\Pi_{t,sta})}_{\text{polyfit-4}^{th}\text{ order}} \cdot \underbrace{\frac{1}{\psi_{cr}} \cdot \sqrt{\left(\frac{1}{\Pi_{t,sta}}\right)^{\frac{2}{\kappa_{gas}}} - \left(\frac{1}{\Pi_{t,sta}}\right)^{\frac{\kappa_{gas}+1}{\kappa_{gas}}}}}_{\psi_{norm,one}(x)} \tag{3.43}$$

, where the flow function $\psi_{norm,one}$ was normalized to unity and the deviations from ideal nozzle flow are corrected by the discharge coefficient μ_T based on a 4th order polynomial data fit (see Fig. 10 left).

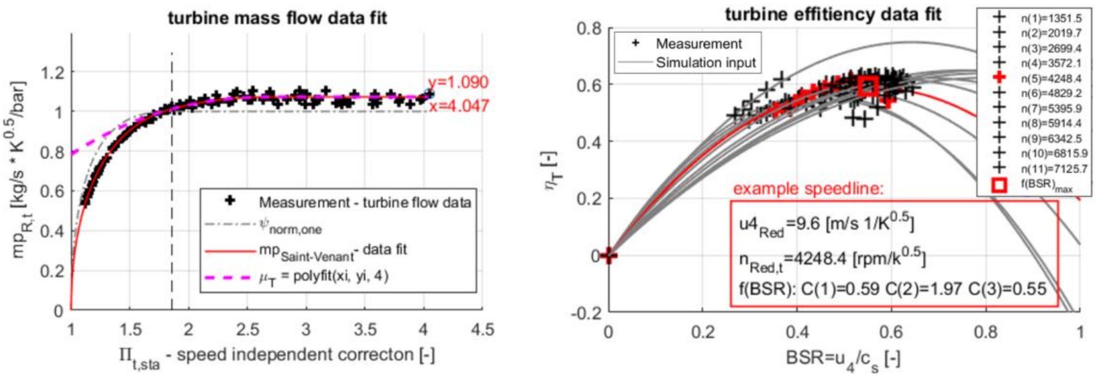

Fig. 10 Left: compressor pressure map used as simulation input, based on turbocharger measurement data fit
Right: compressor enthalpy difference used as simulation input, based on turbocharger measurement data fit

The turbine efficiency defined in (3.42) is approximated as a parabolic function of the blade speed ratio (see Fig. 10 right).

$$\begin{aligned} \eta_T(x{:}BSR) \; &= C_1 - C_2 \cdot \, (\, x - C_3 \,)^2 \\ C_1 &= \eta_{max} \text{ … maximum efficiency} \\ C_2 &= k \text{ … parabola multiply factor} \\ C_3 &= BSR_{max} \text{ … blade speed ratio at which function is maximum} \end{aligned} \tag{3.44}$$

It should be mentioned that the approximation (3.44) is valid only for radial turbines at the vicinity of optimum efficiency. Otherwise, higher order polynomial should be used to consider asymmetry of the efficiency curve.

3.3.1 Compressor

The compressor is modelled as a flow device within the simulation and has therefore the same thermodynamic boundary conditions like the orifice (gets pressures, gives mass flow, see also section 3.2.3). Additionally, mechanical boundary conditions based on the torque (power) equilibrium are used. The boundary conditions are:

- Inputs: p_{1t} , p_{2t} , T_1 , ρ_1, n_{TC}
- Outputs: $\dot{m}_c$, T_2 , T_{qC}

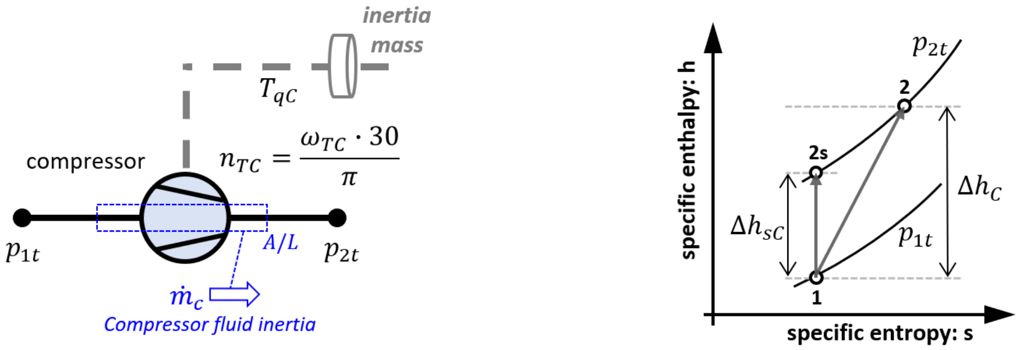

Fig. 11 Principle of compressor simulation (with 1 ODE)

Due to the non-monotonic compressor flow map (see Fig. 9), a direct interpolation of the mass flow as a function of the pressure ratio $\dot{m}_c = f(\Pi_c)$ is ambiguous. This well-known problem was treated in different publications [13] [6] [9], proposing multiple solution possibilities. Solution proposed by Friedrich [9], also published in Mecca 2022 [47], is being used. The idea is that a fluid mass in the control volume between upstream and downstream boundaries (see Fig. 11) must be accelerated by a pressure difference acting on cross section area on both sides of the control volume.

$$(\rho_1 \cdot A \cdot L) \cdot \frac{d}{dt}(u_c) = A \cdot p_1 - A \cdot p_2 - A \cdot (p_{2t} - p_{1t}) \qquad \textbf{(3.45)}$$

The momentum conservation (3.45) leads to an additional differential equation (1 ODE) to be solved in the system

$$\frac{d}{dt}(\dot{m}_c) = \frac{A}{L} \cdot \left[\underbrace{\Pi_c\left(\dot{m}_{N,c},\ n_{N,c}\right)}_{\textit{map-interpolation}} \cdot p_{1t} - p_2\right] \tag{3.46}$$

The compressor mass flow results from the time integration of (3.46). The pressure ratio in (3.46) was obtained by interpolation of the compressor characteristics (see Fig. 12 Left), which is already straight-forward and gives an unambiguous solution.

It was found out that an inter- / extrapolation of the compressor enthalpy difference (Fig. 12 Right) provides more stable results than a direct use of the compressor efficiency map (used for example by [40]). Stability issues affect in particular turbocharger transitions from low speeds [47]. More details on this issue can be seen in Appendix – Theory in Fig. 50.

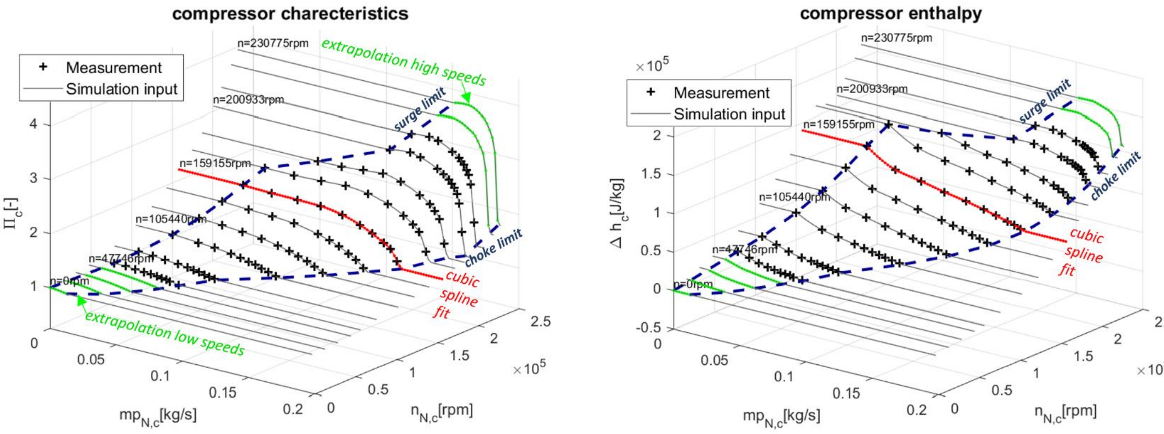

Fig. 12 Left: compressor pressure map used as simulation input, based on turbocharger measurement data fit
Right: compressor enthalpy difference used as simulation input, based on turbocharger measurement data fit

The resulting compressor output torque is calculated as

$$T_{qC} = \dot{m}_c \cdot \underbrace{\Delta h_C\left(\dot{m}_c,\ n_{N,c}\right)}_{\textit{map-interpolation}} \cdot \frac{1}{\omega_{TC}} \tag{3.47}$$

and resulting compressor downstream temperature is calculated as

$$T_2 = T_1 + \frac{\Delta h_C}{c_{p,int}} \tag{3.48}$$

, both dependent on the given boundary conditions.

3.3.2 Turbine

The turbine is modelled as a flow restriction between two gas states and has therefore same thermodynamic boundary conditions like the orifice (gets pressure, gives mass flow, see also section 3.2.3). A mechanical boundary condition at the turbine shaft (input speed, output torque) is defined analogously to the compressor. The boundary conditions are: are:

- Inputs: p_{3t} , p_4 , T_3 , ρ_3, n_{TC}
- Outputs: $\dot{m}_t$, T_4 , T_{qT}

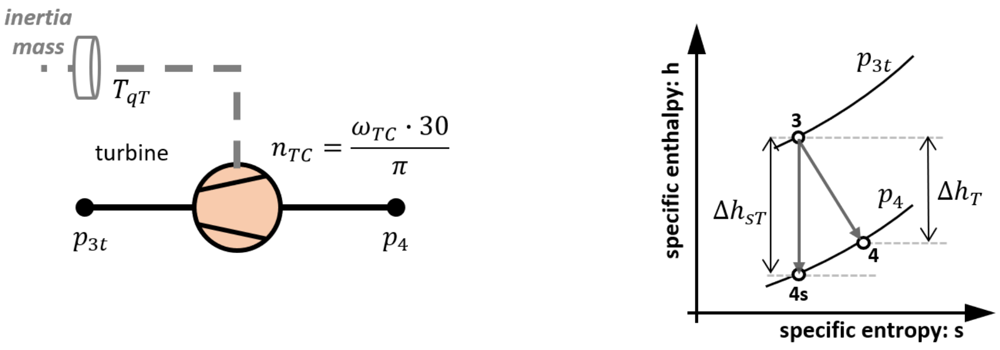

Fig. 13 Principle of turbine simulation (maps interpolations)

The reduced turbine mass flow is obtained by a straight-forward interpolation of the turbine characteristics (see Fig. 14 Left) defined in equation (3.37) with the given boundary pressure ratio Π_t and the reduced turbine speed $n_{R,t}$.

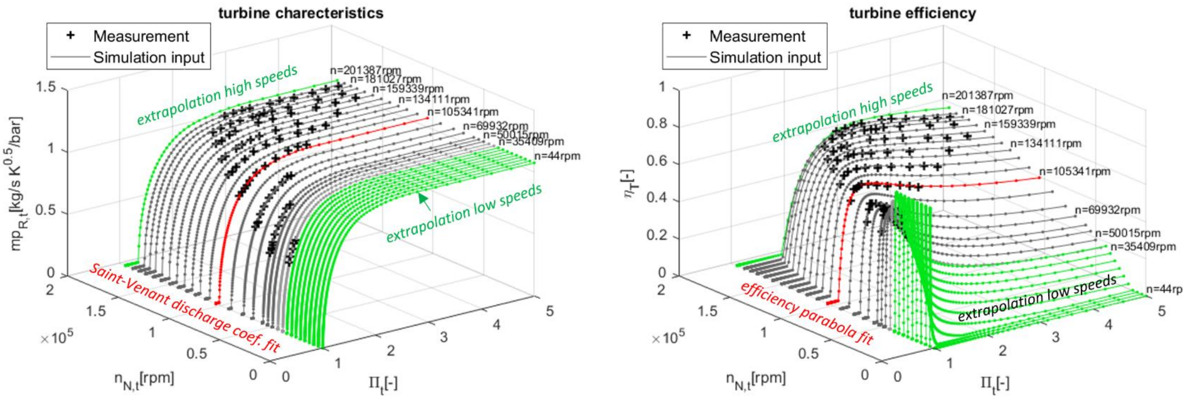

Fig. 14 Left: turbine mass flow characteristics used as simulation input, based on turbocharger measurement data fit
Right: turbine efficiency (product of turbine isentropic efficiency and turbocharger mechanical efficiency) used as simulation input, based on turbocharger measurement data fit

The real turbine mass flow, being an output variable, follows from the interpolated reduced mass flow by the given SAE9222 definitions.

$$\dot{m}_t = \underbrace{\dot{m}_{R,t}\left(\Pi_t,\ n_{N,t}\right)}_{\textit{map-interpolation}} \cdot \frac{p_{3t} \cdot 10^{-5}}{\sqrt{T_3}} \tag{3.49}$$

The real specific enthalpy difference is calculated from the ideal isentropic enthalpy difference (3.41) and the interpolated turbine efficiency (see definition (3.42) and also Fig. 14 Right):

$$\Delta h_T = \underbrace{c_{p,exh} \cdot T_3 \cdot \left[1 - \left(\frac{p_4}{p_{3t}}\right)^{\left(\frac{\kappa_{exh}-1}{\kappa_{exh}}\right)}\right]}_{\Delta h_{sT}} \cdot \underbrace{\eta_T\left(\Pi_t,\ n_{N,t}\right)}_{\textit{map-interpolation}} \tag{3.50}$$

The resulting turbine output torque follows by division of turbine power with the angular velocity of the turbine shaft

$$T_{qT} = \dot{m}_t \cdot \Delta h_T \cdot \frac{1}{\omega_{TC}} \tag{3.51}$$

and the resulting downstream temperature is calculated as

$$T_4 = T_3 - \frac{\Delta h_T}{c_{p,exh}} \tag{3.52}$$

The equations (3.51) and (3.52) depend directly on the given boundary conditions.

3.3.3 Torque Equilibrium on TC Shaft (Including Inertial Mass)

The turbocharger model is supposed to operate under transient engine operating conditions. Equilibrium of power provided by the turbine and consumed by the compressor as assumed for steady-state measurement evaluation in equation (3.38) is no more given. To consider basic dynamic effects such as turbo lag, the map-based model is extended with mechanical inertia mass [40] [6] [47]. The dynamic power equilibrium gets the following form:

$$P_T - P_C - P_I = 0 \tag{3.53}$$

This is equivalent to the mechanical torque equilibrium on the turbocharger shaft, when the equation (3.53) is divided by the angular velocity $\omega_{TC} = n_{TC} \cdot (\pi/30)$

$$T_{qT} - T_{qC} - T_{qI} = 0 \quad \text{, with} \quad T_{qI} = I \cdot \ddot{\varphi}_{TC} \tag{3.54}$$

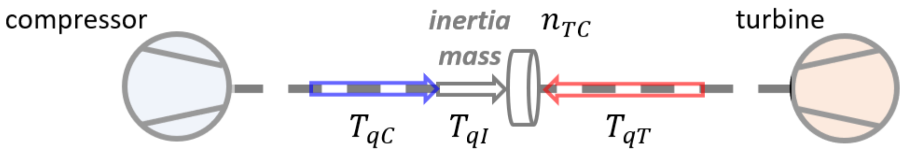

Fig. 15 Definition of torques used for simulation of turbocharger shaft as a rotatory inertia mass

This leads to two differential equations (2 ODEs) for the accelerated mass with a given inertia (for example $I = 2 \cdot 10^{-5} kg \cdot m^2$):

$$\frac{d}{dt}\begin{pmatrix}\varphi_{TC}\\ \omega_{TC}\end{pmatrix} = \begin{pmatrix}\omega_{TC}\\ \left[T_{qT} - T_{qC} - \omega_{TC} \cdot d\right]/I\end{pmatrix} \tag{3.55}$$

Optionally, a damping parameter (for example $d = 2.5 \cdot 10^{-5}\, N/(rad/s)$) can be used to calibrate turbocharger viscose friction, but the turbocharger mechanical losses were already considered in the definition of the turbine efficiency (see definition (3.40) and (3.42)). Therefore, the damping parameter should be theoretically set to zero.

3.4 Pipe Systems

In section 3.4.1, a finite volume method is implemented to achieve best possible resolution of transient flow including the gas composition of tree species (air, burned fuel, unburned fuel). This complex approach for transient 1D flow in pipes, labelled as ‘gas dynamics-full’ is simplified to ‘gas dynamics-reduced’ based on analysis of every term occurring in given transport equation. If the numerical value of some term is small in comparison to other terms, especially by derivative terms, it is being neglected or set as constant. Presented simplifications allow calculation with almost same accuracy, especially when the change of state variables is small, while reducing of computing time.

Later in section 3.4.2, simplifications according to classical acoustic theory applied within a finite volume method, based on the solution of Riemann problem are presented. The objective is to find the simplest possible approach to allow the calculation of pressure wave propagation through space, especially with unstable momentum conservation. The accuracy issues are not considered primarily.

3.4.1 Complex Transient 1D Flow in Pipes

The 1D flow in the detailed model is described by the complete set of three transport conservation laws for mass, momentum and energy. Governing equations can be taken from Pischinger [29] (or Wesseling [30], or LeVeque [31]).

Matrix form:

$q_t + f(q)_x = s$

$$\begin{pmatrix} \rho \\ \rho u \\ \rho E \end{pmatrix}_t + \begin{pmatrix} \rho u \\ p + \rho u^2 \\ \rho u H \end{pmatrix}_x = \begin{pmatrix} 0 \\ (-\Delta p_{fric} - p_{damp})/\Delta x \\ Q_H/(\Delta x A) \end{pmatrix} \tag{3.56}$$

$E = e + \frac{u^2}{2} = c_v \cdot T + \frac{u^2}{2} \left[\frac{J}{kg}\right]$ ... Total specific internal energy

$H = h + \frac{u^2}{2} = c_p \cdot T + \frac{u^2}{2} \left[\frac{J}{kg}\right]$ ... Total specific gas enthalpy

p_{damp} $[Pa]$ ... Pressure term for numerical stabilization

Δp_{fric} $[Pa]$ ... Pressure drop due to wall friction

Q_H $[W]$ ... Wall heat transfer

Partial Differential Equations (PDEs) are discretized in space by using 1st order upwind scheme on a 1D finite volume mesh leading in a set of Ordinary Differential Equations (ODEs).

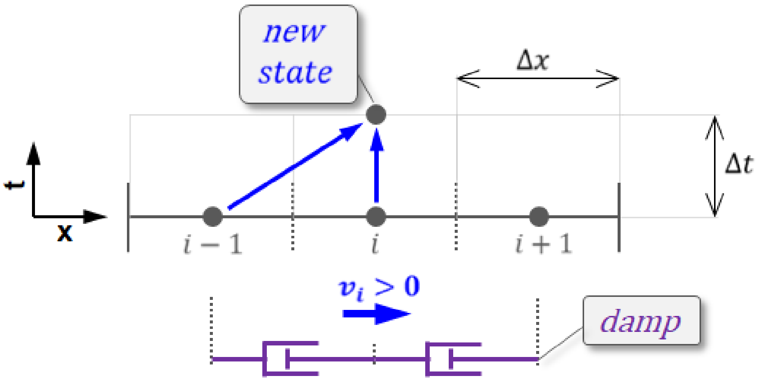

Fig. 16 Information flow in time-space domain when using 1st order upwind discretization with additional numerical damping stabilization

This differential scheme is computationally very fast, however, it requires additional numerical stabilization. The use of explicit time integration methods (2nd order Runge-Kutta), especially in combination with long integration time steps, leads to numerical oscillations. Numerical stabilization was formulated as a function of element gas velocities by using a simple spring-damper model.

Mass conservation is formulated for all three gas components: air, burned fuel and unburned fuel. Empirical source terms for wall friction and heat transfer are considered. Caloric properties of the gas mixture are assumed to be a function of temperature and air-fuel ratio. The single pipe component is assumed to have constant cross-sectional area.

Matrix form:

$$\dot{q}_{FVM,i} = \frac{1}{\Delta x} \cdot [f_{in} - f_{out}] + s$$

$$\begin{bmatrix} \dot{M}_{Air} \\ \dot{M}_{Fb} \\ \dot{M}_{Fu} \\ \dot{u} \\ \dot{T} \end{bmatrix}_{FVM,i} = \begin{bmatrix} \rho_{Air,in} \cdot u_{in} \cdot A - \rho_{Air,out} \cdot u_{out} \cdot A \\ \rho_{Fb,in} \cdot u_{in} \cdot A - \rho_{Fb,out} \cdot u_{out} \cdot A \\ \rho_{Fu,in} \cdot u_{in} \cdot A - \rho_{Fu,out} \cdot u_{out} \cdot A \\ \cdots \\ \cdots \end{bmatrix}_i \qquad \textbf{(3.57)}$$

$$\dot{u}_{FVM,i} = \frac{1}{M} \cdot \left(\left(p_{in} - p_{out} - \Delta p_{fric} + p_{damp} \right) \cdot A + \rho_{in} \cdot u_{in}^2 \cdot A \; - \rho_{out} \cdot u_{out}^2 \cdot A - \dot{M} \cdot u_i \right)$$

... Velocity change ~ acceleration

$$\dot{T}_{FVM,i} = \frac{1}{M \cdot (\partial e / \partial T)} \cdot \left(\dot{m}_{in} \cdot \left(h_{in} + \frac{u_{in}^2}{2} \right) - \dot{m}_{out} \cdot \left(h_{out} + \frac{u_{out}^2}{2} \right) + Q_H - M \cdot \frac{\partial e}{\partial li} \cdot (\dot{li}) - \dot{M} \cdot \left(e + \frac{u^2}{2} \right) - M \cdot u \cdot \dot{u}_i \right)$$

... Temperature change

$M_{Air} = \rho_{Air} \cdot (\Delta x A)\ [kg]$ ... Air mass in volume element

$M_{Fb} = \rho_{Fb} \cdot (\Delta x A)\ [kg]$ ... Burned fuel mass in volume element

$M_{Fu} = \rho_{Fu} \cdot (\Delta x A)\ [kg]$ ... Unburned fuel mass in volume element

$M = M_{Air} + M_{Fb} + M_{Fu} [kg]$ ... Total mass of volume element

Since the calculation of all terms is very time consuming, the model is divided in two versions. A first version 'gas dynamics-full' considers all terms correctly including kinetic energy terms in momentum equation, total enthalpy change in energy equation and gas properties are being modelled as a function of temperature and air-fuel ratio. On the other hand, a second version of model named 'gas dynamics-reduced' neglects kinetic terms, simplifies enthalpy flux terms and gas properties are being estimated only once at initial time.

Gas dynamics-full versus gas dynamics-reduced: **(3.58)**

gas dynamics-full:

$\rho_{in} \cdot u_{in}^2 \cdot A \left[\frac{kgm}{s^2}\right]$ ... Kinetic energy term

gas dynamics-reduced:

$\cancel{\rho_{in} \cdot u_{in}^2 \cdot A} \left[\frac{kgm}{s^2}\right]$ ... Kinetic energy term neglected gas dynamics-full:

$\dot{M} = \frac{dM}{dt} = \dot{M}_{Air} + \dot{M}_{Fb} + \dot{M}_{Fu} \left[\frac{kg}{s}\right]$ ... Total mass change

gas dynamics-reduced:

$\dot{M} = \frac{dM}{dt} = 0 \left[\frac{kg}{s}\right]$ ... Total mass change neglected

gas dynamics-full:

Internal energy changes are being modelled by polynomial approximations of tabulated gas properties:

$$M \cdot (\partial e/\partial T) = (M_{Air} + M_{Fb}) \cdot \frac{\partial e_{Burned}}{\partial T} + M_{Fu} \cdot \frac{\partial e_{Unburned}}{\partial T} \left[\frac{J}{K}\right]$$

, where internal energy is a function of temperature and air-fuel ratio:

$$\frac{\partial e_{Burned}}{\partial T} = c_{v,Burned}(T, li) \left[\frac{J}{kgK}\right]$$

... Change of specific internal energy of burned gases

$$\frac{\partial e_{Unburned}}{\partial T} = c_{v,Unburned}(T, li) \left[\frac{J}{kgK}\right]$$

... Change of specific internal energy of unburned gases

gas dynamics-reduced:

$$M \cdot (\partial e/\partial T) = M \cdot CV \left[\frac{J}{K}\right]$$

... Specific internal energy is estimated only once at initial time

gas dynamics-full:

Total enthalpy flux term

$$\dot{m}_{in} \cdot \left(h_{in} + \frac{u_{in}^2}{2}\right) = \left(\dot{m}_{Air,in} + \dot{m}_{Fb,in}\right) \cdot \left(h_{burned,in} + \frac{u_{in}^2}{2}\right) + \dot{m}_{Fu,in} \cdot \left(h_{Fu,in} + \frac{u_{in}^2}{2}\right) \left[\frac{J}{s}\right]$$

, where enthalpy is a function of temperature and air-fuel ratio:

$$h_{burned,in} = c_{p,burned}(T_{in}, li_{in}) \left[\frac{J}{kgK}\right]$$

... Change of specific enthalpy of burned gases

$$h_{Fu,in} = c_{p,Fu}(T_{in}, li_{in}) \left[\frac{J}{kgK}\right]$$

... Change of specific enthalpy of unburned fuel

gas dynamics-reduced:

Total enthalpy flux term

$$\dot{m}_{in} \cdot \left(h_{in} + \frac{u_{in}^2}{2}\right) = \dot{m}_{in} \cdot CP \cdot (T_{in} - T_0) \left[\frac{J}{s}\right]$$

... Specific enthalpy is estimated only once at initial time gas dynamics-full:

$$\alpha_H = 0.5 \cdot \lambda_{fric} \cdot u \cdot \rho \cdot c_p \left[\frac{W}{m^2K}\right]$$

... Heat transfer coefficient dependent on flow velocity

gas dynamics-reduced:

$$\alpha_H = const. \left[\frac{W}{m^2K}\right]$$

... Heat transfer coefficient constant

The complex pipe model provides quite detailed information on thermal transport effects, but its complexity does not enable real-time capability on production ECU.

3.4.2 Simplification to 1D Linear Acoustics

The complex 1D flow in pipes strongly simplified. Proposed method was already published in Mecca 2018 [48]. The assumptions are:

- **Governing equations:**
  All three conservation laws (nonlinear) → Linearized acoustic equations
- **Discretization scheme:**
  Upwind → Riemann solver
- **Caloric gas properties:**
  Variable → Constant

Classical acoustic theory provides a reasonable compromise to consider basic pressure wave propagation while reducing the computational time ([7], [8], [29]-page 33). Constant gas properties reduce the computational time further. Change of the discretization scheme improves numerical stability.

Simplifications according to classical acoustic theory ([29]-page 31, [31]-page 26) are taken into account:

- $A = const\ [m^2],\ \ dA = 0$ ... No change in cross-section area along pipe
- $u \ll a \left[\frac{m}{s}\right]$ ... Flow velocity is small in comparison with local speed of sound. Terms with u can therefore be neglected (but not its first derivative)
- $\rho \approx \bar{\rho} = const \left[\frac{kg}{m^3}\right]$ ... Small density oscillation around its given mean value

- $\dot{q} = 0 \left[\frac{W}{kg}\right]$ ... Adiabatic state changes (zero heat transfer)
- $T = \bar{T}\,[K] \rightarrow \bar{a} = \sqrt{\kappa R \bar{T}}$ ... Mean temperature is constant and given. This results in constant local speed of sound

Thermodynamic gas properties are calculated only once at the initial time step for a given reference temperature. The simplified transport equations can be written in matrix form using the state q, linearized flux $f = A \cdot q$ and a source term.

Matrix form:

$q_t + f(q)_x = s \rightarrow q_t + A \cdot q_x = s$

$$\begin{pmatrix} p \\ u \end{pmatrix}_t + \begin{pmatrix} 0 & \bar{\rho}\bar{a}^2 \\ 1/\bar{\rho} & 0 \end{pmatrix} \cdot \begin{pmatrix} p \\ u \end{pmatrix}_x = \begin{pmatrix} 0 \\ s_{fric} \end{pmatrix} \tag{3.59}$$

$s_{fric} = \frac{-\Delta p_{fric}}{\Delta x \cdot \bar{\rho}} \left[\frac{m}{s^2}\right]$ ... Friction source term

The only state variables are pressure p and velocity u. The source term considers empirical wall friction. Solution is obtained by using a so-called Riemann solver, which calculates the middle flux on the cell boundary "i+1/2" depending on left "L=i" and right "R=i+1" neighbouring states. Due to the linearity of matrix A, it is possible to estimate only the middle state on the cell boundaries. Then the middle flux is easily given by $f_{i+1/2} = A \cdot q_{i+1/2}$

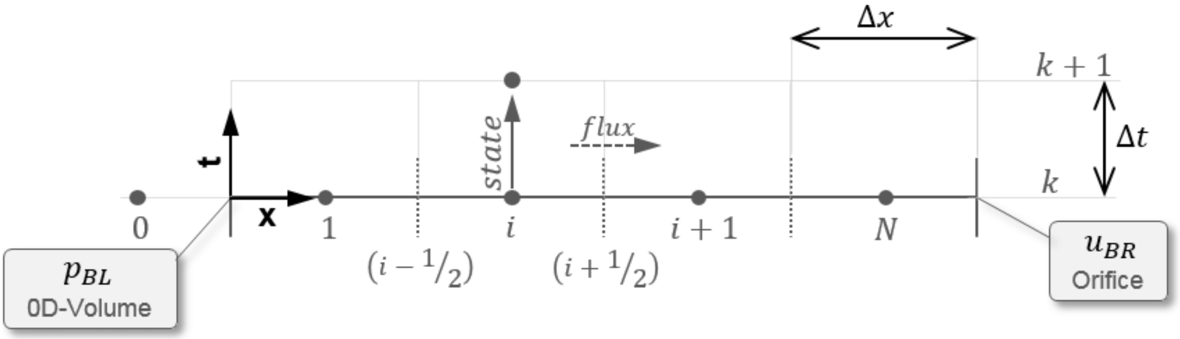

Fig. 17 Time-space domain, upper index "k" is used for time and the lower index "i" for space iteration

Equation for middle state can be taken from LeVeque ([31]-page 57)

$$\begin{bmatrix} p_{i+1/2} \\ u_{i+1/2} \end{bmatrix} = 0.5 \cdot \begin{bmatrix} (p_i + p_{i+1}) + \bar{\rho}\bar{a} \cdot (u_i - u_{i+1}) \\ (u_i + u_{i+1}) + {}^1\!/_{\bar{\rho}\bar{a}} \cdot (p_i - p_{i+1}) \end{bmatrix} \tag{3.60}$$

Static pressure is assumed to be known (for example from a neighbouring 0D volume component) at the left boundary condition $p_{0+1/2} = p_{BL}$ and velocity (for example from a neighbouring orifice component) at the right boundary condition $u_{N+1/2} = u_{BR}$.

Equations for left and right boundary elements are

Boundary left:

$$\begin{bmatrix} p_{0+1/2} \\ u_{0+1/2} \end{bmatrix} = \begin{bmatrix} p_{BL} \\ u_1 + {}^{1}\!/_{\bar{\rho}\bar{a}} \cdot (p_{BL} - p_1) \end{bmatrix} \quad \textbf{(3.61)}$$

Boundary right:

$$\begin{bmatrix} p_{N+1/2} \\ u_{N+1/2} \end{bmatrix} = \begin{bmatrix} p_N + \bar{\rho}\bar{a} \cdot (u_N - u_{BR}) \\ u_{BR} \end{bmatrix} \quad \textbf{(3.62)}$$

Next "Finite Volume Method" discretization of state and flux vectors

$$\frac{q_i^{k+1} - q_i^k}{\Delta t} + \frac{f_{i+1/2}^k - f_{i-1/2}^k}{\Delta x} = s \quad \textbf{(3.63)}$$

is used to resolve variables in time and space. The space resolution is calculated by the pipe component itself. On the other hand, the time integration is implemented into the global ordinary differential equations solver (2nd order Runge-Kutta) using following equation for the change of gas state:

Matrix form:

$$\dot{q}_{FVM,i} = \frac{1}{\Delta x} \cdot [f_{in} - f_{out}] + s \;\; \rightarrow \;\; \dot{q}_i = \frac{1}{\Delta x} \cdot \left(f_{i+1/2}^k - f_{i-1/2}^k\right) + s$$

$$\begin{bmatrix} \dot{p}_i \\ \dot{u}_i \end{bmatrix}_{FVM} = \frac{1}{\Delta x} \cdot \begin{bmatrix} \bar{\rho}\bar{a}^2 \cdot \left(u_{i-1/2} - u_{i+1/2}\right) \\ {}^{1}\!/_{\bar{a}} \cdot \left(p_{i-1/2} - p_{i+1/2} - \Delta p_{fric}\right) \end{bmatrix} \quad \textbf{(3.64)}$$

Δp_{fric} $[Pa]$ ... pressure drop due wall friction

This formulation results in an identical time step for all thermodynamic volume elements formulated by the filling-emptying approach and acoustical pipe elements. It is also possible to formulate locally different integration time step.

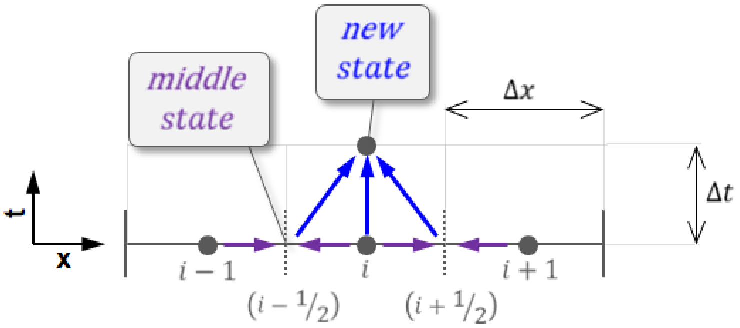

Fig. 18 Information flow in time-space domain when using Riemann solver

Fig. 3 illustrates information flow when calculating the middle state according to equation (4.6). This calculation is based on an analytical solution of Riemann problem at the cells boundaries and is therefore stable even for discontinuous solutions. Therefore, the Riemann solver doesn't require additional numerical damping, which is key benefit in comparison with the previously used upwind method. After evaluation of middle state and linear dependent middle flux, the finite volume step can be completed according to equation (4.9) and the new flow state q_i^{k+1} is calculated.

The wall friction Δp_{fric} is calculated as a function of Reynolds number according to the Moody's diagram, a similar approach is used in GT-Power software.

3.4.3 Numerical Testing of Pipe Components

The objective of numerical testing is to check basic functionality of newly developed pipe components with constant, precisely defined boundary conditions. In this context it is important to mention, that constant boundary condition doesn't mean constant gas state in boundary elements. To make the pipe component connectable to 0D volume component from left side and to orifice component from right side, it is necessary to fulfil related flow equations even in boundary elements.

This procedure can be explained on the 'linear acoustic' pipe component. In equation (3.61) can be seen that boundary pressure $p_{0+1/2} = p_{BL}$ is given by the connected component, whereas velocity at the left boundary must be calculated from given boundary pressure $u_{0+1/2} = f(p_{BL})$. A similar calculation must be done on the right boundary by using equation (3.62). Velocity on right boundary $u_{N+1/2} = u_{BR}$ is given by the connected component, whereas the pressure at right boundary must be calculated from given velocity $p_{N+1/2} = f(u_{BL})$. After solving element boundaries, new gas states in cell centers are calculated in all elements according to equation (3.64) for finite volume method. Calculation of boundaries for the ‘complex gas dynamic’ pipe component is not described in this thesis, but works on similar principle. Finite volume integration step for ‘complex gas dynamic’ pipe is given by equation (3.57).

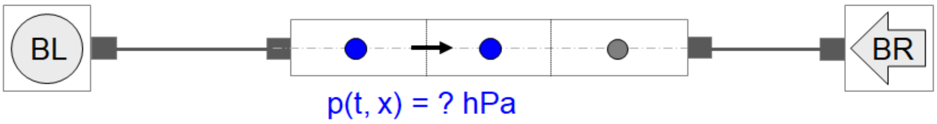

Fig. 19 Schematic representation of 1D pipe component with constant left boundary (BL) and right boundary (BR)

Therefore, a test of the pipe component consists of given boundary conditions and as a result the gas states in cell centres, especially pressure as a function of time and space, will be validated.

3.4.4 Discontinuous Initial Value Problem with Exact Solution

The initial value problem is defined by the set of conservation laws in form of $\dot{q} = f(q)$ (formulated in (3.57) for ‘complex gas dynamics’ and in (3.64) for ‘linear acoustics’) and appropriate constant initial conditions.

Initial conditions: **(3.65)**

$$p(\,t = 0s\,, x\,) = p_0 = 1200hPa$$

$$u(\,t = 0s\,, x\,) = u_0 = 0\frac{m}{s}$$

$$T(\,t = 0s\,, x\,) = T_0 = 300\ K$$

Following constant boundary conditions define a simple ‘Pipe Shock Test’:

Boundary conditions: **(3.66)**

$$p(\,t\,, x = 0m\,) = p_{BL} = 3000hPa$$

$$p(\,t\,, x = 1m\,) = u_{BR} = 0\frac{m}{s}$$

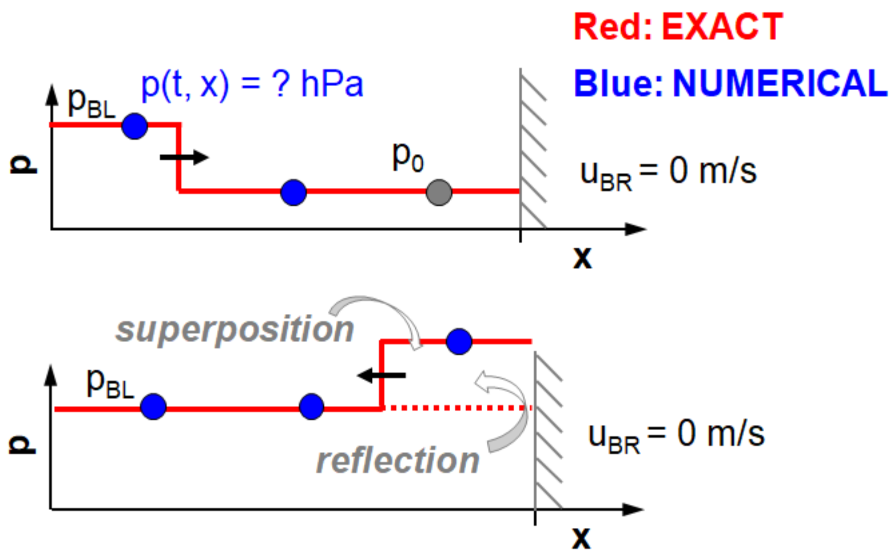

Fig. 20 Validation principle of numerical method by comparison with exact solution of called 'Pipe Shock Test' with reflection on closed right boundary condition

Fig. 20 shows the principle of 'Pipe Shock Test'. All pipe states are set to a constant initial value at initial time $t = 0s$. High pressure at the left boundary p_{BL} causes that sudden discontinuity occurs during first integration step. This discontinuity, so called forward pressure shock, propagates with speed of sound (by gas dynamic equation with speed of sound plus flow velocity $a + u$ to be more exact) from left to right. When the pressure wave reaches the right boundary condition with given zero velocity $u_{BR} = 0\frac{m}{s}$, which is equivalent to a closed orifice, the wave reflects and propagates to the opposite direction. While propagating from right to left, the forward wave superposes with the reverse wave causing an increase in pressure. Fig. 20 shows the forward wave and the first reverse wave, both rectangle shaped when friction is neglected. The friction source term will cause a slight decrease in pressure along x-axis.

3.4.5 Complex vs. Simplified Pipes: 1D Pressure Propagation

Following section shows the comparison of 'complex gas dynamic' equations (3.57) being approximated by the upwind discretization scheme on one hand, and the 'linear acoustic' equations (3.64) on the other hand. Both methods are compared to the exact solution including wall friction.

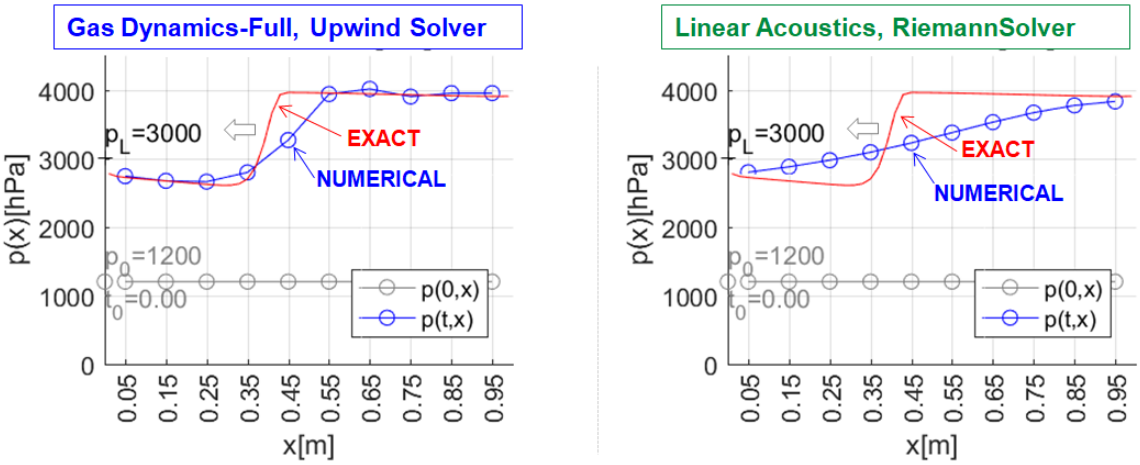

Fig. 21 Pressure distribution along space in 'Pipe Shock Test' after first wave reflection at time t=4ms by using a time step ∆t=50µs

Fig. 21Fig. 21 shows that 'complex gas dynamic' equations (with $\Delta t = 50\mu s,\ \Delta x = 0.1m,\ CFL_{max} = 0.27$) provide more realistic pressure wave propagation even by relatively low number of volume elements.

'Linear acoustic' equations (with $\Delta t = 50\mu s,\ \Delta x = 0.1m,\ CFL_{max} = 0.24$) enable only small pressure changes, but the overall behaviour is similar.

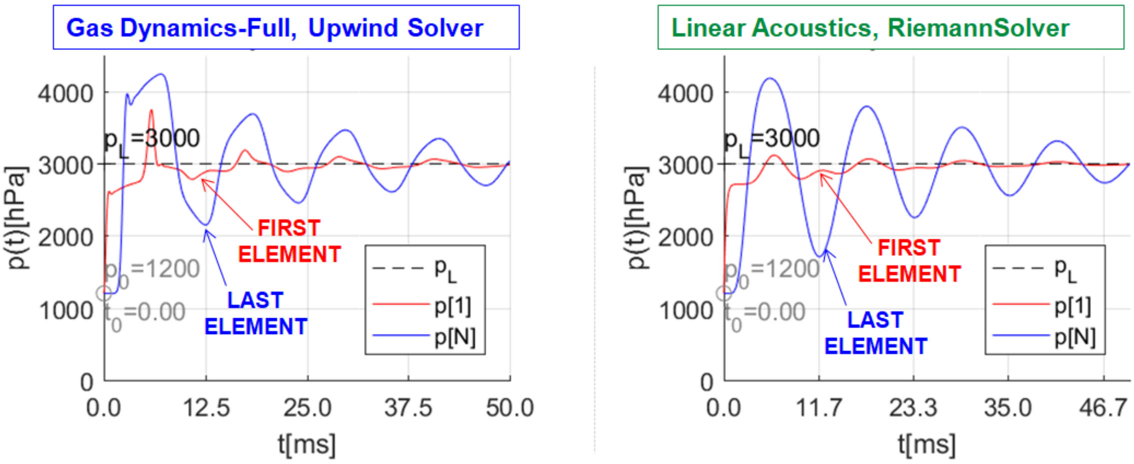

Fig. 22 Time dependent pressure pulsations of first and last pipe elements in 'Pipe Shock Test' by using a time step ∆t=50µs

Fig. 22 shows pulsation of first and last elements, exactly the same results as Fig. 21, but time dependent. The time axis intervals were set to period that corresponds to the eigenfrequency of the pipe by given speed of sound. It can be seen that the pulse frequency matches expected value in both cases. Due to the friction, pulse amplitude goes to zero during time and the pipe pressure will be adapted to pressure on the left boundary condition $p(t = \infty, x) = 3000hPa$.

For real-time applications, it is important to keep integration time step as high as possible to decrease necessary computational time.

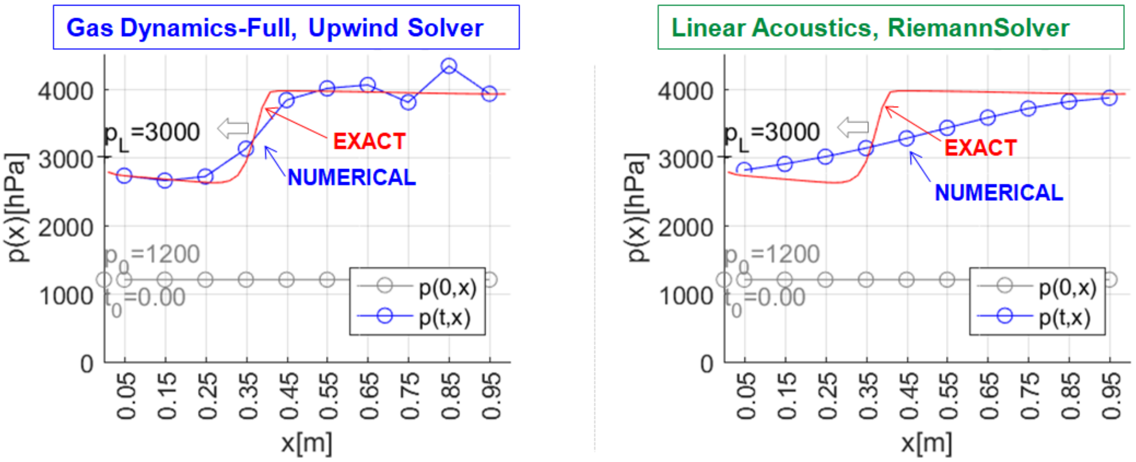

Fig. 23 Pressure distribution along space in 'Pipe Shock Test' after first wave reflection at time t=4ms by using a time step ∆t=165µs

Fig. 23 shows that the upwind solver tends to numerical oscillations in combination with explicit integration method by higher integration time steps (with $\Delta t = 165\mu s$, $\Delta x = 0.1m,\ CFL_{max} = 0.94$). On the other hand, the Riemann solver remains stable even in presence of discontinuities and long integration time steps (with $\Delta t = 165\mu s$, $\Delta x = 0.1m,\ CFL_{max} = 0.78$).

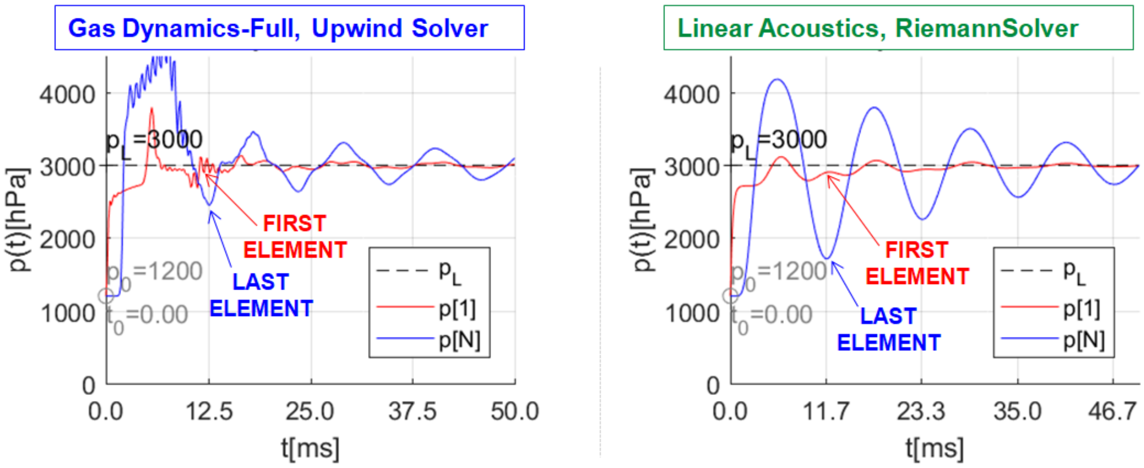

Fig. 24 Time dependent pressure pulsations of first and last pipe elements in 'Pipe Shock Test' by using a time step ∆t=165µs

Fig. 24 shows these results on a time axis.

3.4.6 Complex vs. Simplified Pipes: Real-Time Factor

Real-time factor was estimated offline for all above-described methods for 1D pipe component calculation. The assumptions for estimation are:

Setup / real-time factor estimation **(3.67)**

$ECU\ 240\ MHz$ ... Processor clock frequency

$\Delta t = 300\mu s$ ... Integration time step

$N = 10\ elements$ ... Number of pipe elements

Resulting Real-time factors are:

Results / real-time factor estimation: **(3.68)**

a. gas dynamics-full: $RT = 0.72$

b. gas dynamics-reduced: $RT = 0.24$ … 3 x faster than a

c. linear acoustics: $RT = 0.06$ … 4 x faster than b

… 12 x faster than a

The procedure for estimation of the real-time factor is explained later in section 5.6.

3.4.7 Summary of Pipe Test Results

Both numerical methods used in the complex (section 3.4.1) and the simplified acoustic (see section 3.4.2) 1D pipe component were tested in terms of stability by defining discontinuous initial value problem and compared to their exact solution. The Riemann solver used in the simplified pipe provides better stability with fewer grid points than the previously used upwind scheme. Therefore, higher critical CFL number can be used. The maximum potential of presented simplifications results in a real-time factor RT=0.06. The overall reduction of real-time factor is 12 times in comparison with the complex method.

4 The Engine Development Platform - Experiment

The investigations were performed on a turbocharged, 1.8 litre four-cylinder gasoline engine with both manifold and direct cylinder injection. The experimental engine was installed on an engine test bench with asynchronous machine at Vitesco Technologies in Regensburg for the purpose of model validations. The main data of the engine are described in Tab. 1.

Number of cylinders and arrangement	4 in line
Firing order	1-3-4-2
Displacement	1.8 cm^3
Bore diameter	82.5 mm
Compression ratio	9.5
Rated power	125 kW at 5000 rpm
Maximum torque	300 Nm from 1500 rpm to 4000 rpm
Injection	Direct injection with side injector, manifold injection
Valve train	DOHC, double cam phaser, two-stage variable valve lift at exhaust
Charging system	Single stage turbocharger with mono scroll turbine
Emission class	EU 6

Tab. 1 Main data of the test engine

The direct injection is used at engine start and at higher loads. Depending on the operating state, a single or double injection is possible via the high-pressure injection valves at 200 bar rail pressure. In the partial load range, an intake manifold injection with 10 bar pressure is used.

The overhead intake and exhaust camshafts can be adjusted to improve the gas exchange. The phase adjustment almost eliminates the disadvantages of negative scavenging pressure gradients. In addition, the lift of the exhaust valves can be adjusted in two stages with the valve lift system (see scavenging area – smaller valve lift in Fig. 25 and Fig. 26). As a result, the mutually disadvantageous influencing of the gas exchange between the individual cylinders during exhaust gas stroke is almost completely eliminated.

Fig. 25 shows the engine valve lift curves with definition of phase angle adjustment direction as well as switchable exhaust valve lift. The phasing angle base position for the intake valve is at maximum retard and for the exhaust valve at maximum advanced angle. In the base position, scavenging effects are negligible due to small valve overlap. On the other hand, with maximum adjustment by 30 degrees at exhaust and 60 degrees crank angle at intake valve, the fluid interaction is significant. The fresh air flowing into the cylinders or the exhaust gas flowing out of the cylinders has a specific mass and thus also a mass inertia. When the intake and/or exhaust valves open, these masses are accelerated. The mass inertia causes a reaction that is delayed in relation to the cylinder piston movement. This effect is responsible for the intake of fresh air flowing into the cylinder, even if the piston is already at BDC or beyond. This influence increases with increasing speed and load [43]. Related scavenging effects should be considered by the charge exchange simulation model.

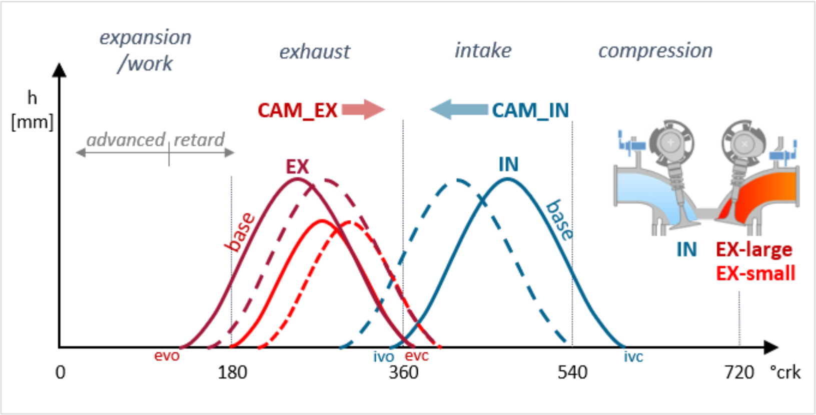

Fig. 25 Engine valve lift curves with phase adjustment and two-stage (small / large) exhaust valve lift option (engine components image source: Vitesco Technologies)

The engine has additionally integrated port flaps in intake manifold to improve the combustion process. This constructive measure is designed to reduce fuel consumption and emissions. With the electronically actuated two-stage port flaps, a more homogeneous mixing of the air-fuel mixture enabled and a stratified charging is implemented [44]. Tumble flaps are active at low engine speeds and loads (see port flap open / closed in Fig. 26).

Further, the engine is equipped with an integrated exhaust manifold cooling duct as a part of a sophisticated thermal management system. Due to the associated cooling of the exhaust gases, the otherwise customary enrichment of the mixture can be dispensed at high speeds. This constructive measure leads to reduction of the fuel consumption. In addition, the cooling water is heated up faster and the engine reaches operating temperature more quickly. Thermal heat exchange effects in exhaust manifold including thermal inertia have significant influence on the turbocharger operating and should therefore be considered in later simulations.

The tested engine has a serial mono scroll turbocharger. The used design has a focus on an optimal low-end torque behaviour. The maximum engine torque of 300 Nm is already available from a speed of 1500 rpm (see Tab. 1 and Fig. 61 in Appendix – Stationary Database). The corresponding maximum boost pressure ratio is 2.0 bar (see Fig. 67 and Fig. 68 in Appendix – Stationary Database). In order to reduce the pressure pulse interaction between cylinders, an ignition sequence manifold was integrated into the cylinder head. In addition to reducing the gas exchange work to be performed, the response of the turbocharger is improved. With this measure, a higher torque is achieved at the same speed. The interaction of pressure pulsations in exhaust manifold was by these constructive measures, but is still not negligible with respect to the turbocharger performance and the engine filling behaviour.

In addition to the basic functionality, further flow control elements are installed in the exhaust gas turbocharger. One element is the wastegate, which creates a bypass for the turbine (see turbine and wastegate in Fig. 26). When the wastegate is closed, the entire flow of exhaust gas is directed through the turbine. Through the opening of the wastegate, part of the exhaust gas is fed directly into the exhaust system. Since the provided boost pressure is derived from the power balance at the turbocharger, it can be controlled in this way. The electronically actuated boost pressure control enables optimal regulation of the boost pressure even in the partial load range with the aim of saving fuel [45]. During the engine warm-up phase, the temperature in front of the catalytic converter is increased by actively opening the wastegate. The cold start emissions can be reduced in this way.

On the compressor stage of the turbocharger, there is a recirculation valve (blow-off) valve (see RCL-valve in Fig. 26). Similar to the wastegate functionality, the air recirculation valve serves to divert accumulated air past the compressor and direct it back to the suction side. This becomes necessary when the throttle valve closes at high turbocharger speeds. A high dynamic pressure is created behind the compressor, which cannot escape. As a result, the compressor wheel is severely braked in overrun mode. To avoid the damage of components due high mechanical loads, recirculation valve is opened.

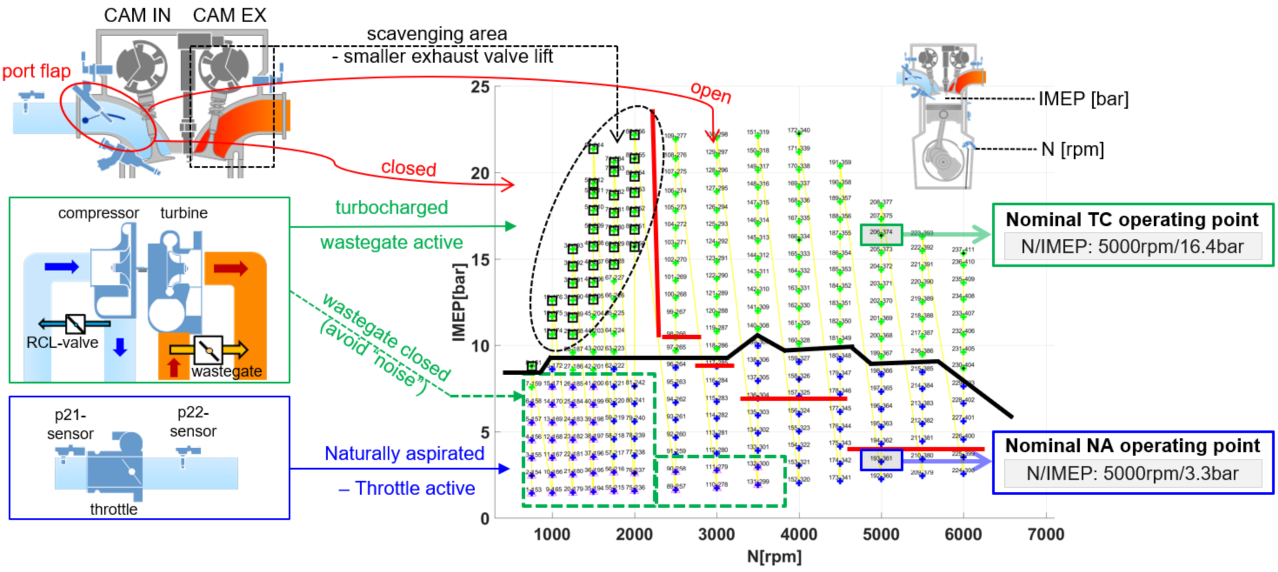

Fig. 26 Engine configuration with actuator positions during experiment (engine components image source: Vitesco Technologies)

The engine load is mainly regulated by the throttle valve actuator during naturally aspirated (NA) operation and by the wastegate during the turbocharged (TC) operating conditions (see throttle and wastegate in Fig. 26). The interaction between throttle and wastegate is explained in section 4.2.2 and 4.2.3 in more detail. For the purpose of further analysis of engine operation, a nominal throttle regulated operating point defined as follows:

Intake mass flow	$\dot{m}_{int,NA} = 99\ kg/h$
Effective throttle area	$A_{Eff,TH,NA} = 1\ cm^2$
Pressure upstream throttle	$p_{u,NA} = 1\ bar$
Pressure downstream throttle	$p_{d,NA} = 0.56\ bar$

Temperature upstream throttle	$T_{u,NA} = 30\ °C$

Tab. 2 Nominal naturally aspirated (NA) operating point, N/IMEP: 5000rpm / 3.3bar

and a nominal wastegate regulated operating point as follows:

Mass flow	$\dot{m}_{int,TC} = 397\ kg/h$
Effective throttle area	$A_{Eff,TH,TC} = 20\ cm^2$
Pressure upstream throttle	$p_{u,TC} = 1.813\ bar$
Pressure downstream throttle	$p_{d,TC} = 1.810\ bar$
Temperature upstream throttle	$T_{u,TC} = 30\ °C$

Tab. 3 Nominal turbocharged (TC) operating point, N/IMEP: 5000rpm / 16.4bar

The engine installed on a test bench with an asynchronous machine and was tested under steady-state as well as transient conditions.

4.1 Sensor Positions on Test Bench

To analyse the engine behaviour and interactions between components during engine operation, the engine was equipped with multiple sensors. Fig. 27 shows the sensor positions during the experiment. Sensor positions marked in yellow boxes in Fig. 27 were sampled by the engine automation system named Morpheus. Used engine automation system is suitable only for steady-state validations, since the sample frequency of 10 Hz is relatively low. In addition to this, the signals from engines serial ECU sensors were transferred into the INCA application tool and used for further validations (see green boxes in Fig. 27). The sample frequency of most ECU signal values is connected to engine stroke events each 180°crk, being for example 167Hz at 5000 rpm engine speed. Finally, the signals labelled with grey boxes in Fig. 14 were obtained from test bench high-pressure and low-pressure indication system with 1°crk angle resolution (30kHz at 5000rpm). These signals are very important for further analysis, as they enable validation of engine pressure dynamic behaviour during each working cycle.

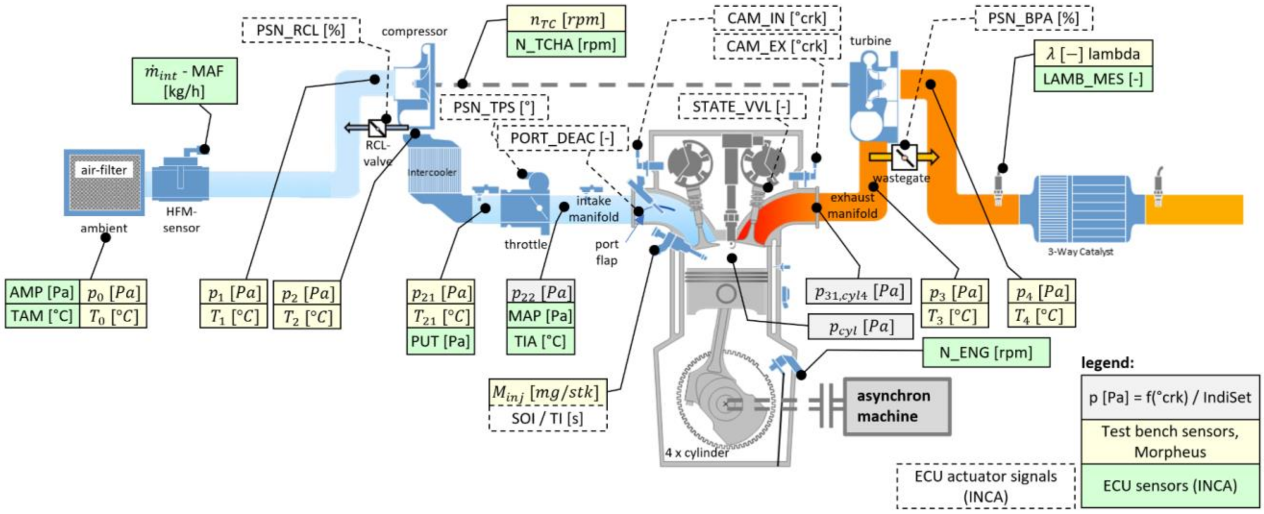

Fig. 27 Sensor positions on engine test bench during experiment (image source: Vitesco Technologies)

Tab. 4 contains the essential measured variables with the sensor specifications used within the engine test bench experiment:

Name	Measurement value	Sensor type		Measurement range / error
$p_0\ [Pa]$	ambient pressure	piezoresistive transducer	absolute	0 – 2bar ± 0.2%
$T_0\ [°C]$	ambient temperature	resistance thermometer	PT100	0 – 200°C ± 0.5°C
$p_1\ [Pa]$	pressure before compressor	piezoresistive transducer	absolute	0 – 2bar ± 0.2%
$T_1\ [°C]$	temperature before compressor	resistance thermometer	PT100	0 – 200°C ± 0.5°C
$p_2\ [Pa]$	pressure after compressor	piezoresistive transducer	absolute	0 – 5bar ± 0.2%
$T_2\ [°C]$	temperature after compressor	resistance thermometer	PT100	0 – 200°C ± 0.5°C
$p_{21}\ [Pa]$	pressure after charge air cooler = pressure upstream throttle	piezoresistive transducer	absolute	0 – 5bar ± 0.2%
$T_{21}\ [°C]$	temperature after charge air cooler	resistance thermometer	PT100	0 – 200°C ± 0.5°C
$p_{22}(t)\ [Pa]$	intake manifold pressure, 1°crk resolution	piezoresistive rel. transducer	Kistler 4050	0 – 5bar ± 0.2%
$p_{cyl}(t)\ [Pa]$	pressure in cylinder, 1°crk resolution	piezoelectric rel. transducer	Kistler 6041A	0 – 200bar ± 1%
$p_{31,cyl4}(t)\ [Pa]$	pressure in exhaust runner of	piezoresistive	Kulite	0 – 10bar ± 0.2%

	cylinder 4, 1°crk resolution	rel. transducer	EWTC-312	
$p_3\ [Pa]$	pressure before turbine	piezoelectric transducer	absolute	0 – 10bar ± 0.2%
$T_3\ [°C]$	temperature before turbine	thermoelement	NiCrNi	0 – 1200°C ± 1.0°C
$p_4\ [Pa]$	pressure after turbine	piezoelectric transducer	absolute	0 – 2bar ± 0.2%
$T_4\ [°C]$	temperature after turbine	thermoelement	NiCrNi	0 – 1200°C ± 1.0°C
$\dot{m}_{inj}\ \left[\frac{kg}{h}\right]$	injected fuel mass flow = fuel consumption	fuel mass flow meter	by AVL	0 – 100 kg/h ± 0.12%
$\lambda\ [-]$	air-fuel ratio before catalyst	exhaust analysis according to Brettschneider formula	AMA system	
$n_{TC}\ [rpm]$	turbocharger shaft speed	inductive transducer	DS1 sensor	1000 – 400.000 rpm
N_ENG [rpm]	ECU engine crank speed	production crank shaft position sensor		
AMP [Pa] / TAM [°C]	ECU ambient pressure / temperature	production absolute pressure sensor combined with temperature sensor		
PUT [Pa]	ECU pressure upstream throttle (= wastegate setpoint)	production absolute pressure		
MAP [Pa] / TIA [°C]	ECU intake manifold pressure (=throttle setpoint) / temperature	production absolute pressure sensor combined with temperature sensor		
MAF [kg/h]	ECU mass flow value, corrected by serial calibration model	hot film air-mass (HFM) sensor		
LAMB_MES [-]	ECU exhaust air-fuel ratio	production lambda (oxygen concentration) sensor		
PV [%]	ECU pedal value	recorded driver actuator request. *See also other actuators in section 5.1, Fig. 30.		

Tab. 4 List of sensors used on engine test bench during experiment

The actuator positions recorded during experiments (see white dashed boxes in Fig. 27) are explained in section 5.1 in more detail since they are used directly as a model input for the offline validation.

4.2 Stationary Measurements

In automotive industry, it is a common practice to display steady-state engine characteristic measurement variables and performance parameters in form of 2-dimensional maps. Selected measured quantities, used for later engine validation, are shown in Fig. 55 to Fig. 78 in Appendix – Stationary Database.

Following sections show the basic validation of engine mass flow balance under steady-state conditions based on the provided experimental data.

4.2.1 Engine Mass Flow and Cylinder Composition

The engine mass conservation is analysed under the assumption of steady-state conditions. This is useful for later comparison of simulation with measurements as well as fast initialization of the engine pressure controllers.

First, the steady-state intake mass flow rate is obtained from the measured fuel consumption (see Fig. 64 and Fig. 65 in Appendix – Stationary Database). The in-cylinder trapped mass consists of air-mass and fuel-mass:

$$M_{cyl,trapp} = M_{Air} + M_{Fuel} \tag{4.69}$$

Since the air contains only about 20% oxygen, the fuel has to be mixed with a relatively large amount of air. The used engine fuel has been analysed in a specialized laboratory. As a result, the stochiometric ratio needed for ideal combustion was estimated:

$$c_S = \frac{M_{Air}}{M_{Fuel}} = 14.2 \quad \ldots\ @\ 630°crk, \lambda = 1 \tag{4.70}$$

With following definition of air-fuel equivalence ratio obtained from engine test bench measurements (see lambda in Fig. 63 in Appendix – Stationary Database)

$$\lambda = \frac{M_{Air}}{M_{Fuel} \cdot c_S} \tag{4.71}$$

, the trapped in-cylinder unburned air-mass can be estimated based on the knowledge of the measured injected fuel mass (see also $\dot{m}_{inj}$ in Fig. 64 in Appendix – Stationary Database).

$$M_{Air,unburned} = \lambda \cdot c_S \cdot M_{inj,fuel} \tag{4.72}$$

Note that this procedure is only valid for SI-engines, for diesel engines another procedure for air mass estimation would be needed.

From the unburned air-mass, the stationary mass flow is of reciprocating engine can be estimated with the known engine speed as

$$\underbrace{\dot{m}_{int}}_{\left[\frac{kg}{s}\right]} = \underbrace{4}_{[cyl]} \cdot \underbrace{0.5}_{\left[\frac{stk}{360^\circ crk}\right]} \cdot \underbrace{M_{Air,unburned}}_{\left[\frac{kg}{stk}\right]} \cdot \underbrace{\frac{N_{eng}}{60}}_{\left[\frac{360^\circ crk}{s}\right]} \tag{4.73}$$

, where the factor 4 is used to consider engine’s four cylinders and the factor 0.5 refers to every second cycle of a 4-stroke engine being used for injecting fuel (360°crk/720°crk).

To estimate the exhaust mass flow rate, the fuel mass has to be accounted to the previously estimated air mass. The total cylinder trapped mass is estimated as

$$M_{cyl,trapp} = (\lambda \cdot c_S + 1) \cdot M_{inj,fuel} \tag{4.74}$$

and similarly to the intake mass flow, the exhaust mass flow of reciprocating engine is estimated from the trapped mass and engine speed:

$$\underbrace{\dot{m}_{exh}}_{\left[\frac{kg}{s}\right]} = \underbrace{4}_{[cyl]} \cdot \underbrace{0.5}_{\left[\frac{stk}{360^\circ crk}\right]} \cdot \underbrace{M_{cyl,trapp}}_{\left[\frac{kg}{stk}\right]} \cdot \underbrace{\frac{N_{eng}}{60}}_{\left[\frac{360^\circ crk}{s}\right]} \tag{4.75}$$

The resulting intake and exhaust mass flow rate are shown in Fig. 65 and Fig. 66 in Appendix – Stationary Database dependent on the engine speed and engine load.

4.2.2 Estimation of Throttle Valve Opening Area

In naturally aspirated (NA) engine operations, the throttle valve regulates the engine load. Within the engine intake air path, it represents the main flow restriction. For purpose of the engine model, an exact knowledge of the throttle effective flow area at all operating conditions is crucial for correct description of engines flow behaviour. This represents a challenge, because from the electronically actuated throttle valve only the throttle angle is known quite exactly. The throttle effective area is then modelled by the ECU with model specific calibrations. The ECU value for effective throttle area is therefore burdened by deviations. To overcome this problem, effective throttle valve area is estimated based on the analysis of steady-state engine data.

Fig. 28 shows on the left side the intake mass flow obtained from measurements by the application of equation (4.73). In addition to this, the difference between pressure sensors upstream and downstream throttle is needed

$$\Delta p_{TH} = p_{22} - p_{21} \qquad \textbf{(4.76)}$$

On the right side of Fig. 28 is the resulting pressure difference on throttle obtained from equation (4.76). Following definition was used to distinguish between NA and TC operations, including a transition area between them

$$\begin{gathered} p_{22} \geq p_0 \quad \rightarrow \quad TC \\ p_{22} > (p_0 - 70hPa) \quad \wedge \quad p_{22} < (p_0 + 70hPa) \quad \rightarrow \quad transition \\ p_{22} < p_0 \quad \rightarrow \quad NA \end{gathered} \qquad \textbf{(4.77)}$$

The pressure dissipation of nominal NA point is with ca. 0.439bar relatively high in contrast to the nominal TC operation point with 0.013bar pressure difference.

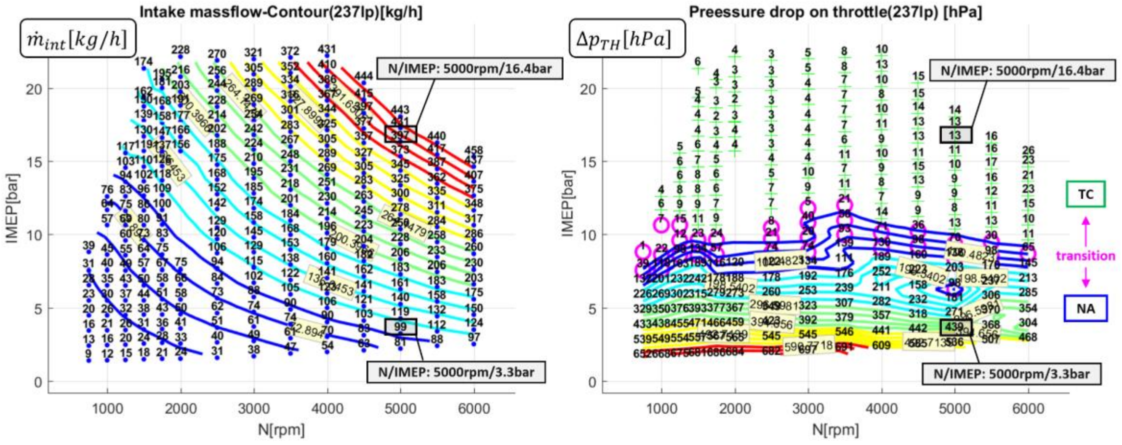

Fig. 28 Intake mass flow and pressure difference at throttle valve obtained from stationary experiment

The pressure difference on throttle is expressed in terms of pressure quotient

$$x = \frac{p_d}{p_u} = \frac{p_{22}}{p_{21}} \tag{4.78}$$

and used to transfer the measured data into coordinates of Saint-Venant flow function for compressible flow (based on equation (3.31))

$$\psi(x) = \sqrt{\frac{\kappa}{\kappa - 1} \cdot \left(x^{\frac{2}{\kappa}} - x^{\frac{\kappa+1}{\kappa}}\right)} \tag{4.79}$$

Fig. 29 shows the measured data in coordinates of flow function obtained from equation (4.79). Operating points with lowest engine load, it is with highest pressure difference, reached sonic flow conditions (blue points with $x < x_{cr}$ in Fig. 29). With continuously opening throttle, pressure quotient goes to unity and resulting flow function nears to zero ($x \rightarrow 1 \implies \psi \rightarrow 0$). The nominal NA and TC operating conditions based on definition in Tab. 2 and Tab. 3 are highlighted.

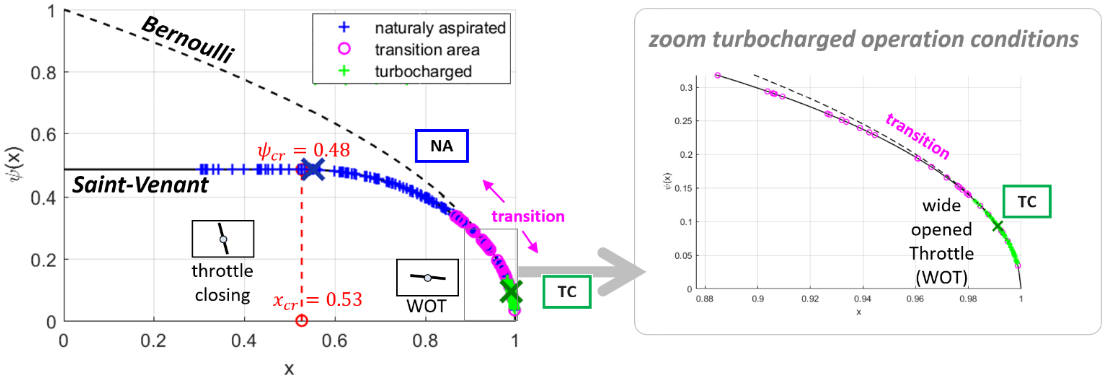

Fig. 29 Pressure quotient vs. flow function with naturally aspirated and turbocharged operating points from stationary engine database

With the assumption of Saint Venant flow (3.31), the effective throttle area opening is estimated as

$$A_{Eff,TH,SV} = A_{TH} \cdot A_{Rel,TH} = \frac{\dot{m}_{int}}{p_{21} \cdot \sqrt{2/(R \cdot T_{21})} \cdot \psi(p_{22}/p_{21})} \tag{4.80}$$

, where $A_{TH} = 0.25 \cdot \pi \cdot d_{TH}^2$ is the geometrical reference area, $A_{Rel,TH}$ is the relative throttle opening and intake flow rate, pressures and temperature are obtained from the steady-state experiment (see Fig. 65, Fig. 69, Fig. 70 and Fig. 75 in Appendix – Stationary Database).

A secondary problem that occurs during the turbocharged (TC) operations is handling of the interaction between throttle valve and wastegate. Due to the wide opening of throttle (WOT), the resulting small pressure difference between the throttle upstream and downstream pressure cannot be used for reliable mass flow estimation as in the case of NA operations. Even a relatively small pressure deviation of 1hPa, caused for example by the measurement errors of upstream and downstream pressure sensors, implies a large mass flow error of 7.5% (assumed from equation (3.31)). For this reason, pressure difference from sensors at TC operations is not used to estimate throttle opening, but wise versa. Similarly, as it is done within engine control unit, a known value of WOT throttle area is assumed based on the nominal TC operating point (see Tab. 3). The values coming from the pressure upstream throttle sensor are dismissed and replaced with correction based on the current steady-state flow rate.

Fig. 29 shows on the right side the detail of TC operating points with pressure quotient near unity ($x \rightarrow 1$). It can be seen that at these conditions incompressible flow according to Bernoulli equation can be used instead of Saint-Venant flow equation (see dashed line compared to full line in Fig. 29). The Bernoulli equation is used in following form

$$\dot{m}_{Ber} = A_{Eff,TH,TC} \cdot \sqrt{2 \cdot \rho_{21} \cdot \Delta p_{TH}} \qquad \textbf{(4.81)}$$

, where $A_{Eff,TH,TC} = 20cm^2$ is assumed at nominal TC conditions from Tab. 3 and upstream density $\rho_{21} = \frac{p_{21}}{R \cdot T_{21}}$ is obtained from measurements. By rearranging of equation (4.81), empirical Borda-Carnot dissipation loss can be obtained

$$\Delta p_{TH,WOT} = \zeta_{TH,WOT} \cdot \frac{1}{2 \cdot \rho_{u,TC}} \cdot \left(\frac{\dot{m}_{Ber}}{A_{Eff,TH,TC}} \right)^2 \qquad \textbf{(4.82)}$$

Upstream density in equation (4.82) was replaced with nominal TC conditions $\rho_{u,TC} = \frac{p_{u,TC}}{R \cdot T_{u,TC}}$ given in Tab. 3. The pressure difference calculated by equation (4.82) is shown in Fig. 30.

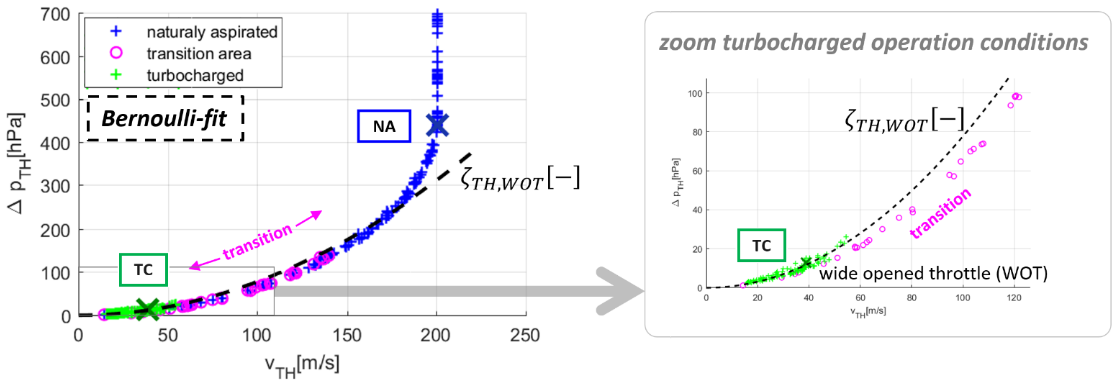

Fig. 30 Flow velocity vs. pressure difference at throttle with naturally aspirated and turbocharged operating points from stationary engine database

The resulting empirical dissipation factor $\zeta_{TH,WOT}$ in connection with the nominal TC operating conditions defined in Tab. 3 are later used in the fast-running simulation model to correct the pressure upstream throttle value.

4.2.3 Estimation of Wastegate Opening Area

Analogically to throttle valve actuator, the position of wastegate actuator is known only as a proportional signal giving relative opening, but exact effective flow area needed for later engine simulations is unknown. To overcome this problem, flow conditions at wastegate obtained from measured steady-state data are analysed in a similar manner like the previous throttle valve analysis. Used input data n_{TC}, $\dot{m}_{exh}$, p_3, p_4 and T_3 are shown in Fig. 59, Fig. 66, Fig. 71, Fig. 72 and Fig. 77 in Appendix – Stationary Database.

In a first step, the flow rate portion throw turbine is estimated from the turbine map-based characteristics (see definition of turbine flow rate characteristics in section 3.3). For this purpose, turbine pressure ratio is needed as an x-coordinate

$$\Pi_T = \frac{p_{3t}}{p_4} \qquad \textbf{(4.83)}$$

, where p_{3t} is the turbine total upstream pressure calculated as

$$p_{3t} = p_3 + \frac{1}{2} \cdot \frac{R \cdot T_3}{p_3} \cdot \left(\frac{\dot{m}_{exh}}{0.25 \cdot \pi \cdot d_{3T}^2} \right)^2 \qquad \textbf{(4.84)}$$

and p_4 is the static downstream pressure. With the assumed turbine inlet diameter $d_{3T} = 43mm$, the dynamic pressure portion is approximately 3.3% of total pressure at nominal TC operating conditions. As an y-coordinate for the turbine characteristics interpolation, the normalized turbocharger shaft speed is needed

$$n_{N,T} = n_{TC} \cdot \sqrt{\frac{T_{3,ref}}{T_3}} \tag{4.85}$$

The resulting reduced turbine mass flow is obtained by 2D interpolation of turbine characteristics

$$\dot{m}_{Red,T} = f_{2D}\left(\Pi_T, n_{N,T}\right) \tag{4.86}$$

and transformed back to the original flow rate coordinated according to the turbocharger map convention

$$\dot{m}_T = \dot{m}_{Red,T} \cdot \frac{p_{3t}}{\sqrt{T_3}} \tag{4.87}$$

To ensure consistency of results, identical turbine characteristics is used for both the estimation of effective wastegate area and the later engine simulations.

Fig. 31 shows the principle of turbine and wastegate flow rate estimation needed for the calculation of effective wastegate opening area during engine operation. The reduced mass flow calculated by equation (4.86) is shown in the coordinates of turbine characteristics at selected engine speed 5000rpm. Resulting portion going throw turbine only, calculated by equation (4.87), is shown on the left side in Fig. 31.

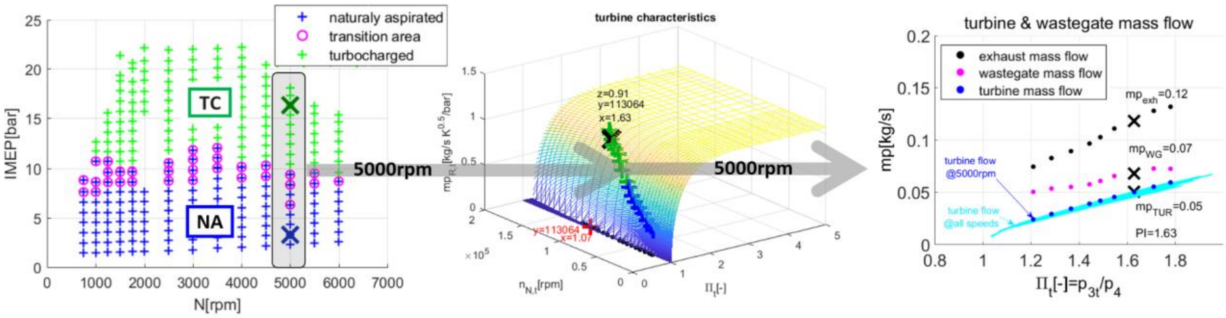

Fig. 31 **Principle of turbine and wastegate mass flow estimation at steady-state conditions**

Having the turbine mass flow portion, the wastegate mass flow portion can be estimated as the result of subtraction from the total exhaust mass flow

$$\dot{m}_{WG} = \dot{m}_{exh} - \dot{m}_{T} \qquad \textbf{(4.88)}$$

Resulting wastegate mass flow portion obtained from equation (4.88) represents ca. 58% of total exhaust mass flow at nominal TC operation point (see magenta points on the left side Fig. 31).

Analogically to the equation (4.80), the resulting effective wastegate area is obtained from the Saint-Venant relation for compressible flow

$$A_{Eff,WG,SV} = A_{WG} \cdot A_{Rel,WG} = \frac{\dot{m}_{WG}}{p_3 \cdot \sqrt{2/(R \cdot T_3)} \cdot \psi(p_4/p_3)} \qquad \textbf{(4.89)}$$

, where $A_{WG} = 0.25 \cdot \pi \cdot d_{WG}^2$ is the geometrical wastegate reference area and $A_{Rel,WG}$ is the relative wastegate opening.

With the knowledge of wastegate effective area and the presented relations, initialization of wastegate component in engine model can be done. Even though the presented relations are valid only at steady-state operating conditions, they represent a good initial value when used within the engine wastegate controller even for the purpose of transient simulations.

4.1 Transient Measurements

The engine was equipped with a serial ECU, including a standard engine calibration (mainly look-up table based volumetric efficiency). Signals from ECU were transferred into INCA application tool and recorded by the engine test bench automation system. By this method, sensor values and actuator positions can be used for later offline validation (see also ECU signals in Fig 27 and Tab. 4).

Fig. 32 shows the transient engine operating modes being tested. The pedal value was pressed and released at different engine speeds < 3000 rpm, followed by either change of engine speed (N), or engine load (IMEP). Each sudden load decrease, caused by the closing of the throttle valve is followed by an opening of the recirculation valve (see PSN_RCL in Fig. 27 and Fig. 32) to avoid compressor surging. More details on compressor surging and choking effects, as well as the interaction of the engine with of turbocharger were presented in an article in Mecca 2022 [47].

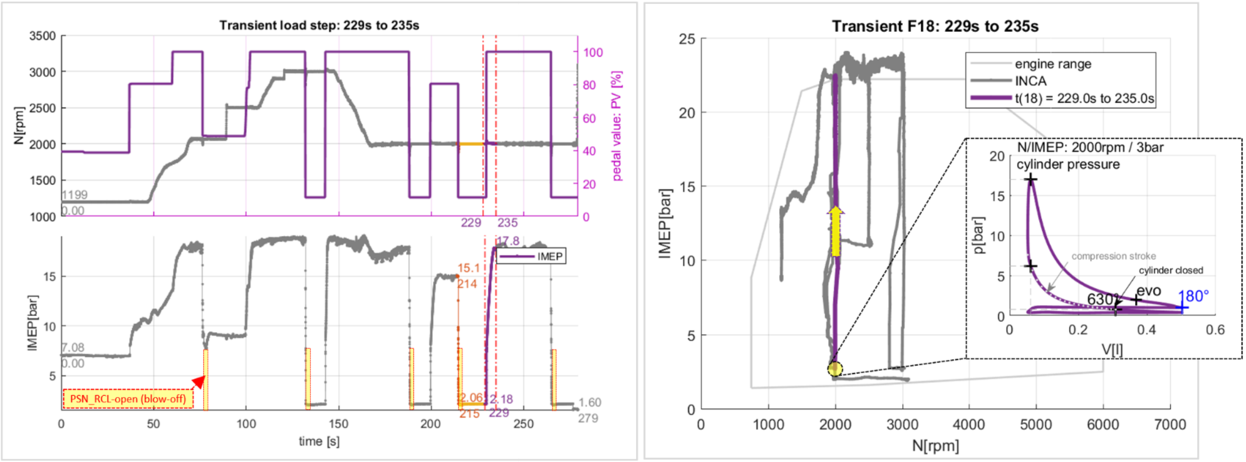

Fig. 32 Engine configuration during transient experiment (selection: transient load step IMEP=2bar to 22bar at constant speed 2000rpm)

After each load decrease, a short interval of few seconds at steady state conditions is set (PV=const., N=const., IMEP=const.). After that, the pedal value is pressed again, followed by another engine load increase.

For simplicity reasons, validations presented in this work are restricted a short interval between 229s and 235s (duration=6s) of the entire experiment. The selected interval represents a sudden load increase (IMEP=2bar → 22bar) at constant engine speed N=2000rpm.

5 SI-Engine Process and Gas Exchange Model

The engine process of 4-cylinder, turbocharged, SI-engine is described by thermodynamic 1D and 0D simulation. The newly developed engine model is intended to extend/replace older look-up table-based ECU prediction models used for engine control purpose.

Database of the experimental engine presented in chapter 4 is used for model offline validation.

5.1 Engine (Model) Control Strategy

Signals from ECU sensors together with information about engine actuator positions, recorded during engine test bench measurements, are used as model inputs. Fig. 33 shows the configuration of sensors and actuators signal flow (red, dashed lines) used for engine torque control. The torque control is realized by managing the in-cylinder air mass, while keeping the air-fuel ratio stoichiometric in order to minimize exhaust emissions. Therefore, the main focus of the model is the correct discretization of the engine air path, whereas the mechanical behaviour is given as input boundary condition from other modules of engine management system. The model actuator signal inputs are (see Fig. 33):

- Driver pedal value (PV [%] – just for info, not used directly as input)
- Throttle valve actuator position (opening angle PSN_TPS [°] or A_REL_TH [-])
- Boost pressure actuator position (PSN_BPA [%] – wastegate opening)
- Two stage port flap actuator position (PORT_DEAC [OPEN / CLOSE])
- Intake cam phaser actuator position (CAM_IN [°crk])
- Exhaust cam phaser actuator position (CAM_EX [°crk])
- Exhaust valve lift actuator position (STATE_VVL [LARGE / SMALL])
- Compressor recirculation valve actuator position (rel. opening PSN_RCL [%])
- Injection event start time and duration (SOI [s] / TI [s])

The driver request to accelerate or decelerate the car is expressed by a pedal value (PV = 0 to 100%). The pedal value is then transformed into the torque setpoint and later into manifold pressure setpoint. The objective of presented engine model is then prediction of trapped in-cylinder air mass to enable exact injection of fuel for next combustion event. The thermodynamic conditions of charge exchange are being observed sensors, giving feedback to the engine control. Following ECU sensor inputs are used by the model (see Fig. 33):

- Engine speed recorded by the crankshaft sensor (N_ENG [rpm])
- Exhaust manifold air-fuel ratio from lambda sensor (λ = LAMB_MES [-])
- Intake pressure upstream throttle (p_{21} = PUT [Pa])
- Intake manifold pressure downstream throttle (p_{22} = MAP [Pa])
- Intake manifold temperature (T_{22} = TIA [°C])

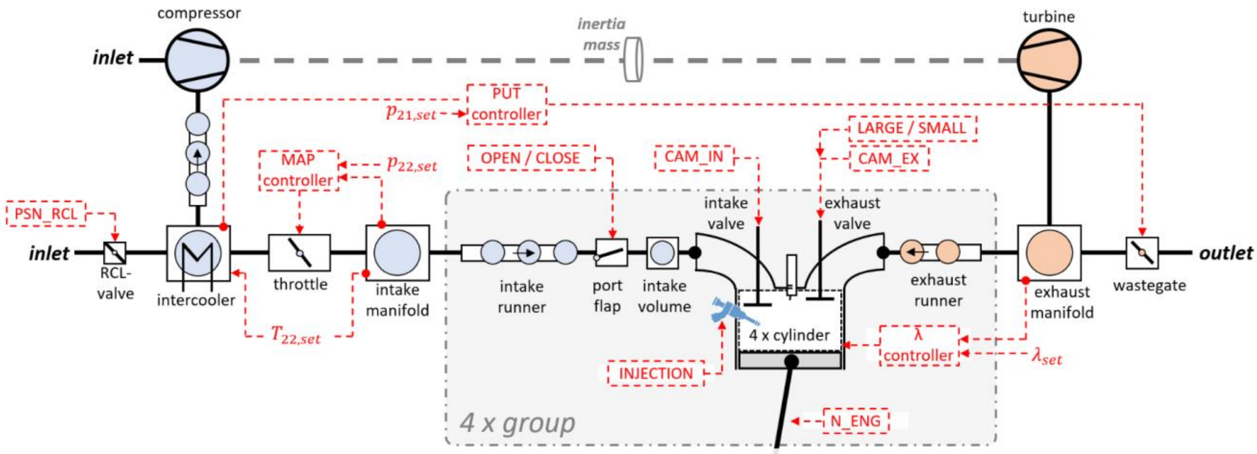

Fig. 33 Sensors and actuators considered within simulation gas exchange model

The pumping of reciprocating pistons is the main determinator of the engine suction behaviour. The engine speed determinates the cylinder piston movement and therefore influences directly the change of thermodynamic state during compression and expansion stroke on one hand, and the flow velocity during exhaust and intake stroke on the other hand. The charge exchange process is then being controlled by the actuators, acting as flow restrictions in intake and exhaust air ducts. In particular, the throttle valve actuator regulates inlet mass flow during naturally aspirated engine operation. The throttle valve opening area is being controlled by a MAP-controller with manifold pressure as a setpoint value (see $p_{22,set}$ in Fig. 33). During turbocharged operating conditions, it is when required intake pressure is higher than ambient, wastegate PUT-controller is activated with pressure upstream throttle setpoint (see $p_{21,set}$ in Fig. 33). Used serial intake manifold pressure sensor is also equipped with an integrated temperature sensor, being another input for model intake temperature adaption (see $T_{22,set}$ in Fig. 33).

Correct determination of thermodynamic intake manifold state is a necessary but not sufficient condition for exact prediction of intake charge exchange. Due to technical limitations, the intake manifold sensor is placed in an area of relatively low-pressure fluctuations at a certain distance from cylinder intake valve. Another aspect is that measurement of cylinder inlet pressure directly before inlet valve of each cylinder individually would be ineffective from the perspective of production costs. For this reason, simulation has to be used to estimate the cylinder gas state as an initial condition for next combustion event. The engine is equipped with a variable two stage port flap actuator between the intake manifold and cylinder, being used as another model input (see Fig. 33, OPEN / CLOSE). The original function of port flap is to increase turbulence intensity and therefore improve combustion efficiency by providing tumble effects [36]. The influence of tumble on gas mixture is not modelled directly because a simplified phenomenological combustion model is used. Only the port flap influence in terms of flow restriction is modelled directly.

The engine is equipped with two hydraulic cam phasers on intake and exhaust cam shaft and with an actuator switching between two different sets of camshaft lobs. Recorded intake and exhaust phaser positions (see CAM_IN / CAM_EX in Fig. 33) are used as model input for variable valve timing (VVT) together with the state of the variable valve lift (VVL) system (see LARGE / SMALL in Fig. 33). This enables correct estimation of effective valve opening area needed for prediction of the gas mixture composition, in particular the scavenging fluid mass and internal exhaust gas ratio (iEGR).

The recorded air-fuel equivalence ratio obtained from engine lambda sensor in exhaust manifold (see λ-controller in Fig. 33) is used as another model input. The target lambda setpoint is usually approximately one, which means that cylinder injectors (see INJECTION in Fig. 33) must deliver an exact fuel mass to reach a stoichiometric ratio. The injected fuel mass is not directly known in engine management system and therefore has to be calculated. The calculation is based on ECU signals for injection start event and injection duration (SOI, TI). This behaviour is reflected by a model build-in PI controller used for model adaption of lambda value.

Last model actuator input to be mentioned is the electronically actuated pressure release valve (see RCL-valve, PSN_RCL in Fig. 33). Its main purpose is to take the load off the turbocharger when the throttle valve is suddenly closed to avoid compressor surging. The measured input signal from RCL-valve is used to parametrize related opening area in the model.

5.2 Model Initialization and Convergence Criteria

The throttle valve and the wastegate are main determinators for the engine load. Correct initialization of the model build-in throttle controller and the wastegate controller (see MAP-controller and PUT-controller in Fig. 33) enables fast model convergence. The initialization is based on the effective opening area guess at steady-state cognitions described in sections 4.2.2. and 4.2.3. Even though the relationships were derived and validated only for stationary engine operating conditions, they are used for transient simulations too. The deviations between model pressure and setpoint pressure values are then corrected by a PI-controller.

The relative throttle valve opening can be obtained directly by application of the equation (4.80)

$$A_{Rel,TH,SV} = \frac{A_{Eff,TH,SV}}{A_{TH}} \tag{5.90}$$

, where the $A_{Eff,TH,SV}$ is the effective flow area resulting from current steady-state mass flow and upstream and downstream pressures and A_{TH} is the geometrical throttle valve area. For the purpose of fast-running simulations, the equation (4.80) and (5.90) can be further simplified. When the engine is in naturally aspirated (NA) operating mode defined according to condition (4.77), nominal flow conditions according to Tab. 2 are assumed in a first step. The resulting relative throttle opening area is then a product of relative area at nominal conditions and scaling factors between current conditions and nominal conditions:

$$A_{Rel,TH,FAST} = \underbrace{\frac{A_{Eff,TH,NA}}{A_{TH}}}_{A_{Rel,TH,NA}} \cdot \underbrace{\frac{\dot{m}_{int}}{\dot{m}_{int,NA}}}_{k_{mp}} \cdot \underbrace{\frac{p_{u,NA}}{p_u}}_{k_{pu}} \cdot \underbrace{\frac{\psi_{NA}}{\psi(p_d/p_u)}}_{k_{psi}} \cdot \underbrace{\cancel{\sqrt{\frac{T_u}{T_{u,NA}}}}}_{k_{Tu}} \tag{5.91}$$

The scaling factors in equation (5.91) have following meaning:

- k_{mp} … scaling of engine mass flow based on current in-cylinder air mass and engine speed ($\dot{m}_{int} = MAF = 4 \cdot 0.5 \cdot M_{air,u} \cdot \frac{N_{eng}}{60}$), steady-state assumption
- k_{pu} … scale factor for pressure upstream throttle $p_u = PUT_{SP}$
- k_{psi} … scale factor for flow function with current pressure quotient $x = p_d/p_u = MAP_{SP}/PUT_{SP}$
- k_{Tu} … scale factor for upstream temperature can be neglected because $T_u = T_{21} \cong 30°C = T_{u,NA}$

Each of the scaling factors can be checked separately on plausibility based on the validity range obtained from stationary database. The scaling factor for upstream temperature can be neglected, because temperature after intercooler being regulated to 30°C by the thermo-management system (see T_{21} in Fig. 75 in Appendix – Stationary Database). Fig. 34 shows that the effective area obtained by rearranging of the Saint-Venant flow function ($A_{Rel,TH,SV}$ from equation (4.80) and (5.90)) is almost same like the effective area obtained by scaling of nominal NA conditions ($A_{Rel,TH,FAST}$ from equation (5.91)). The relative deviation between them is smaller than 3%.

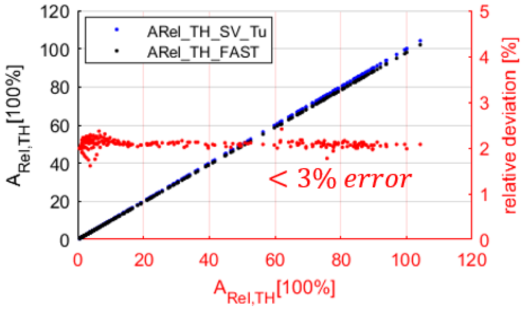

Fig. 34 Relative throttle valve area estimated from Saint-Venant formula compared to fast evaluation by the use of scaling factors

The prediction of relative wastegate opening area, needed for initialization of PUT-controller, is done analogically to the previously shown estimation of throttle valve area.

As it was already explained in section 4.2.2, the pressure difference between pressure upstream (PUT-sensor) and downstream throttle (MAP-sensor) is relatively small at TC conditions and therefore, due to measurement errors, unreliable. For this reason, the sensor value from PUT-sensor is not used as a model setpoint for model controller adaption at TC conditions. Instead, the value from MAP-sensor is used and corrected with the empirical Borda-Carnot dissipation loss $\Delta p_{TH,WOT}$ obtained from equation (4.82)

$$p_u = p_d + \Delta p_{TH,WOT}$$

$$PUT_{SP} = MAP_{SP} + \zeta_{TH,WOT} \cdot \frac{1}{2 \cdot \rho_{u,TC}} \cdot \left(\frac{MAF}{A_{Eff,TH,TC}} \right)^2 \qquad \textbf{(5.92)}$$

Both the Borda-Carnot dissipation coefficient $\zeta_{TH,WOT} = const.$ and the nominal density at TC operating conditions $\rho_{u,TC} = const.$ were obtained from stationary database and are constant over the entire engine operating range.

Fig. 35 shows an example of pressure setpoints with related throttle and wastegate opening predictions during engine load variation at 5000rpm. It can be seen that both the throttle valve and wastegate are active (did not reach threshold) during the load variation.

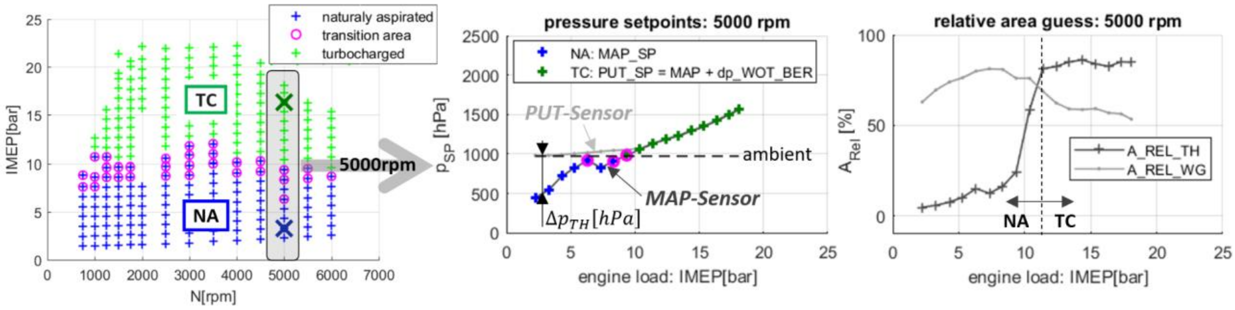

Fig. 35 Model pressure setpoints and initialization of throttle and wastegate

The manifold pressure sensor defines model setpoint at each time of the simulation ($p_{22,set} = MAP_{SP} = MAP\_MES$). The convergence criteria can be expressed as follows:

$$\frac{p_{22,set} - p_{22}}{p_{22,set}} \cdot 100\% < 0.5\% \qquad \textbf{(5.93)}$$

For all operating conditions, the model is seen as being converged (adapted to manifold pressure sensor), when the deviation between measured manifold pressure and simulated manifold pressure is smaller than 0.5%.

5.1 Definition of Model Accuracy Criteria, Main Results

For spark ignited engines, torque control is realized in the ECU by managing the in-cylinder air mass, while keeping the air-fuel ratio stoichiometric in order to minimize exhaust emissions. To fulfill the control objectives, exact prediction of in-cylinder air mass is therefore of key importance [48]. The trapped in-cylinder air mass is therefore the main validation quantity with a required relative deviation to be < 5% compared to measurements.

Measured in-cylinder air mass was calculated from injected fuel by application of equation (4.28) with the Brettschneider based air-fuel ratio. An error of the model is defined as the percentage error between simulation and measurement

$$PE_{MAF} = \frac{M_{Air,unburned}^{simulation} - M_{Air,unburned}^{measurement}}{M_{Air,unburned}^{measurement}} \cdot 100\% \qquad \textbf{(5.94)}$$

Fig. 37 shows the distribution of the percentage error over the stationary engine opiating range. The simulated unburned air-mass refers to model cylinder mixture composition sampled at 630°crk, being the middle of compression stroke (intake valve is already closed).

A simulated load point variation is characterized by increasing engine speed and indicated mean effective pressure (N/IMEP). An overall error is defined as the root of the mean square error

$$RMSE = \sqrt{\frac{1}{k} \cdot \sum_{i=1}^{k} \left(\frac{\overline{y}_i^{simulation} - y_i^{measurement}}{y_i^{measurement}} \right)^2} \cdot 100\% \qquad \textbf{(5.95)}$$

over all engine operating points.

Following table shows the main model deviations compared to stationary database:

Compared variable	**Description**	**Root mean squared error of 234 validation load points / RMSE(234lp)**
$M_{Au}\left[\frac{mg}{stk}\right] \rightarrow [\%]$	(unburned) air-mass error	5.3%err (max 24%)
$n_{TC}[rpm] \rightarrow [\%]$	turbocharger shaft speed error	5%err @TC 30% to 56% @NA
$p_1[hPa] \rightarrow [\%]$	error of inlet pressure before compressor	0.3%err
$p_{22}[hPa] \rightarrow [\%]$	error of manifold pressure (model setpoint!)	0.2%err
$p_{31,cyl4}[hPa] \rightarrow [\%]$	error of pressure in exhaust runner	2.8%err
$p_4[hPa] \rightarrow [\%]$	error of inlet pressure after turbine	1.0%err
$T_1[°C] \rightarrow [\%]$	error of inlet temperature before compressor	0.8%err
$T_{21}[°C] \rightarrow [\%]$	error of temper. after intercooler (model setpoint!)	0.6%err
$T_3[°C] \rightarrow [\%]$	error of temperature before turbine	17.0%err
$T_4[°C] \rightarrow [\%]$	error of temperature after turbine	27.2%err

Tab. 5 Overview of model average deviations compared to stationary measurements (reference model M1: detailed 1D model)

The model deviations listed in Tab. 5 are shown in Fig. 81 to Fig. 91 in Appendix – Model Accuracy of M1.

The overall model accuracy target for in-cylinder air mass, being less than 5%, was reached in the most operating points. Higher deviations occur in particular at low engine speeds. This has mainly two reasons. First reason is simply the definition of the relative error. With a small absolute value $M_{Au} = 100mg\ @IMEP = 1bar$ in denominator, the relative deviation is more restrictive than at high engine loads with high trapped air mass $M_{Au} = 950mg\ @IMEP = 21bar$. Second reason is the violation of steady-state model assumption due to cycle-to-cycle fluctuations of engine operation. This can be expressed as the standard deviation of indicated mean effective pressure (IMEP- covariance). The IMEP-covariance of 100 following cycles is approximately 1.5% during the engine experiment, but reaches 5% to 6% at low loads (see σ_{IMEP} in Fig. 59 in Appendix – Stationary Database). To improve accuracy at low loads, more complex model calibration would be required.

The model shows a good correlation of the turbocharger shaft speed with 5%err at turbocharged operations (see n_{TC} in Tab. 5). Deviations at naturally aspirated operations are with 30% to 56% higher. These deviations must be interpreted with caution, as the reliability of the inductive turbocharger shaft speed sensor is limited at low rotation speeds.

The pressure deviations listed in Tab. 5 show that the convergence criteria for manifold pressure setpoint p_{22} as defined in (5.93) was reached at all operating conditions without any problems. Small deviations of pressures before/after compressor as well as before/after turbine show that pressure resistances in orifice components, dissipation factors at pipe cross section changes and wall frictions are calibrated correctly. Intake temperatures, determining the cylinder inlet density and thus filling behaviour, show also a very good agreement with measurements. Exhaust temperatures show a relatively high deviations, but further recalibration of exhaust wall heat transfer and related phenomena are out of the scope of this work.

Presented model accuracy status represents a baseline (model M1) for the next investigations. The objective is to find a best possible trade-off between model accuracy and real-time capability.

5.2 Model M1: “detailed 1D model”

A so called detailed 1D model is defined (see Fig. 36), that fulfils the main accuracy objectives. The transient flow in intake and exhaust ducts is described by mass, momentum and energy conservation laws described in section 3.4.1 (see 1D gas dynamics - full). Principles of the causal modelling technique, described in section 3.1 (Numerical solver), are used to connect components having thermodynamic state with components providing fluxes. This enables a high level of modularity for potential modification to different engine types and configurations.

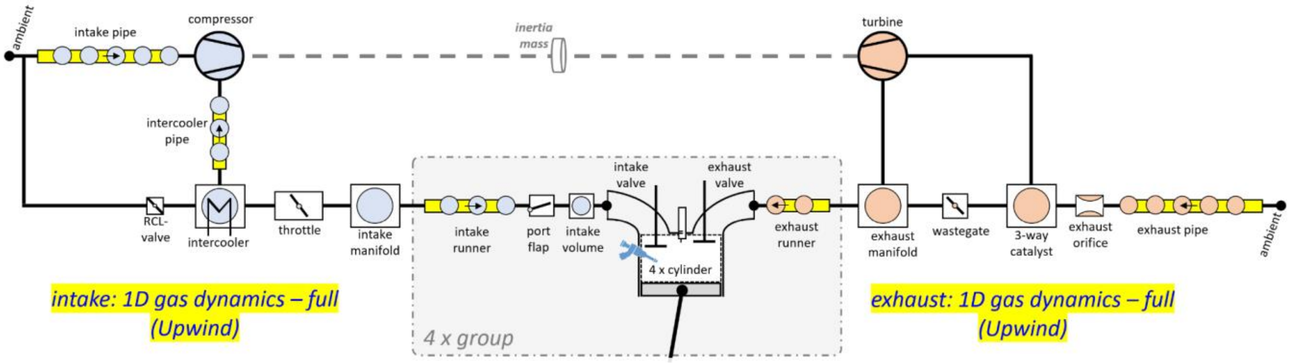

Fig. 36 Layout of detailed 1D model (M1: 234 ODEs, ∆t=30µs, RT=41, RMSE=5.3%err)

Volume components presented in section 3.2.1 describe the engines intercooler, intake manifold and a small intake volume before the cylinder inlet. The intercooler volume is calibrated with a high wall heat transfer coefficient $\alpha_{H,intercooler} = 1000\frac{W}{m^2K}$ and a given wall heat temperature $T_{Wall} = ca. 30°C$. This simple method ensures correct model adaption to the temperature after intercooler, being regulated by engines thermo-management system. The cylinders are modelled by 0D thermodynamic volume extended with phenomenological combustion heat release and a heat transfer model (see cylinder component in section 3.2.2). On the exhaust side, exhaust manifold volume with the heat transfer model represents the engines cylinder head integrated, water cooled, exhaust manifold. Volume components and pipe elements with thermodynamic state (marked as a filled circle in Fig. 36) are connected with orifice components described in section 3.2.3. Basic calibration of pressure resistances in intake and exhaust manifold ducts and the heat transfer calibration was done based on available stationary measurement database.

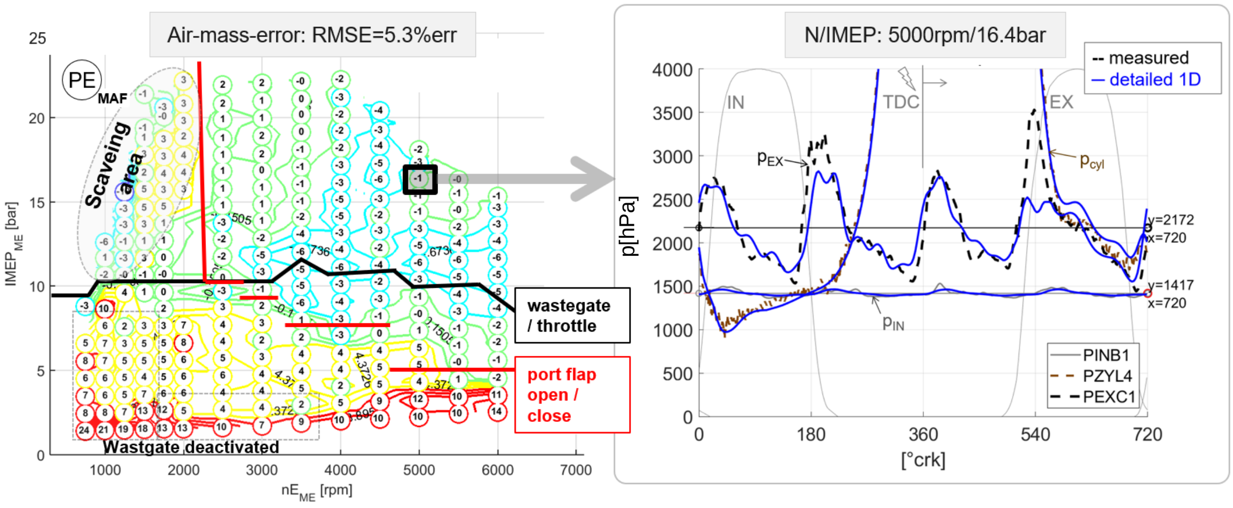

Fig. 37 Left: air mass accuracy of detailed 1D model compared to steady state measurements (M1: 234 ODEs, Δt=30µs, RT=41, RMSE=5.3%err)

Right: intake, cylinder and exhaust pressures compared to experiment

Fig. 37 shows left the model air-mass accuracy as defined section 5.1. The model provides good filling accuracy (RMSE=5.3%err) with some exceptions at scavenging area and at low loads as already explained in previous section.

Fig. 37 right demonstrates the model capability to predict the high-frequency phenomena. The crank angle resolved intake, cylinder and exhaust pressures show a very good correlation compared to measurements (see also $p_{22}(t)$, $p_{cyl}(t)$ and $p_{31,cyl4}(t)$ in section 4.1 Sensor Positions on Test Bench).

However, the transient 1D flow in pipes shows to be the most time consulting part of the numeric solution. The limiting components are four exhaust runners between exhaust valve and exhaust manifold. High temperature of exhaust gasses implies a high local speed of sound ($a = \sqrt{\kappa \cdot R \cdot T}$). This, in combination to small length of exhaust runners, results in a relatively small integration time step needed to satisfy the Courant-Lewy-Friedrichs stability condition [29] [31]

$$CFL = \frac{(a + |u|) \cdot \Delta t}{\Delta x} \overset{!}{\lesssim} 1 \tag{5.96}$$

Required, relatively small, integration time step $\Delta t = 30\mu s$ of detailed 1D model must be set to ensure a stable numerical solution.

5.3 Model M2: “reduced 1D model”

Simplifications described in sections 3.4.1 and 3.4.2 are applied on the model pipe components. The objective of simplifications is to save computational time, while keeping the capability to resolve 1D pressure wave propagation along the engine air path. Reduction of flux terms and caloric properties is applied to the intake pipe and the intercooler pipe (see 1D gas dynamics – reduced in Fig. 38). It was found out that provided simplifications cannot be applied to intake runners without a significant reduction of model accuracy (see 1D gas dynamics – full in Fig. 38) due to scavenging effects and temperature changes resulting from backflow of residual gasses after intake valve opening. All pipe elements on the intake side are solved with the upwind scheme, providing fluxes for the finite volume method integration, and contain all 3 conservation laws for mass, momentum and energy.

A significantly stronger simplification is performed on the exhaust side. The solved system is reduced to only two equations, the mass and the momentum conservation law. Simplifications according to the classical acoustic theory are assumed and the fluxes are solved by the Riemann’s type solver* [31] (see 1D linear acoustics in Fig. 38).

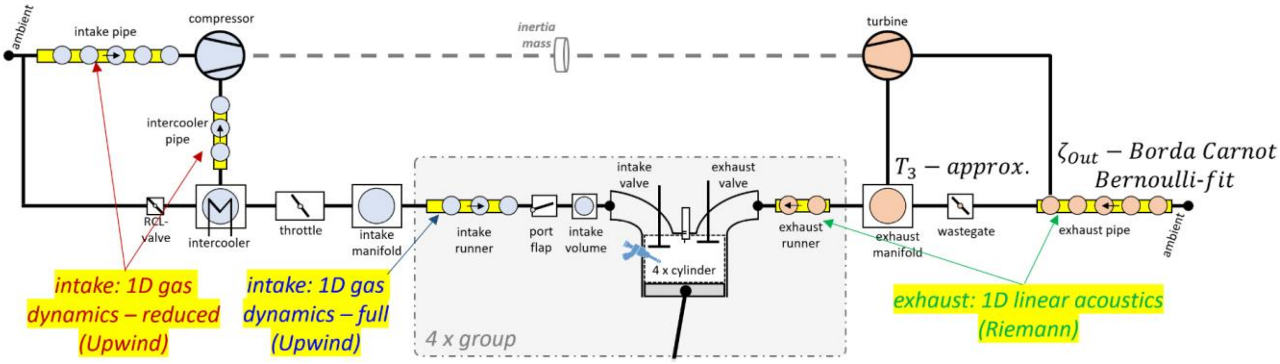

Fig. 38 Layout of the reduced 1D model (M2: 190 ODEs, ∆t=40µs, RT=20, RMSE=5.2%err)

In addition to the reduction of the number of solved equations in the exhaust runner and the exhaust pipe, the model structure after the turbine is further simplified. The previously used catalyst volume in combination to the exhaust orifice is removed from the model. The boundary condition of the exhaust pipe is modified to enable a connection of two fluxes from neighbouring components. This in general is not trivial.

---

*note: with the level of simplifications provided by linear acoustics, several finite volume differential schemes lead to identical result. For example, the Godunov’s methos, Roe’s method etc. Therefore, the label Riemann type solver is used.

As opposed to the volume component with the possibility of connecting (mixing) multiple fluxes, correct connection of multiple fluxes with respect to the momentum conservation is complex. Due to the fact that a same flow direction at all times can be assumed for the turbine and for the wastegate, this problem can be avoided. Losing a part of the modularity and the general validity is the resulting compromise.

The presented modifications on the exhaust side are provided by a recalibration, based on regressions obtained from steady-state measurements. Fig. 39 shows left the pressure difference of the 3-way catalyst and engine exhaust pipe (including a damper) in dependence on steady-state exhaust mass flow. The corresponding pressure resistance, previously calculated by the exhaust orifice component, is now calculated within the exhaust pipe boundary condition (see Bernoulli-fit in Fig. 39). For this purpose, the Borda-Carnot dissipation coefficient ζ_{Out} obtained from measurements is used as a setup parameter for the exhaust pipe boundary condition.

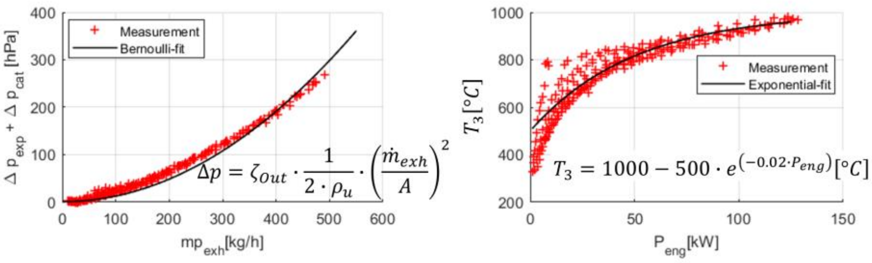

Fig. 39 Empirical regressions used for recalibration of the reduced 1D model

Due to the neglection of energy conservation on exhaust side, an assumption for model temperature must be made. Fig 39. shows right a simple regression used to approximate the temperature in the exhaust runners. Obviously, besides neglecting large temperature ranges during engine’s warm-up and cool-down cycles by load variation at steady-state conditions, transient temperature behaviour cannot be captured by the regression. But within presented steady-state validation, the method provides reasonable results.

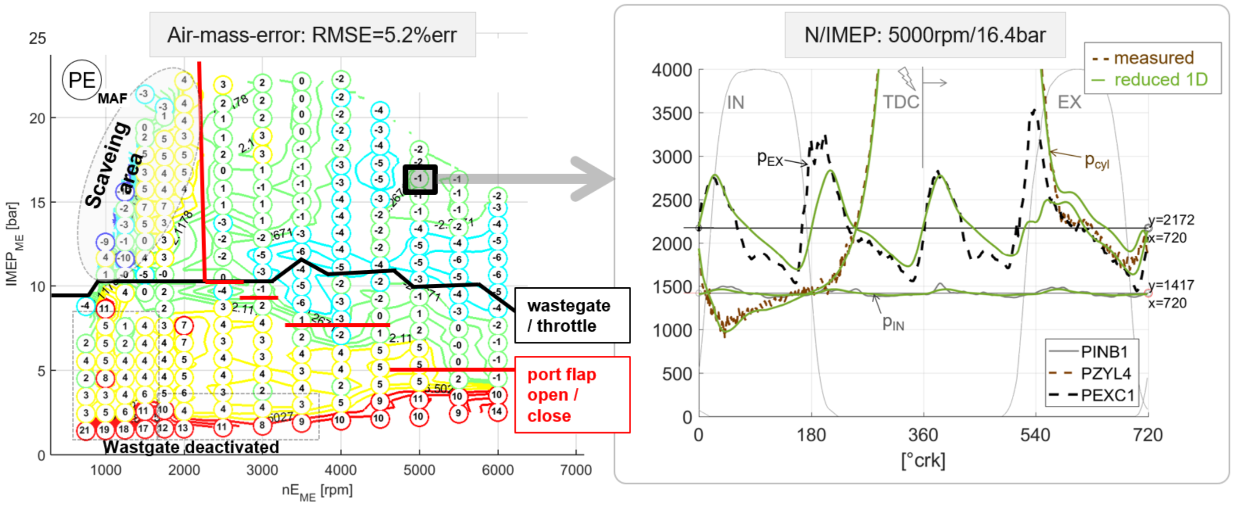

Fig. 40 Left: air-mass accuracy of reduced 1D model (M2: 190 ODEs, ∆t=40µs, RT=20, RMSE=5.2%err)

Right: intake, cylinder and exhaust pressures compared to experiment

Fig. 40 shows left the air-mass accuracy when compared to steady-state experiment. The overall deviation is quite similar to the previously presented detailed 1D model. Due to presented recalibrations, even some minor improvements are observed. The right side of the Fig. 40 shows that the model keeps the capability to capture pressure pulsations with a good correlation to measurements, but higher frequencies disappeared when compared to the detailed model (M1).

Due to the simplifications to linear acoustics and due to the explicit numerical stability of the Riemann’s solver (see also section 3.4.3 Numerical Testing of Pipe Components), an increasing of integration time step to ∆t=40µs is possible. This in combination with the reduction of number of calculated states leads to a reduction of computational time by ca. 50% (RT=41 was reduced to RT=20) when compared to the detailed model.

The real-time factor of reduced 1D model, assessed for the target ECU hardware (240MHz), is with RT=20 still high. To reach the real-time capability, further simplifications are inevitable.

5.4 Model M3: “fast-running 0D model”

The model is further simplified by removing of the pipe components out from the model layout (see Fig. 41). Remaining thermodynamic volumes and orifice components interact based on the principles of the classical 0D filling-emptying method [29].

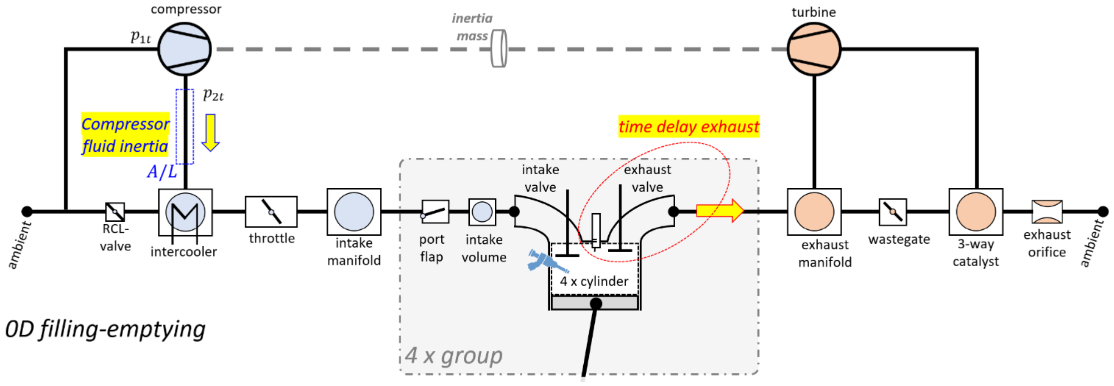

Fig. 41 Layout of fast-running 0D model (M3: 69 ODEs, Δt=300µs, RT=1.7, RMSE=7.4%err)

Nevertheless, the assumption of momentum conservation used within the compressor component provides a certain potential to calibrate the time delay on intake side, and, thus approximate the missing wave propagation. For this purpose, the length and the cross-sectional area of the control fluid volume between the compressor and the intercooler are used as calibration parameters (see compressor fluid inertia in Fig. 41). The assumed differential equation of the compressor acts as a 1st order lag applied on the compressor’s mass flow signal. The principle of the interaction between the compressor map-based interpolation and the accelerated fluid volume was explained in section 3.3.1. This method, already used by Friedrich [9], was successfully tested within previous projects [47].

Similarly to the intake side, a component feature of the exhaust valve, acting as the 1st order time delay of a signal, is used at the exhaust side. The orifice component has the possibility to apply additional differential equation to the solved system instead of calculating the mass flow directly as a functional relation between upstream and downstream states (see also section 3.2.3). This feature, originally intended to increase numerical stability of valves, can be (mis)used to calibrate previously neglected time delays due to wave propagation. Obviously, resulting modelled pressure in the exhaust manifold must be compromised in order to provide either correct backpressure for the cylinders, or the correct boundary pressure pulsations for the turbine component.

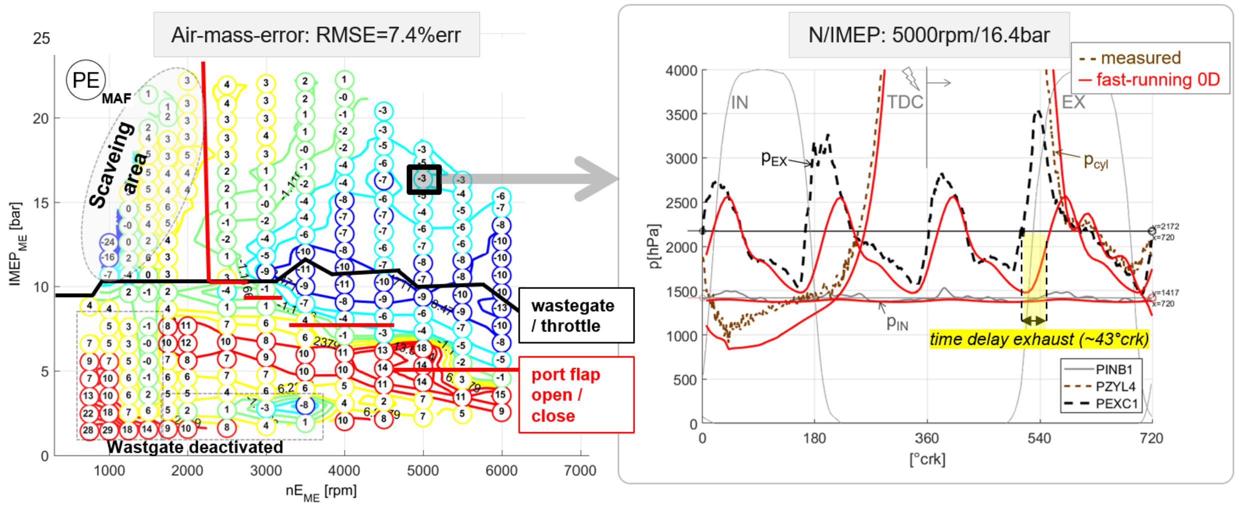

Fig. 42 Left: air-mass accuracy of fast-running 0D model compared to steady state measurements (M3: 69 ODEs, ∆t=300μs, RT=1.7, RMSE=7.4%err)

Right: intake, cylinder and exhaust pressures compared to experiment

Fig. 42 shows left the air-mass deviations obtained from the comparison of the fast-running 0D model with measurements. Due to the simplifications, model predicts lower filling especially in the transition between naturally aspirated and turbocharged operations at high engine speeds. On the other hand, some points in naturally aspirated modes with a closed port-flap condition show eventually higher air-mass than measured. Some points in the scavenging area show an increased deviation too. This was to be expected, because due to the rougher discretization of intake manifold from previously used 17 thermodynamic elements (intake manifold + intake runners + intake volumes) the capability to resolve gas composition is with the used 5 elements (intake manifold + intake volumes) restricted. Despite of strong simplifications, the overall error 7.4%err still seems to be reasonable.

Fig. 42 shows on the right side the resulting pressure pulsations of the fast-running 0D model compared to the measurement sensors. The time delayed increase of exhaust pressure p_3 as a result of exhaust valve calibration can be observed. The calibration focus of the used time delay was to provide best possible solution during valve overlap, while compromising of the pressure pulsations seen at the turbine.

Therefore, the model still has a relatively good capability to describe scavenging effects, including the prediction of the internal recirculation gas ratio (iEGR).

The neglecting of momentum conservation enables to use a significantly higher integration time step $\Delta t = 300\mu s$. This leads in connection with the reduced number of states to a real-time factor RT=1.9 on the target hardware (ECU with 240MHz).

5.5 Model M4: "reduced fast-running 0D model"

To come closer to the real-time capability on the target hardware, further model reduction is needed. The small intake volume before the cylinder in connection with the port-flap orifice represent the limiting factor from the point of view of the numerical stability. They are removed from the model layout (see Fig. 43).

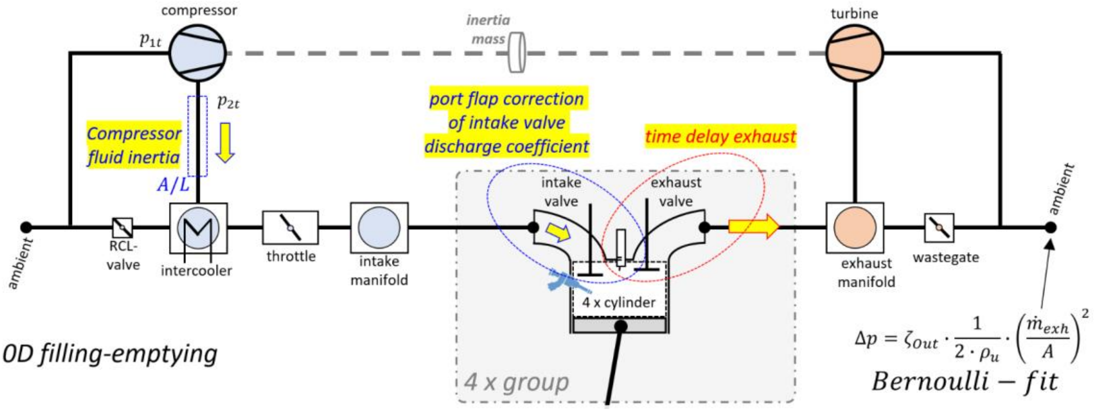

Fig. 43 Layout of reduced fast-running 0D model (M4: 44 ODEs, Δt=300µs, RT=1.1, RMSE=7.4%err)

This again leads to a reduced capability of the prediction of cylinder gas composition (iEGR) and related scavenging effects. On the other hand, the neglected flow resistance of the two-stage port flap component can be preserved in the model by a relatively simple assumption. The effective flow area of the removed port flap component is accounted to the inlet valve characteristics. The equation for two resistances in series

$$A^*_{Eff,IN}(\varphi) = \sqrt{\frac{A^2_{Eff,PortFlap} \cdot A^2_{Eff,IN}(\varphi)}{A^2_{Eff,PortFlap} + A^2_{Eff,IN}(\varphi)}} \tag{5.97}$$

is used to calculate an equivalent effective area [39]. Consequently, this results in one inlet valve characteristics for the opened and one for the closed port flap actuator position.

Finally, the catalyst volume component connected to the exhaust orifice is removed from the model. Instead, the ambient boundary condition is extended by a functional relation for the catalyst and exhaust pipe (damper) resistance obtained from steady-state data fit. This empiric relation was already used in the reduced 1D model (see Fig. 39 left). On the other hand, the temperature T_3 is still part of the numeric solution of the energy conservation law in the exhaust manifold volume (no regression is used).

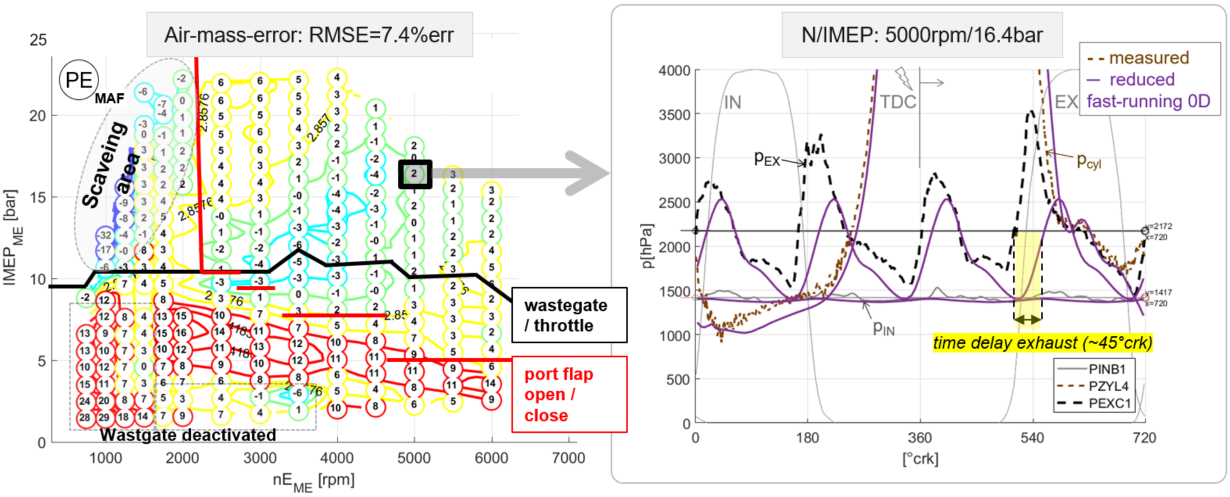

Fig. 44 Left: air mass accuracy of simplified fast-running 0D model compared to steady state measurements (M4: 44 ODEs, ∆t=300µs, RT=1.1, RMSE=7.4%err)

Right: intake, cylinder and exhaust pressures compared to experiment

Fig. 44 shows on the left that the overall air-mass accuracy of the reduced 0D fast-running model remains with 7.4%err comparable with the previous more complex model. Due to the used Bernoulli-based boundary condition representing backpressure of engines outlet, the accuracy at transitions between naturally aspirated and turbocharged operating conditions was even improved at high engine speeds. On the other hand, the model provided higher deviations in the area of deactivated wastegate controller and in the scavenging area.

Even though the model gained additional numerical stability due to removal of the cylinder volume, additional increase of the integration time step $\Delta t = 300\mu s$ cannot be done without further affecting the accuracy. The resulting real-time factor for target hardware (ECU 240MHz) is RT=1.1, while using of the Heun's 2nd order integration time method (see also section 3.1 Numerical solver).

Another engine models with similar level of detail were tested, giving stable results with the use of the Euler's 1st order integration method [47]. This seems to be promising to reach the desired RT<1, but it is out of the scope of the current work. Additional validations of accuracy and stability would be required.

5.6 Estimation of Real-Time Capability

The target hardware for the model implementation is a multicore ECU used in the serial production. Each of the 3 cores has a processor with the clock frequency of 240 MHz. Only one core should be reserved for the air-path model calculation. The hardware is capable to calculate the 32-bit float point arithmetic. The ability to calculate the float point arithmetic is required due to the algorithm nature solving differential equations of mass, momentum and energy. Within the wide range of engine loads and gas thermodynamic states, the variable changes (for example the temperature in exhaust manifold) cannot be captured with a fix point arithmetic.

The real-time capability on engine management system is defined as a ratio of turnaround time for model calculation and the ECU sample period, in which the model is supposed to run. The estimation of necessary turnaround time for each model version can be obtained offline even before going to real-time hardware. The evaluation is based on summarizing of necessary computational operations (additions / subtractions, multiplications, etc.) involved in the code, and taking into account the used integration time step size. The offline estimation formula for real-time factor is:

$$RT = \frac{n_{R-K}}{\Delta t} \cdot \left(N_{add/sub} \cdot T_{add/sub} + N_{mul} \cdot T_{mul} + N_{div} \cdot T_{div} + N_{cpx} \cdot T_{cpx}\right) \quad \textbf{(5.98)}$$

, where the inputs are:

- n_{R-K} $[-]$ … number of Runge-Kutta integration steps = order of ODE's method

- $\Delta t\ [s]$ … integration time step used for the simulation
- $N_i\ [-]$ … number of additions/subtractions, multiplications, divisions and complex operations occurring in code during the evaluation of one integration step
- $T_i\ [s]\ [1/Hz]$ … processor load needed for the particular computational operation measured on the real-time hardware

The first three properties needed for the real-time evaluation (n_{R-K}, Δt and N_i) are related to the software. Finally, the evaluation runtime of each computational operation T_i is required as a hardware property. This value was obtained from measurements of the processor load at particular computational operation (in a for-loop) on the target hardware.

Each part of the model code has been evaluated separately in terms of CPU time consumption based on the evaluation formula (5.98). The procedure has been validated by implementation of the fast-running 0D model on the target hardware and by comparison actual with the offline estimated CPU load. Some model evaluation results were already presented in a previous publication [48]. Both, the principle of the offline evaluation method and some results were presented at the Symposium for Combustion Control 2017 at the RWTH University in Aachen [49].

Tab. 6 shows the number of solved differential equations for each of the previously defined models (M1: detailed 1D model, M2: reduced 1D model, M3: fast-running 0D model and M4: reduced fast-running 0D model).

From the differential equations solved in the code, the number of involved computational operations is obtained (see $N_{add/sub}$, N_{mul} , N_{div} and N_{cpx} in Tab. 6).

Model comparison – estimation of real-time factor					
	M1: **Σ234 ODEs**	**M2:** **Σ190 ODEs**	**M3:** **Σ69 ODEs**	**M4:** **Σ44 ODEs**	**M4$^{a)}$:** **Σ26 ODEs**
	Number of solved ordinary differential equations				
1. Volume (0D)	32	28	32	12	12
2. Cylinder (0D)	16	16	16	16	4
3. Orifice	16	15	16	11	5

4. Turbocharger	3	3	3	3	3
5. Pipe (1D)	165 - complex	126 – simplified	removed	removed	removed
6. other	2	2	2	2	2
	Number of computational operations in code				
$N_{add/sub}$	7493	4506	2367	1598	1025
N_{mul}	8909	4923	2100	1389	861
N_{div}	1868	1636	1252	866	248
N_{cpx}	357	280	258	188	83
	Model assumption for reduction of real-time factor				
a) M4: Σ26ODEs	Calculate only first cylinder with ODEs, last 3 cylinders are assumed as a time-delayed signal of the first cylinder				

Tab. 6 Overview of model components, number of solved differential equations and computational operations in code

Fig. 45 shows the comparison of the resulting real-time factors obtained from equation (5.98) for each of the main models that were previously validated in a wide range of operation conditions.

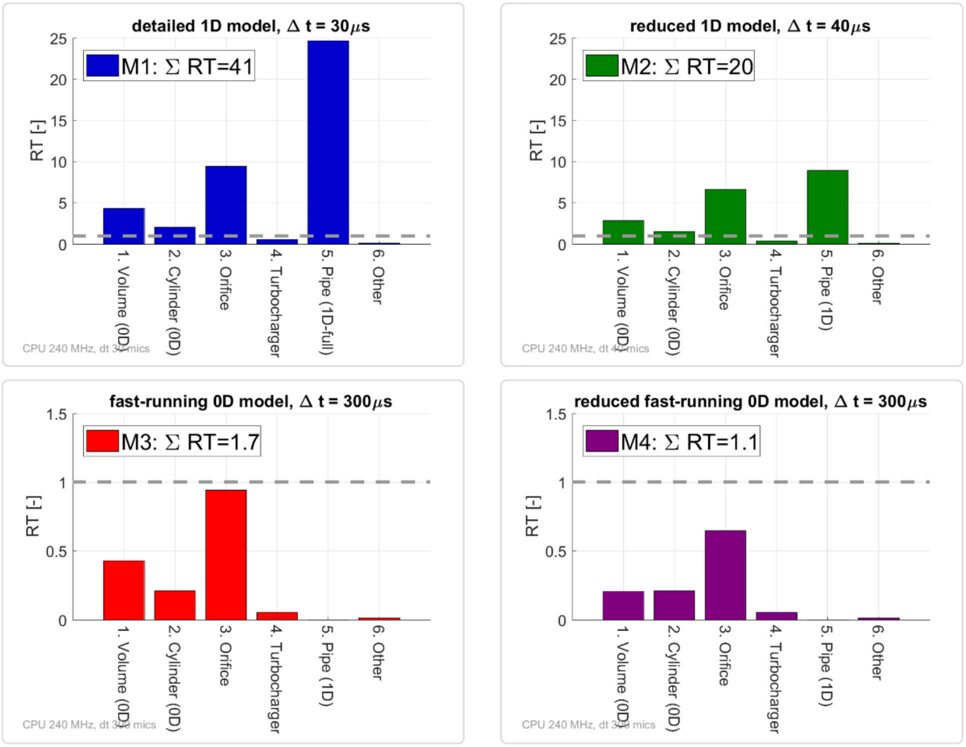

Fig. 45 Comparison of the offline estimated real-time factors on ECU with 240MHz processor for defined models, solved by the Heun's integration method (2nd order Runge-Kutta)

A more detailed overview of the number of differential equations used in the individual model components (intercooler, intake manifold, etc.) and resulting real-time factors are in Tab. 9 in Appendix – ODEs / CPU Load by Components. Fig. 92 and Fig. 93 in Appendix – ODEs / CPU Load by Components show the comparison of an assumed CPU processor load for each individual model component, compared for all models M1, M2, M3 and M4.

5.7 Accuracy Versus Real-Time Capability

Tab. 7 shows the summary of the real-time factor evaluation based on formula (5.98) with the achieved accuracy results.

Model comparison – real-time factor & air-mass-error (target: production ECU 240MHz)					
	M1: **Σ234 ODEs**	**M2:** **Σ190 ODEs**	**M3:** **Σ69 ODEs**	**M4:** **Σ44 ODEs**	**M4$^{a)}$:** **Σ26 ODEs**
CPU 240MHz, Δt=30µs	**RT=41** **RMSE=5.3%**	RT=27	RT=17	RT=11	RT=6
CPU 240MHz, Δt=40µs	instable	**RT=20** **RMSE=5.2%**	RT=13	RT=8	RT=5
CPU 240MHz $\Delta t / \Delta t_{Pipe}$ =100µs / 25µs Local pipe integration	-	**RT=9** **RMSE=10.3 %**	-	-	-
CPU 240MHz, Δt=300µs	instable	instable	**RT=1.7** **RMSE=7.4%**	**RT=1.1** **RMSE=7.4%**	**RT $^{a)}$=0.6**
a) M4: Σ26ODEs	Calculate only first cylinder with ODEs, last 3 cylinders are assumed as a time-delayed signal of the first cylinder				

Tab. 7 Overview of resulting real-time factors and air-mass-errors on the production ECU with 240MHz processor dependent on the number of solved differential equations in the models

The real-time capability of models M1 to M4 on the target hardware was not yet reached. Therefore, some other measures are investigated to reach the real-time capability (RT<1).

The first proposal to reach the real-time capability (see RT$^{a)}$=0.6 in Tab. 7 and Tab. 8) refers to further reduction of the model complexity. The reduced fast-running 0D model is further simplified by using of a symmetry condition for the first engine cylinder (see M4$^{a)}$ Σ26 ODEs in Tab. 6). Only the one of the 4 cylinders is being modelled with differential equations and therefore having an internal state. The last 3 cylinders including intake and exhaust valves are modelled as a time-delayed signal of the first cylinder. Such 1-cylinder model (with 3 fictive time-delayed cylinders) was successfully implemented and validated in a restricted range of transient engine operating conditions and published in Mecca [47]. However, the re-evaluation in a wide range of steady-state engine operating conditions and related validation work is out of the scope of current work.

Model comparison – real-time factor extrapolations (different solver & hardware)					
	M1: **Σ234 ODEs**	**M2:** **Σ190 ODEs**	**M3:** **Σ69 ODEs**	**M4:** **Σ44 ODEs**	**M4$^{a)}$:** **Σ26 ODEs**
CPU 240MHz, Δt=300µs Euler $^{b)}$	instable	instable	**RT $^{b)}$ =0.9**	**RT $^{b)}$ =0.6**	**RT $^{b)}$=0.3**
CPU 350MHz, Δt=300µs Future ECU $^{c)}$	instable	instable	**RT $^{c)}$=1.2**	**RT $^{c)}$=0.8**	**RT $^{c)}$=0.4**
CPU 1GHz, Δt=300µs dSPACE Autobox (HiL) $^{d)}$	instable	instable	**RT $^{d)}$=0.4**	**RT $^{d)}$=0.3**	**RT $^{d)}$=0.1**
	Assumptions for extrapolation of real-time factor				
a) M4: Σ26ODEs	Calculate only first cylinder with ODEs, last 3 cylinders are assumed as a time-delayed signal of the first cylinder				
b) Euler	Use Euler's time integration (1'st order Runge-Kutta with $n_{R-K} = 1$) instead of Heun's integration (2'nd order Runge-Kutta with $n_{R-K} = 2$)				
c) Future ECU	Assume that an ECU with higher clock frequency 350MHz is used instead of the state-of-art production ECU with 240MHz				
d) dSPACE Autobox (HiL)	Model execution on real-time hardware dSpace1005 with 1GHz processor instead of production ECU with 240MHz				

Tab. 8 Overview of extrapolated real-time factors in dependence on the number of solved differential equations in the models

Second proposal to reduce the computational CPU time by 50% is to use the Euler's 1st order integration method instead of the Heun's 2nd order time integration (see RT$^{b)}$ in Tab. 8 and also the numerical solver in section 3.1). This method was successfully tested, giving stable results at selected representative operating points and therefore seems to be promising to reach the desired RT<1. However, additional validations of accuracy and stability in the wide range of engine operations is out of the scope of this work.

As a next step, the real-time factor is extrapolated to show the model performance on different hardware platforms. For simplicity reasons, the real-time factor is scaled by the ratio of processor clock frequencies, without considering of particular hardware architecture. The extrapolation shows, that the reduced fast-running 0D model (see M4: $RT^{c)}$=0.8 in Tab. 8) has potential to be real-time capable on a future ECU with a higher CPU performance of 350MHz (published at SCC Aachen [46]).

Finally, the extrapolation to a state-of-the-art real-time HiL hardware shows that both the fast-running 0D model and the reduced fast-running 0D model (see M3: $RT^{d)}$=0.4 and M4: $RT^{d)}$=0.3 in Tab. 8) are by far real-time capable on the dSpace1005 Autobox hardware.

5.8 Validation with Transient Experiment

The real-time capable, reduced fast-running 0D model with the symmetry assumption to calculate only one of four cylinders with ODEs ($M4^{a)}$: 26 ODEs, Δt=300µs, $RT^{a)}$ =0.6, see in Tab. 7) was validated with the transient experiment. The results are presented in Mecca 2022 [47], giving more details on the interaction between the engine and the turbocharger.

Tab. 46 shows the comparison of the reduced fast-running 0D model (blue line), based on differential equations, with the signals obtained from ECU (black line) during experiment. Both the fast-running model and the ECU model use same actuator signal inputs (pedal value, throttle, wastegate, cam phaser positions etc., see right axis in Fig. 46). The dynamic response on throttle valve opening of both models is very similar.

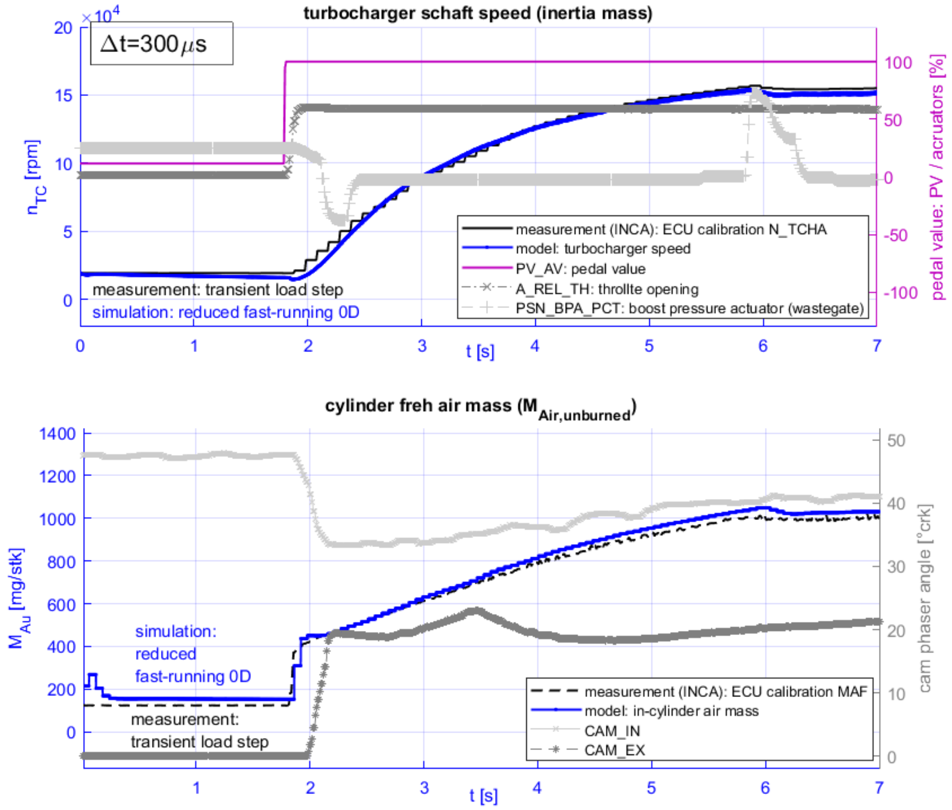

Fig. 46 Validation of reduced fast-running 0D model with ECU model values obtained from transient experiment (M4[a)]: 26 ODEs, Δt=300µs, RT[a)]=0.6, calculates only first cylinder with ODEs)

Fig. 47 shows the that the pressure upstream throttle setpoint could be set very precisely with the fast-running model (measured setpoint is grey dashed line, model value is shown as the green dashed line). Also, the manifold pressure setpoint, being a mean value obtained from ECU sensor, could be set very accurately. Moreover, the fast-running model captures the manifold pressure pulsations during each individual engine cycle correctly (see high-sampled measurements as black dots, compared to the blue full line obtained by the model).

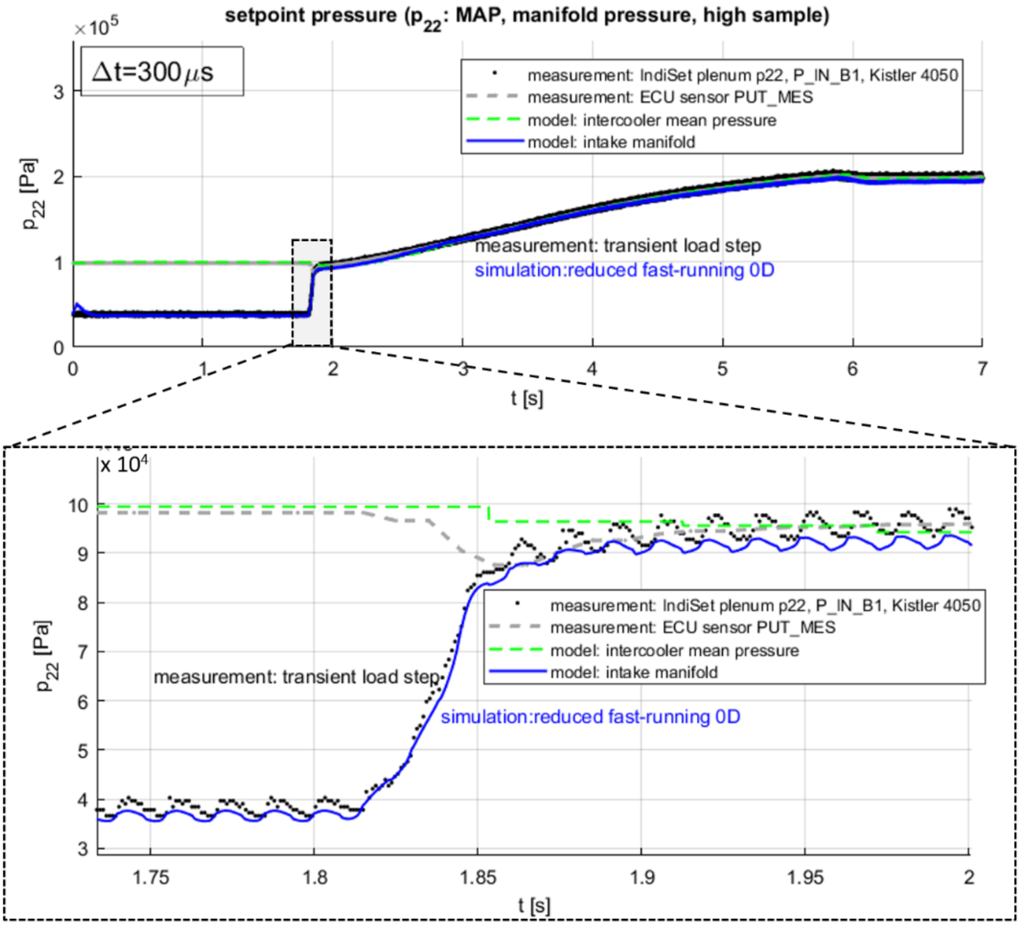

Fig. 47 Intake manifold pressure of reduced fast-running 0D model compared to ECU model values obtained from transient experiment (M4$^{a)}$: 26 ODEs, Δt=300μs, RT$^{a)}$=0.6, calculates only first cylinder with ODEs)

The exhaust pressure shows also very good agreement with measurements obtained by crank angle resolved indication system (Fig. 45) on different time scales. The model provides information on low frequency effects during engine transition from low load to full load (ΔT=7s), as well as quick dynamic response within the transition (ΔT=0.2s) and also crank angle resolved information on each individual engine cycle (ΔT=0.07s).

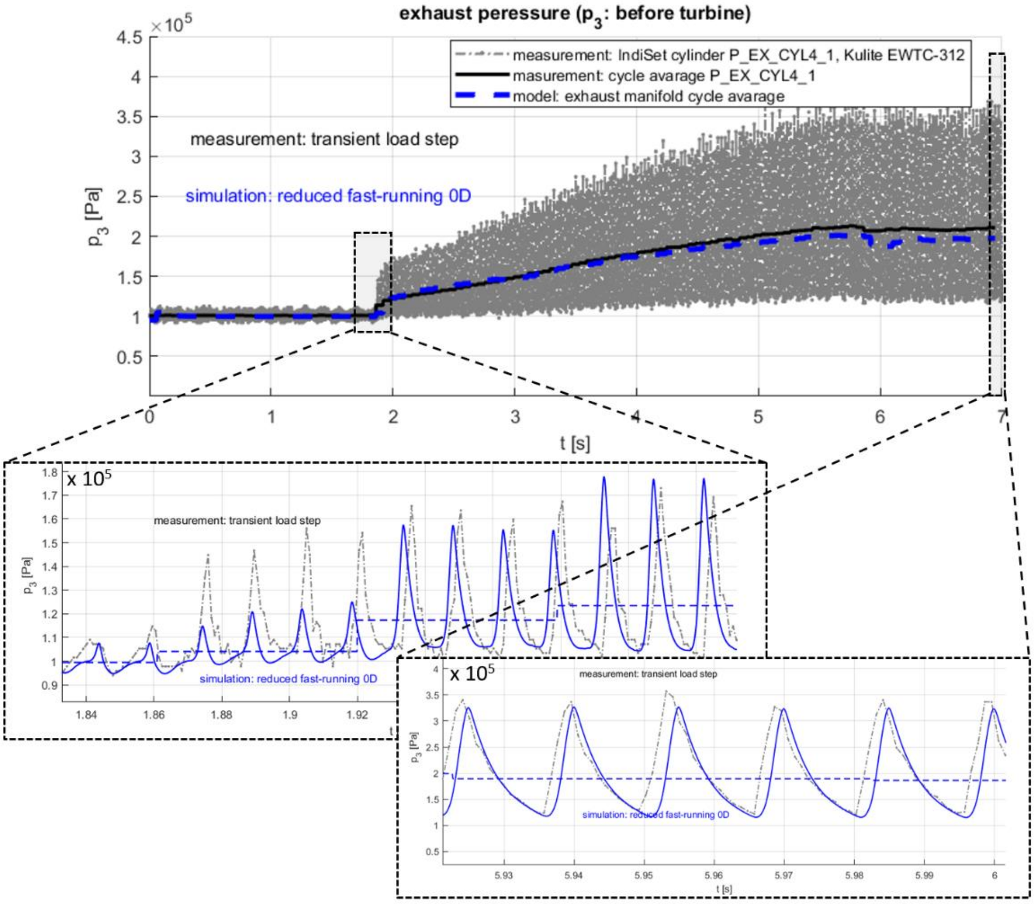

Fig. 48 Exhaust manifold pressure of reduced fast-running 0D model compared to ECU model values obtained from transient experiment (M4[a)]: 26 ODEs, Δt=300μs, RT[a)]=0.6, calculates only first cylinder with ODEs)

The presented model is, despite of strong simplifications, capable to provide high quality information on each individual engine cycle during the engine transition.

6 Conclusions

Modular, physical-based model and simulation environment combining MATLAB, C++ and C code libraries was implemented based on the principles of causal modelling approach (see also 3.1 Numerical Solver). The model provides crank angle resolved information on engine in-cylinder gas mixture and charge exchange including performance of a turbocharger (see also section 2. Objective). Fig. 49 illustrates the accuracy results and the real-time performance on the target hardware dependent on the model complexity. The model complexity is expressed as the number of solved differential equations (ODEs). This shows the feasibility of presented physical models to be real-time capable on a state-of-the-art production ECU. The topics related to the conflict between accuracy and the real-time capability were also published in Mecca 2018 [48] and presented at the Symposium for Combustion control in the RWTH University in Aachen [49].

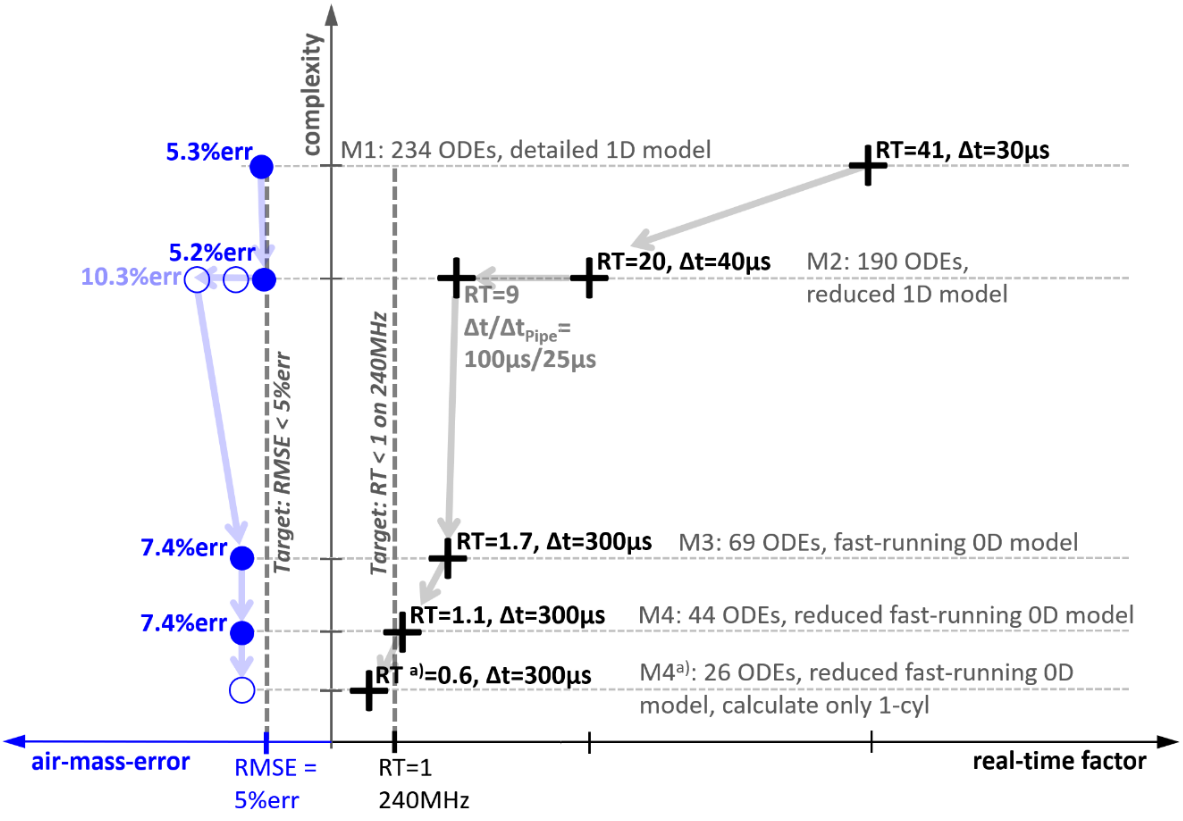

Fig. 49 Air-mass-error and real-time factors on production ECU (240MHz) in dependence on model complexity

The detailed 1D model with 234 solved ODEs provides overall reasonable accuracy on different time scales. It provides also a high level of modularity with a potential to be used for different engine types and configurations. The model requires, however, a small simulation time step of Δt=30μs to satisfy the CFL stability condition in exhaust manifold (see equation (5.96)). This results in a very high turnaround time and the real-time factor RT=41.

To keep the model ability of resolving 1D pressure wave propagation while reducing the required CPU time, the 1D flow in pipe components was strongly simplified. Different simplifications were assumed on intake and exhaust side according to what the accuracy requirements allow within the wide range of engine operating modes. On the intake side, some terms from the evaluation of mass, momentum and energy conservation together with the caloric gas property dependence on temperature are neglected (see section 3.4.1). On the exhaust side, solved system of equations is reduced to mass and momentum conservation based on the assumptions of the linear acoustics (see section 3.4.2). Thanks to the higher stability of the Reimann based solver, used to calculate the 1D linear acoustic pressure pulsations in exhaust, the proposed simplifications enable an increase of the integration time step to Δt=40μs. This leads together with the reduced number of solved equations (190 ODEs) to a 50% reduction of required CPU time. The resulting real-time factor of reduced 1D model is RT=20. The model accuracy remains same in the wide range of validation conditions, the assumed calibrations show even a minor benefit at some points. However, proposed simplifications restrict the model validity to steady-state conditions due to empiric regressions used for calculation of the exhaust temperature. This would probably lead to higher model deviations during engine load transitions. Finally, the numerical solver was modified to overcome the CFL limitations of the 1D model. The integration time step of the global solver was increased to Δt=100μs, while the pipe components are solved with a locally defined integration time step Δt_{Pipe}=25μs (see also local pipe integration in section 3.1). This method provided promising results at some points, giving almost same accuracy while decreasing the real-time factor to RT=9. But the overall air-mass-error was then increased up to 10.3%err. For this reason, model reduction to 0D is inevitable to enable real-time capability on the target hardware.

The neglecting of the pipe components leads to an increase of the overall air-mass-error of the fast-running 0D model to 7.4%err. In particular, lower air-mass than measured is predicted at the transition between naturally aspirated and turbocharged operating conditions at high engine speeds. In contrary to this, higher air-mass than measured was predicted in operating points at lower loads (IMEP<10bar) with the closed port flap actuator position. Because of the fact that one of the development objectives was the reduction of the calibration effort for model configurations, no locally valid calibrations are used. All calibration parameters used are defined as a single value for the entire engine operating range. However, to improve the accuracy of the fast-running 0D model, some local recalibrations would probably be needed. On the costs of the model accuracy, the integration time step can be significantly increased to Δt=300µs. This leads in combination with the reduced number of solved differential equations (69ODEs) to a real-time factor RT=1.7.

Further simplifications to 44 solved ODEs of the defined reduced fast-running 0D model provide a real-time factor RT=1.1, close to real-time capability on the target production ECU with 240MHz clock frequency. The influence of engine port flap on the flow resistance before cylinder inlet was accounted to the intake valve effective area without decreasing of model accuracy. Due to proposed regression used for the calibration of exhaust pipe backpressure, even some accuracy benefits can be observed at the transition between naturally aspirated and turbocharged operating conditions at high engine speeds. On the other hand, the model provided higher deviations in the area of deactivated wastegate controller and in the scavenging area. The deviations go to the bill of the large volumes used for discretization of (in reality complex) intake and exhaust manifolds.

Finally, one solution to reach the real-time capability on target hardware was found. The reduction of solved system to 26 ODEs by calculating only the first cylinder while assuming a symmetry condition for the last three cylinders allows a real-time factor $RT^{a)}$=0.6 (see model $M4^{a)}$ and assumption a) in Tab. 7 in section 5.7). The model shows same accuracy like the previously defined model M4 with 44 ODEs, when tested at selected individual stationary operating points. The model was successfully validated under transient operating conditions, using identical inputs from the engine actuators like the used engine's OEM ECU with serial calibration (see section 5.8).

The proposed real-time capable model shows a good agreement with the values obtained from measurements during the transition (fresh in-cylinder air mass and turbocharger speed shown in Fig. 46). Beside this, the model provides high quality information on each individual engine cycle such as internal recirculation ratio, indicated mean effective pressure and other relevant engine performance indicators without further increase of the model complexity for each individual output value (in contrary to classical data driven models). The comparison of modelled intake and exhaust pressures with high-sampled indication system shows that the model captures correctly the dynamic effects on different time scales from low frequency engine transitions to the crank angle resolved pressure pulsations (see Fig. 47 and Fig. 48). This represents a benefit, for example in comparison to classical mean value models.

Besides the proposal to calculate one out of four cylinders with ODEs, other assumptions were discussed. When using the Euler’s time integration instead of the Heun’s integration method, real-time capability of shown fast-running models can be reached (see fast-running 0D model M3 has $RT^{b)}$=0.9, reduced fast-running 0D model M4 has $RT^{b)}$=0.6 in Tab. 8).

The estimated real-time factor was scaled with processor clock frequency for an assumed future ECU (with 350MHz, M4 has $RT^{c)}$=0.8 in Tab. 8) and for a state-of-art real-time hardware dSpace1005 (with 1GHz, M3 has $RT^{d)}$=0.4 and has $RT^{d)}$=0.3, see Tab. 8). This shows the potential of physical models to extend/replace older data-based algorithms used for the control purpose, taking into account the progress of computational hardware for future ECUs in the time horizon of 5-10 years.

Even when the presented 1D models cannot be real-time capable on the production ECU with 240MHz clock frequency, they represent a good baseline for calibrating the derived fast-running 0D models. On the intake side, the first order time delay defined in compressor model can be used to calibrate previously neglected transport effects. Due to the used physically motivated assumption, based on the momentum conservation, proposed calibration parameters are physically interpretable (see equations (3.45) and (3.46) in section 3.3.1). The compressor model is also published in Mecca 2022 [47], where different inter- and extrapolation methods were compared. Similarly to the intake side, a first order lag behaviour of the exhaust valve is used to calibrate previously neglected transport delay effects (see equation (3.32) in section 3.2.3). All presented models use physically interpretable calibration parameters, valid for the entire engine operating range to keep general validity as high as possible.

Taking into account the above written conclusions, it can be stated that the objectives of the work have been reached. The results related to the physical-based model development in context of real-time applications were also presented at the Symposium for Combustion Control in Aachen 2017 [49] and published in Mecca 2018 [48], and topics related to turbocharger modelling are published in Mecca 2022 [47]. All results were continuously presented internally at Vitesco Technologies in Regensburg and approved for the purpose of this publication.

7 Bibliography

[1] **Merker, G. P., Schwarz, Ch., Stiesch, G., Otto, F.** *Grundlagen Verbrennungsmotoren; Simulation der Gemischbildung, Verbrennung, Schadstoffbildung und Aufladung.* Wiesbaden : Vieweg + Teubner, 2009. pp. 189-354, ISBN 978-3-8348-0740-3.

[2] **Beckmann, R.** *Beitrag zur exakten Füllungssteuerung am aufgeladenen Ottomotor.* Dissertation, Deutschland : Logos Verlag Berlin, Universität Rostock, 2015. pp. 1-6 and pp.96, ISBN 978-3-8325-3930-6.

[3] **Coraddu, A., Kalikatzarakis, M., Theotokatos, G., Geertsma, R. and Oneto, L., Book: Kumar A., A., Kumar, D., Sharma, N., Sonawane, N.,.** *Chapter 6. Physical, data-driven and hybrid approaches to model engine exhaust gas temperatures in operational conditions, Engine Modeling and Simulation.* Chapter 6: Delft-Netherlands, Book: Kanpur-India : Springer Nature Singapore, 2021. pp. 145-187, ISBN 978-981-16-8617-7.

[4] **Kainz, J., Beer, J., Bänfer, O., Nelles, O.** *Einsatz von lokalen Modell-Netzen in einer Motorsteuerung zur Modellierung von Ventiltriebsvariabilitäten.* Essen : Congress "Haus der Technik" Variable Ventilsteuerung, March 3rd-4th, 2009. pp. 3-7.

[5] **Kainz, J., Beer, J., Banfer, O., Nelles, O.** *Local Model Networks, "The Prospective Method for Modeling in Electronic Control Units", ATZ Elektron Worldw 3.* Frankfurt am Main : November 2008ATZelektronik worldwide 3(6), 2008. pp. 36-39, doi:10.1007/BF03242200.

[6] **Macek, J., Polasek, M., Sika, Z., Valasek, M., Florian, M., Vitek, O.** *Transient Engine Model as a Tool for Predictive Control.* Detroit : SAE Technical Paper 2006-01-0659, Czech Technical University in Prague, 2006. pp. 1-17, doi:10.4271/2006-01-0659.

[7] **Roesler, C.** *Echtzeitfähiges physikalisches Motorprozessmodell - Potenziale für die Steuerung eines Pkw-Ottomotors.* Dissertation Berlin : Logos Verlag, Technical University of Berlin, 2013. pp. 71-96 and pp. 163-165, ISBN 978-3-8325-3359-5.

[8] **Ludwig, O.** *Eine Möglichkeit zur echtzeitfähihen, physikalisch-basierten Motorprozessanalyse auf der Grundlage zeitlich fusionierter Messdaten.* Dissertation, Hamburg : Logos Verlag Berlin, Helmut-Schmidt-Universität / Universität der Bundeswehr Hamburg, 2011. pp. 55-174, ISBN 978-3-8325-2792-1.

[9] **Friedrich, I.** *Motorprozess-Simulation in Echtzeit - Grundlagen und Anwendungsmöglichkeiten.* Dissertation, Berlin : Sharker Verlag Aachen, TU-Berlin, 2008. pp. 1-73 and pp. 92, ISBN 987-3-8322-7019-3.

[10] **Isermann, R.** *Engine Modeling and Control, Modeling and Electronic Management of Internal Combustion Engines.* Germany : Springer-Verlag Berlin Heidelberg, TU Darmstadt, 2014. pp. 5-25, ISBN 978-3-642-39933-6.

[11] **Wurzenberger, J. C., Heinzle, R. , Schuemie, A. , Katrasnik, T.** *Crank angle resolved real-time engine simulation - integrated simulation tool chain from office to testbed.* USA : SAE Technical Paper 2009-01-0589, 2009. pp. 112, doi:10.4271/2009-01-0589.

[12] **Jakovlev, S.** *Echtzeitfähige, kurbelwinkelaufgelöste Simulation des Motorstarts.* Dissertation, Braunschweig : Logos Verlag Berlin, Technische Universität Carolo-Wilhelmina zu Braunschweig, Wolkswagen AG, 2014. pp. 1 and pp. 47, ISBN 978-3-8325-3825-5.

[13] **Macek, J., Vitek, O.** *Determination and Representation of Turbocharger Thermodynamic Efficiencies.* USA : SAE Technical Paper 2016-01-1042, Czech Technical University in Prague, 2016. pp. 1-12, doi:10.4271/2016-01-1042.

[14] **Navratil, J., Hnilicka, B., Rawnsley, S.** *WAVE-RT Real Time 1-D Model Running on Engine Controller.* North American User Conference: Tools & Technologies to Meet CAFE Standards 17th April 2013 : Ricardo, 2013. pp. 1-26, www.ricardo.com/wave-rt.

[15] **Kouba, A., Navratil, J., Hnilicka, B., and Niven, P.** *Sensorless Control Strategy Enabled by a Sophisticated Tool Chain.* USA : SAE Technical Paper 2015-01-2847, 2015. pp. 1-6, doi:10.4271/2015-01-2847.

[16] **Kouba, A., Navratil and J., Hnilicka, B. in Book: Liebl J., Beidl C. (eds).** *Engine Control using a Real-Time 1D Engine Model, VPC – Simulation und Test 2015, .* Wiesbaden, Germany : Springer Vieweg, Springer Nature, 2018. pp. 295-309, ISBN 978-3-658-20735-9.

[17] **Ruggiero, A., Montalto, I., Poletto P., Pautasso, E., Mustafaj, K., Servetto E.** *Development and assessment of a Fully-physical 0D Fast Running Model of an E6 passenger car Diesel engine for ECU testing on a Hardware-in-the-loop system.* Torino, Italy : International Congress SIA Powertrain - Rouen, May 21st-22th, SIA Technical Paper, 2014. pp. 1-10, Code R-2014-02-09.

[18] **Cosadia, I., Silvestri, J., Papadimitriou, I., Maroteaux, D., Obernesser, P.** *Traversing the V-Cycle with a Single Simulation - Application to the Renault 1.5 dCi Passenger Car Diesel Engine.* USA : SAE Technical Paper 2013-01-1120, 2013. pp. 1-10, doi:10.4271/2013-01-1120.

[19] **Sellnau, M., Sinnamon, J., Oberdier, L., Dase, C., Quillen, M. V. K., Silvestri, J., Papadimitriou, I.** *Development of a Practical Tool for Residual Gas Estimation in IC Engines.* USA : SAE Technical Paper 2009-01-0695, 2009. pp. 1-10, doi:10.4271/2009-01-0695.

[20] **Papadimitriou, I., Warner, M., Silvestri, J., Lennblad, J., Tabar, S.** *Neural Network Based Fast-Running Engine Models for Control-Oriented Applications.* Detroit, Michigan : SAE Technical Paper 2005-01-0072, 2005. pp. 1-9, doi:10.4271/2005-01-0072.

[21] **Ciesla, C., Keribar, R., Morel, T.** *Engine/Powertrain/Vehicle Modeling Tool Applicable to All Stages of the Design Process, also in: Electronic Engine Control Technologies-PT-73, Electronic Engine Controls 2000: Modeling, Neural Networks.* USA : SAE Technical Paper 2000-01-0934, Gamma Technologies US, 2000. pp. 151-163, doi:10.4271/2000-01-0934.

[22] **Reine, A., Thomas, V., Manz, A.** *Particle Reduced, Efficient Gasoline Engines, Report on new prediction capabilities over regulatory and real driving emissions.* Germany : EUROPEAN COMMISSION, 2020. pp. 1-18, GA # 723954.

[23] **Cipollone, R., Sciarretta, A.** *A New Modeling for the Air and Gas Dynamics in ICE Manifold Oriented to Air-Fuel Ratio Control.* 1999. pp. 1, ASME Paper 99-ICE-170.

[24] **Hendricks, E., Chevalier, A., Jensen, M., Sorenson, S., Trumpy, D. and Asik, J.** *Modelling of the Intake Manifold Filling Dynamics.* Denmark : SAE Technical Paper 960037, Technical University of Denmark, 1996. pp. 1, doi:10.4271/960037.

[25] **Cipollone, R., Sciarretta, A.** *The Quasi-Propagatory Model: A New Approach for Describing Transient Phenomena in Engine Manifolds.* L'Aquila : SAE Technical Paper 2001-01-0579, University of L'Aquila, 2001. pp. 55-63, doi:10.4271/2001-01-0579.

[26] **Cavina, N., Migliore, F., Carmignani, L. and Di Palma, S.** *Development of a Control-Oriented Engine Model Including Wave Action Effects.* Italy : SAE Technical Paper 2009-24-0107, University of Bologna, Piaggio & C. S.p.A, 2009. pp. 1-12, doi:10.4271/2009-24-0107.

[27] **Stockar, S., Canova, M., Guezennec, Y., Torre, A. D., Montenegro, G., Onorati, A.** *Modeling Wave Action Effects in Internal Combustion Engine Air Path Systems: Comparison of Numerical and System Dynamics Approaches.* s.l. : International Journal of Engine Research 14(4): pp. 391-408, 2013. doi:10.1177/1468087412455747.

[28] **Follen, K. M.** *A system dynamics modeling metodology for compressible fluid flow systems with applicatins to internal combustion engines.* USA : Dissertation, The Ohio State University, 2010, pp. 5-40.

[29] **Pischinger, R., Klell, M., Sams, T.** *Thermodynamik der Verbrennungskraftmaschine.* Wien : Springer Verlag Wien, 2009. pp. 1-68 and pp. 309-331, ISBN 978-3211-99276-0.

[30] **Wesseling, P.** *Principles of computational fluid dynamics.* Heidelberg : Springer, 2001. pp. 339-445, ISBN 978-3-642-05145-6.

[31] **LeVeque, R. J.** *Finite volume methods for hyperbolic problems.* United Kingdom : The University of Cambridge, 2004. pp. 1-85 and pp. 291-309, ISBN 0-511-04219-1.

[32] **Gustavsson, E.** *Modelling of Wave Propagation in Combustion Engines.* Lund : Master thesis, Lunds Universitet, 2014. pp. 25-93, ISSN 0282-1990.

[33] **Cipollone, R., Martella, L., Scarpone, L. and Valente, R.** *A New Modeling to Predict the Fluid Dynamic Transient Phenomena in Ice Ducts.* L'Aquila : SAE Technical Paper 2008-01-2389, University of L'Aquila, 2008. pp. 1-8, doi:10.4271/2008-01-2389.

[34] **Touimi, Z. B., Gaid, M. B., Bohbot, J., Dutoya, A.** *From Physical Modeling to Real-Time Simulation: Feed back on the use of Modelica in the engine control development toolchain.* Dresden & Rueil-Malmaison : Proceedings 8th Modelica Conference, March 20th-22th, pp. 763-771, 2011.

[35] **Sommer, R., Halfmann, T., Broz, J.** *Automated behavioral modeling and analytical model-order reduction by application of symbolic circuit analysis for multi-physical systems: Simulation Modelling Practice and Theory.* Ilmenau, Germany : IMMS Institut für Mikroelektronik- und Mechatronik-Systeme gemeinnützige GmbH, Frauenhofer Institute, 2008. pp. 1024–1039, doi:10.1016/j.simpat.2008.04.012.

[36] **Heywood, J. B.** *Internal combustion engines fundamentals.* New York : McGraw-Hill, 1989. pp. 204-304 and pp. 748-764, ISBN 0-07-08637-X.

[37] **Grill, M.** *Objektorientierte Prozessrechnung von Verbrennungsmotoren.* Dissertation, Deutschland : OPUS - Publication Server of the University of Stuttgart, Institut für Verbrennungsmotoren und Kraftfahrwesen der Universität Stuttgart, 2006. pp. 193-230, doi:10.18419/opus-4076.

[38] **Woschni, G.** *A Universally Applicable Equation for the Instantaneous Heat Transfer Coefficient in the Internal Combustion Engine.* Maschinenfabrik Augsburg - Nürnberg AG : SAE Technical Paper 670931, 1967. pp. 1, doi:10.4271/670931.

[39] **Zinner, K., Puscher, H.** *Aufladung von Verbrennungsmotoren - Grundlagen, Berechnungen, Ausführingen.* Berlin, Heilderberg : Springer-Verlag, 4. Auflage, 2021. pp. 26-169, ISBN 978-3-642-28989-7.

[40] **Berndt, R.** *Einfluss eines diabaten Turboladermodells auf die Gesamtprozesssimulation abgasturboaufgeladener PKW-Dieselmotoren.* Berlin : Dissertation, Fakultät V - Verkehrs- und Maschinensysteme, Technische Universitat Berlin, 2009. pp. 24-37 and pp. 53-58, doi:10.14279/depositonce-2313.

[41] **Hiroschi, A., MathWorks, Inc (1994-2022).** *1-D data interpolation (table lookup): User's Guide (r2021b).* s.l. : Retrieved February 14th, 2022 from. pp. 1, https://de.mathworks.com/help/matlab/ref/interp1.html.

[42] **Scharf, J. S.** *Extended Turbocharger Mapping and Engine Simulation.* Germany : Dissertation, Lehrstuhl für Verbrennungskraftmaschinen und Institut für Thermodynamik, RWTH Aachen, 2010. pp. 29, Interne Identifikationsnummern: RWTH-CONV-125328, Datensatz-ID: 63937.

[43] **Mahle GmbH.** *Kapitel 6 Variabilitäten im Ventiltrieb, ATZ/MTZ Fachbuch, Ventiltrieb – Systeme und Komponenten.* Stuttgart : Springer Vieweg, 2013. pp. 145-199, ISBN 978-3-8348-2490-5.

[44] **Basshuysen, R., Schäfer, F.** *Handbuch Verbrennungsmotor - Grundlagen, Komponenten, Systeme, Perspektiven.* Hamm, Deutschland : Springer Vieweg, 7. Auflage, 2002-2015. pp. 676, ISBN 978-3-658-04677-4.

[45] **Schreiber, G.** *Untersuchung von Verbesserungspotentialen hinsichtlich Verbrauch und Drehmoment bei Ottomotoren mit Hilfe 1-dimensionaler Simulationsrechnung.* Deutschland : Dissertation, Technische Universität Kaiserslautern, 2006. pp. 122-134, Intene Diss. Nr. D 386, urn:nbn:de:hbz:386-kluedo-19526.

[46] **Borean, F., Message, S., Morgan, Ch., Neaves, B., Slaney, T.** *2020-2025 Challenges for Combustion Control in Automotive World: Hybridization, Emissions*

and Key Enablers. Jaguar Land Rover, Coventry, UK : Symposium for Combustion Control, June 15th-16th, pp. 145-148, Aachen, 2016.

8 Publications

[47] **Fortl, J., Macek, J.** *Turbocharger Modelling for Fast-Running Transient 0D ICE Simulations.* Prague : MECCA Technical Paper, submitted for review on February 22nd, 2022. pp. 1-18.

[48] **Fortl, J., Beer, J., Keller, J, Macek, J. and Borchsenius, F.** *Physical Model of SI-Engine Process and Gas Exchange for Real-Time Implementation in Engine Management System.* Prague : MECCA Technical Paper, 2018. pp. 11-17, 10.1515/mecdc-2018-0006.

[49] **Fortl, J.** *Presentaion of "Physical Model of SI-Engine Process and Gas Exchange for Real-Time Implementation in Engine Management System" in context of Real-Time Applications.* RWTH Aachen University, Germany : Symposium for Combustion Control, June 28th-29th, 2017. public speach with presentation, pp. 1-22.

1 Appendix – Theory

Warning: Inter- and extrapolation of compressor efficiency should <u>not</u> be used within the simulation program to calculate compressor enthalpy difference:

$$\Delta h_c = \frac{c_{p,int} \cdot T_{1,ref} \cdot \left[\Pi_c^{\frac{\kappa_{int}-1}{\kappa_{int}}} - 1 \right]}{\eta_{sC}\left(\dot{m}_{N,c},\ n_{N,c}\right)} \tag{1.99}$$

A stability problem can occur due to near-zero divisions with $\eta_{sC} \to 0$. Data based cubic spline extrapolation of the efficiency (see Fig. 40 Left) leads to <u>non</u>physical states behind compressor (see Fig. 40 Right). Negative enthalpy difference yields implausible compressor outlet temperatures (for example -130°C).

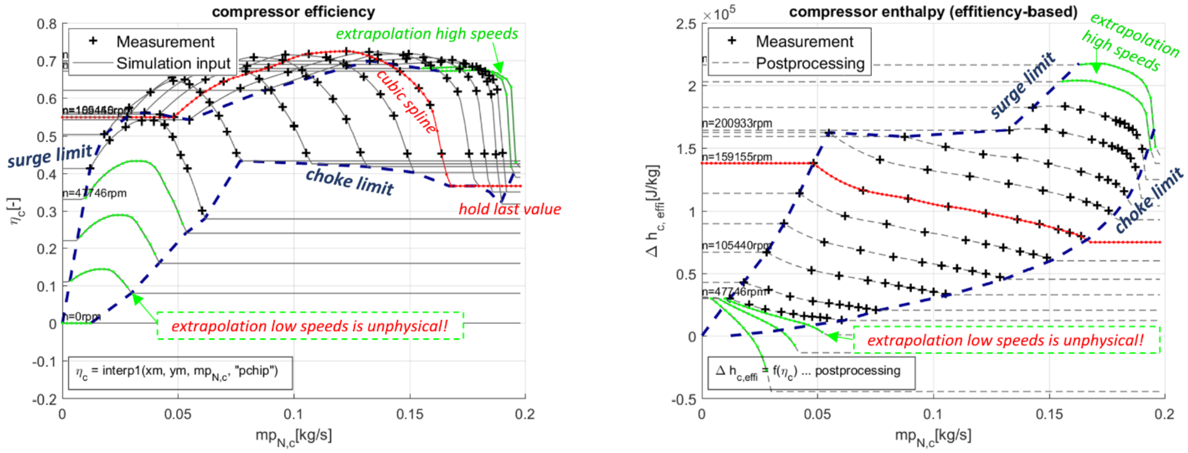

Fig. 50 Left: compressor efficiency map <u>not</u> used as simulation input, because extrapolation at low speeds would yield unphysical states (temperatures ca. -130°C) at compressor outlet in simulation model
Right: compressor enthalpy difference calculated from the efficiency resulting in <u>unphysical</u> values at extrapolated low speeds

Therefore, the enthalpy difference is being inter- and extrapolated as a compressor performance quantity instead of the enthalpy (see Fig. 50 Right).

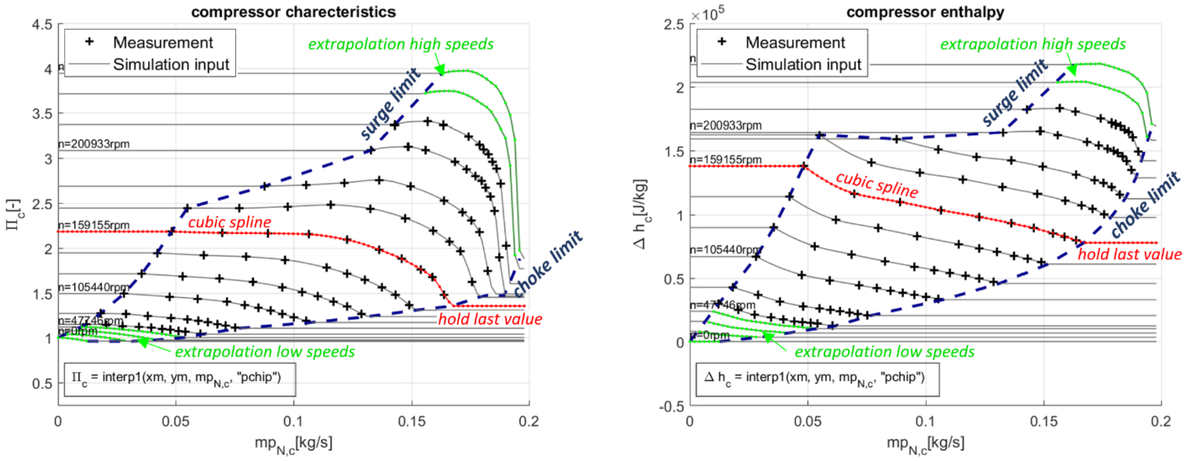

Fig. 51 Left: compressor pressure map used as simulation input, based on turbocharger measurements data fit, 2D detailed view
Right: compressor enthalpy difference used as simulation input, based on turbocharger measurements data fit, 2D detailed view

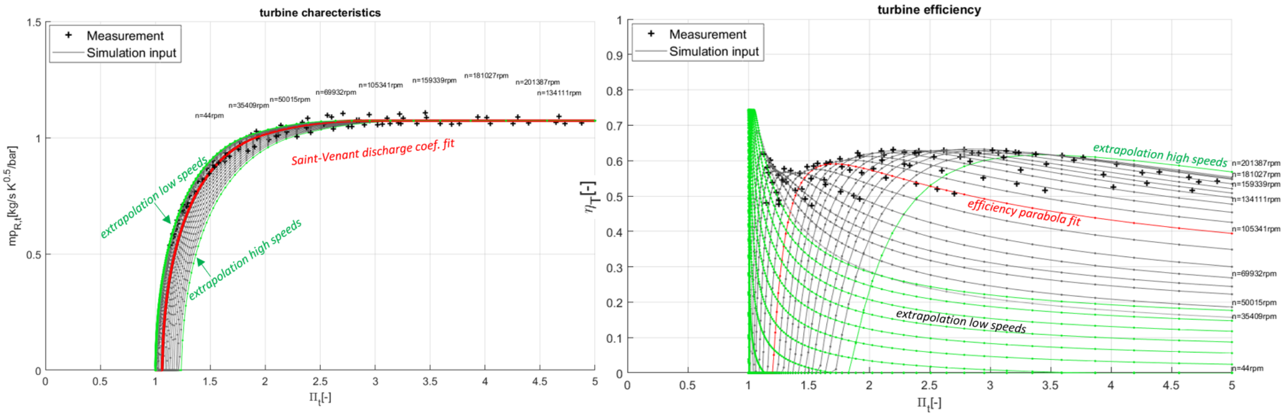

Fig. 52 Left: turbine mass flow characteristics used as simulation input, based on turbocharger measurement data fit, 2D detailed view
Right: turbine efficiency (product of turbine isentropic efficiency and turbocharger mechanical efficiency) used as simulation input, based on turbocharger measurement data fit, 2D detailed view

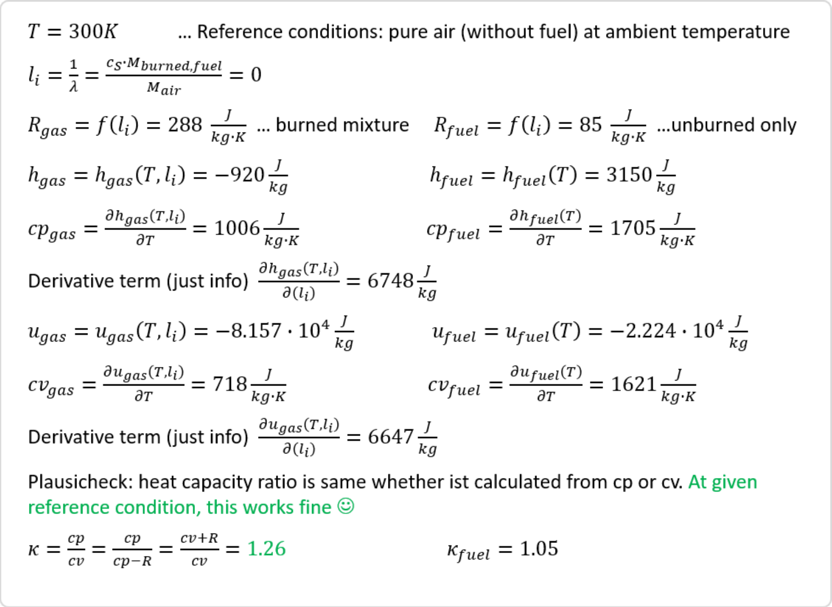

$T = 300K$ … Reference conditions: pure air (without fuel) at ambient temperature

$l_i = \frac{1}{\lambda} = \frac{c_S \cdot M_{burned,fuel}}{M_{air}} = 0$

$R_{gas} = f(l_i) = 288 \ \frac{J}{kg \cdot K}$ … burned mixture $R_{fuel} = f(l_i) = 85 \ \frac{J}{kg \cdot K}$ …unburned only

$h_{gas} = h_{gas}(T, l_i) = -920 \frac{J}{kg}$ $h_{fuel} = h_{fuel}(T) = 3150 \frac{J}{kg}$

$cp_{gas} = \frac{\partial h_{gas}(T,l_i)}{\partial T} = 1006 \frac{J}{kg \cdot K}$ $cp_{fuel} = \frac{\partial h_{fuel}(T)}{\partial T} = 1705 \frac{J}{kg \cdot K}$

Derivative term (just info) $\frac{\partial h_{gas}(T,l_i)}{\partial (l_i)} = 6748 \frac{J}{kg}$

$u_{gas} = u_{gas}(T, l_i) = -8.157 \cdot 10^4 \frac{J}{kg}$ $u_{fuel} = u_{fuel}(T) = -2.224 \cdot 10^4 \frac{J}{kg}$

$cv_{gas} = \frac{\partial u_{gas}(T,l_i)}{\partial T} = 718 \frac{J}{kg \cdot K}$ $cv_{fuel} = \frac{\partial u_{fuel}(T)}{\partial T} = 1621 \frac{J}{kg \cdot K}$

Derivative term (just info) $\frac{\partial u_{gas}(T,l_i)}{\partial (l_i)} = 6647 \frac{J}{kg}$

Plausicheck: heat capacity ratio is same whether ist calculated from cp or cv. At given reference condition, this works fine ☺

$\kappa = \frac{cp}{cv} = \frac{cp}{cp-R} = \frac{cv+R}{cv} = 1.26$ $\kappa_{fuel} = 1.05$

Fig. 53 Plausibility check: Gas mixture properties dependent on temperature and (unburned) air-fuel-ratio, obtained from data published by Grill 2006 [37], reference data of pure air at ambient conditions

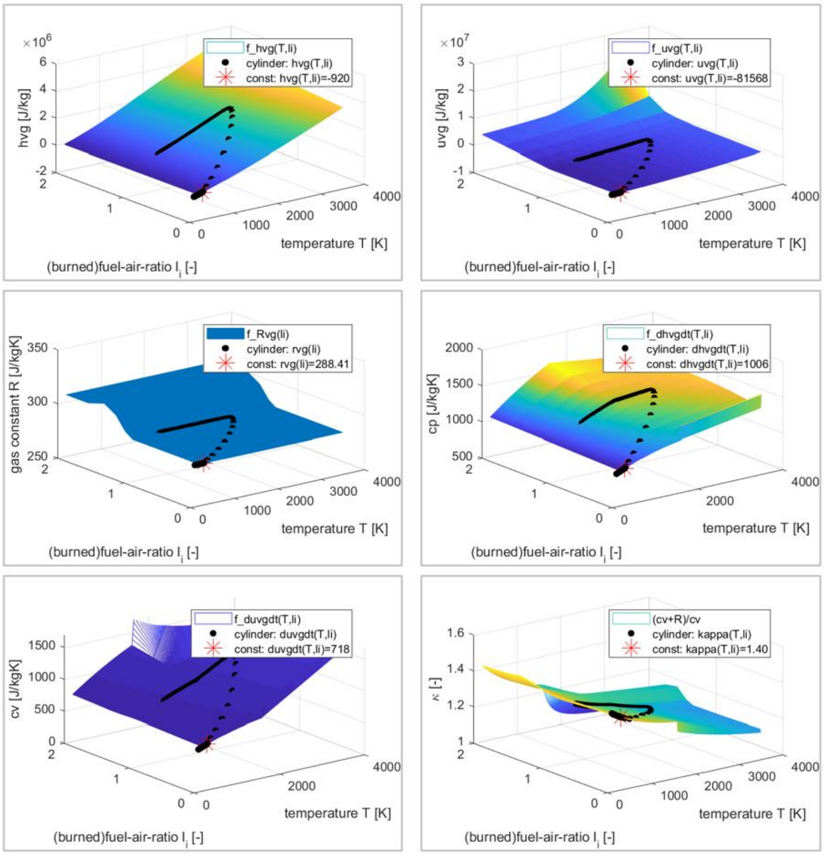

Fig. 54 Gas mixture properties dependent on temperature and (unburned) air-fuel-ratio, obtained from data published by Grill 2006 [37], Specific heat capacities c_p and c_v based on enthalpy, internal energy and their derivations, resulting heat capacity ratio κ

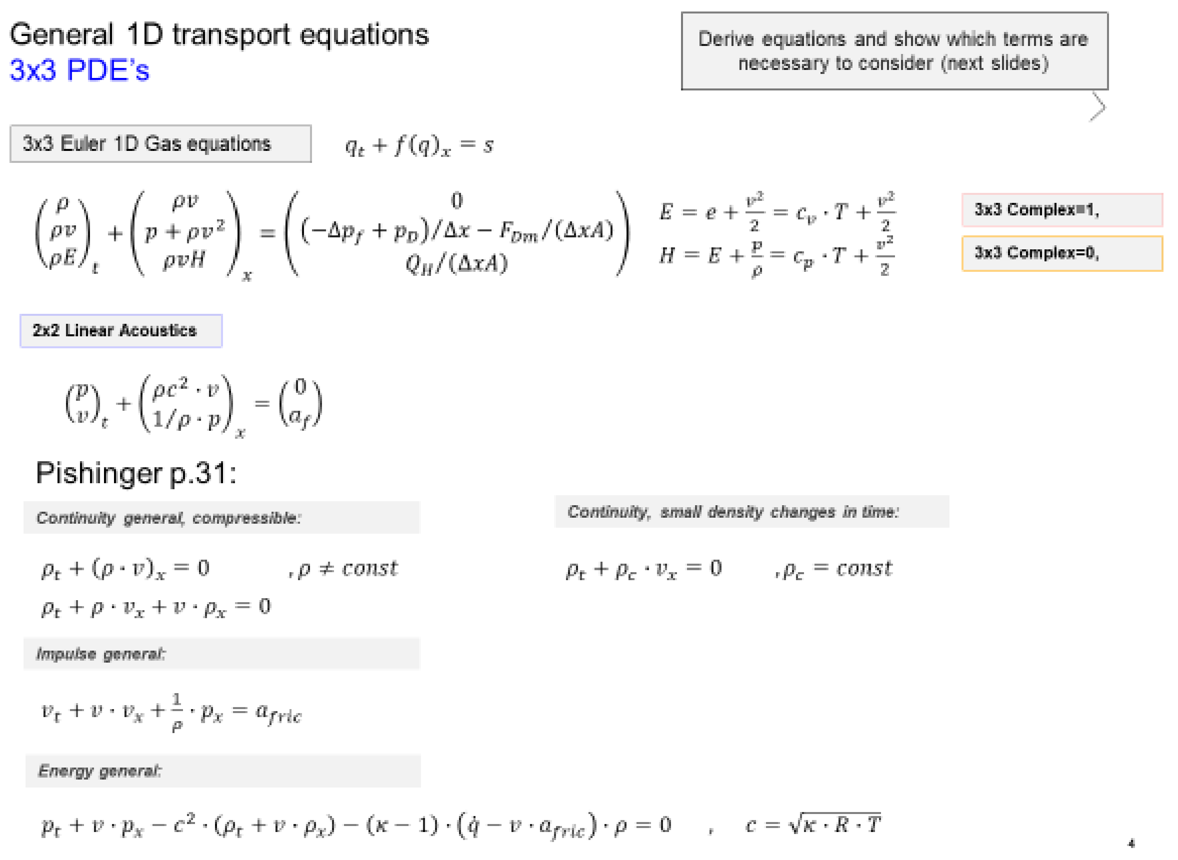

General 1D transport equations
3x3 PDE's

Derive equations and show which terms are necessary to consider (next slides)

3x3 Euler 1D Gas equations

$$q_t + f(q)_x = s$$

$$\begin{pmatrix} \rho \\ \rho v \\ \rho E \end{pmatrix}_t + \begin{pmatrix} \rho v \\ p + \rho v^2 \\ \rho v H \end{pmatrix}_x = \begin{pmatrix} 0 \\ (-\Delta p_f + p_D)/\Delta x - F_{Dm}/(\Delta x A) \\ Q_H/(\Delta x A) \end{pmatrix}$$

$$E = e + \frac{v^2}{2} = c_v \cdot T + \frac{v^2}{2}$$

$$H = E + \frac{p}{\rho} = c_p \cdot T + \frac{v^2}{2}$$

3x3 Complex=1,

3x3 Complex=0,

2x2 Linear Acoustics

$$\binom{p}{v}_t + \binom{\rho c^2 \cdot v}{1/\rho \cdot p}_x = \binom{0}{a_f}$$

Pishinger p.31:

Continuity general, compressible:

$$\rho_t + (\rho \cdot v)_x = 0 \qquad , \rho \neq const$$

$$\rho_t + \rho \cdot v_x + v \cdot \rho_x = 0$$

Impulse general:

$$v_t + v \cdot v_x + \frac{1}{\rho} \cdot p_x = a_{fric}$$

Energy general:

$$p_t + v \cdot p_x - c^2 \cdot (\rho_t + v \cdot \rho_x) - (\kappa - 1) \cdot (\dot{q} - v \cdot a_{fric}) \cdot \rho = 0 \quad , \quad c = \sqrt{\kappa \cdot R \cdot T}$$

Continuity, small density changes in time:

$$\rho_t + \rho_c \cdot v_x = 0 \qquad , \rho_c = const$$

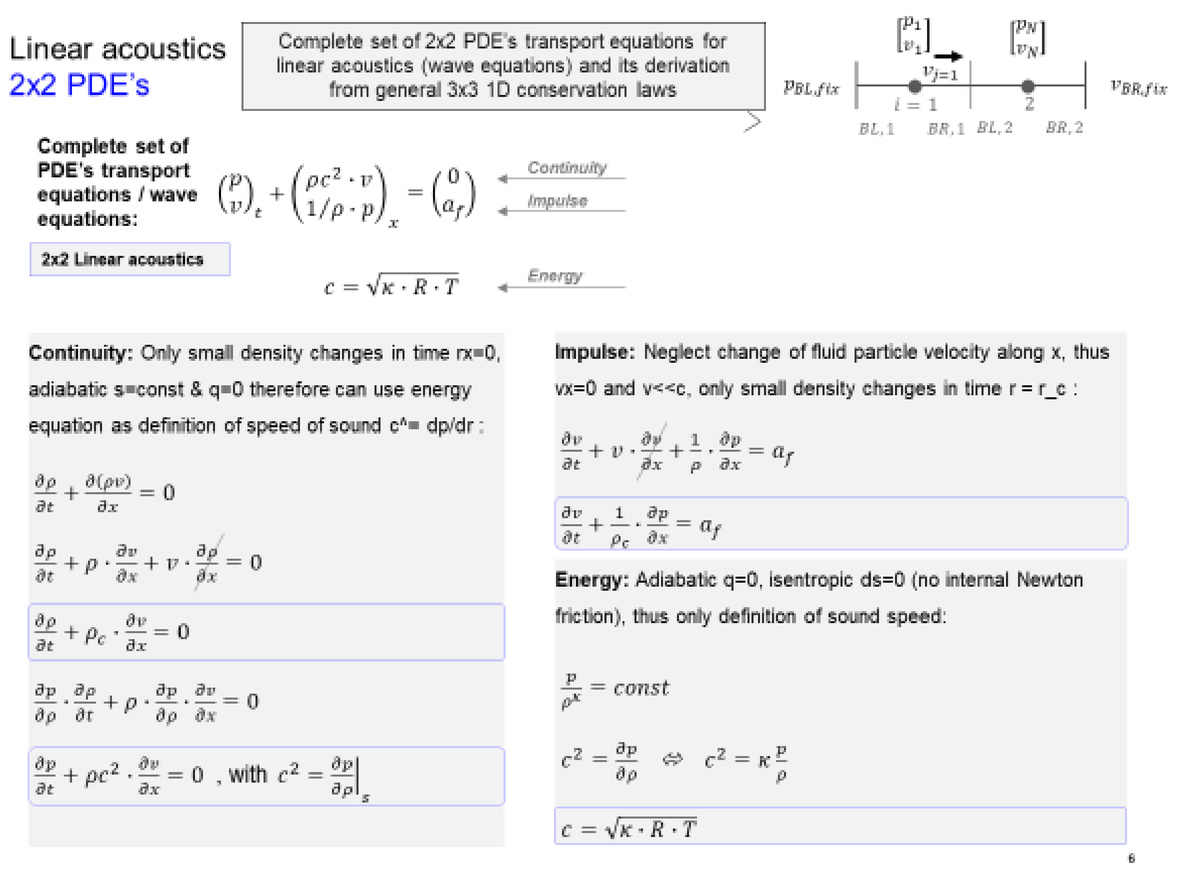

Linear acoustics
2x2 PDE's

Complete set of 2x2 PDE's transport equations for linear acoustics (wave equations) and its derivation from general 3x3 1D conservation laws

Complete set of PDE's transport equations / wave equations:

$$\binom{p}{v}_t + \binom{\rho c^2 \cdot v}{1/\rho \cdot p}_x = \binom{0}{a_f} \quad \leftarrow \text{Continuity} \quad \leftarrow \text{Impulse}$$

2x2 Linear acoustics

$$c = \sqrt{\kappa \cdot R \cdot T} \quad \leftarrow \text{Energy}$$

Continuity: Only small density changes in time rx=0, adiabatic s=const & q=0 therefore can use energy equation as definition of speed of sound c^= dp/dr :

$$\frac{\partial \rho}{\partial t} + \frac{\partial(\rho v)}{\partial x} = 0$$

$$\frac{\partial \rho}{\partial t} + \rho \cdot \frac{\partial v}{\partial x} + v \cdot \cancel{\frac{\partial \rho}{\partial x}} = 0$$

$$\boxed{\frac{\partial \rho}{\partial t} + \rho_c \cdot \frac{\partial v}{\partial x} = 0}$$

$$\frac{\partial p}{\partial \rho} \cdot \frac{\partial \rho}{\partial t} + \rho \cdot \frac{\partial p}{\partial \rho} \cdot \frac{\partial v}{\partial x} = 0$$

$$\boxed{\frac{\partial p}{\partial t} + \rho c^2 \cdot \frac{\partial v}{\partial x} = 0 \text{ , with } c^2 = \left.\frac{\partial p}{\partial \rho}\right|_s}$$

Impulse: Neglect change of fluid particle velocity along x, thus vx=0 and v<<c, only small density changes in time r = r_c :

$$\frac{\partial v}{\partial t} + v \cdot \cancel{\frac{\partial v}{\partial x}} + \frac{1}{\rho} \cdot \frac{\partial p}{\partial x} = a_f$$

$$\boxed{\frac{\partial v}{\partial t} + \frac{1}{\rho_c} \cdot \frac{\partial p}{\partial x} = a_f}$$

Energy: Adiabatic q=0, isentropic ds=0 (no internal Newton friction), thus only definition of sound speed:

$$\frac{p}{\rho^\kappa} = const$$

$$c^2 = \frac{\partial p}{\partial \rho} \quad \Leftrightarrow \quad c^2 = \kappa \frac{p}{\rho}$$

$$\boxed{c = \sqrt{\kappa \cdot R \cdot T}}$$

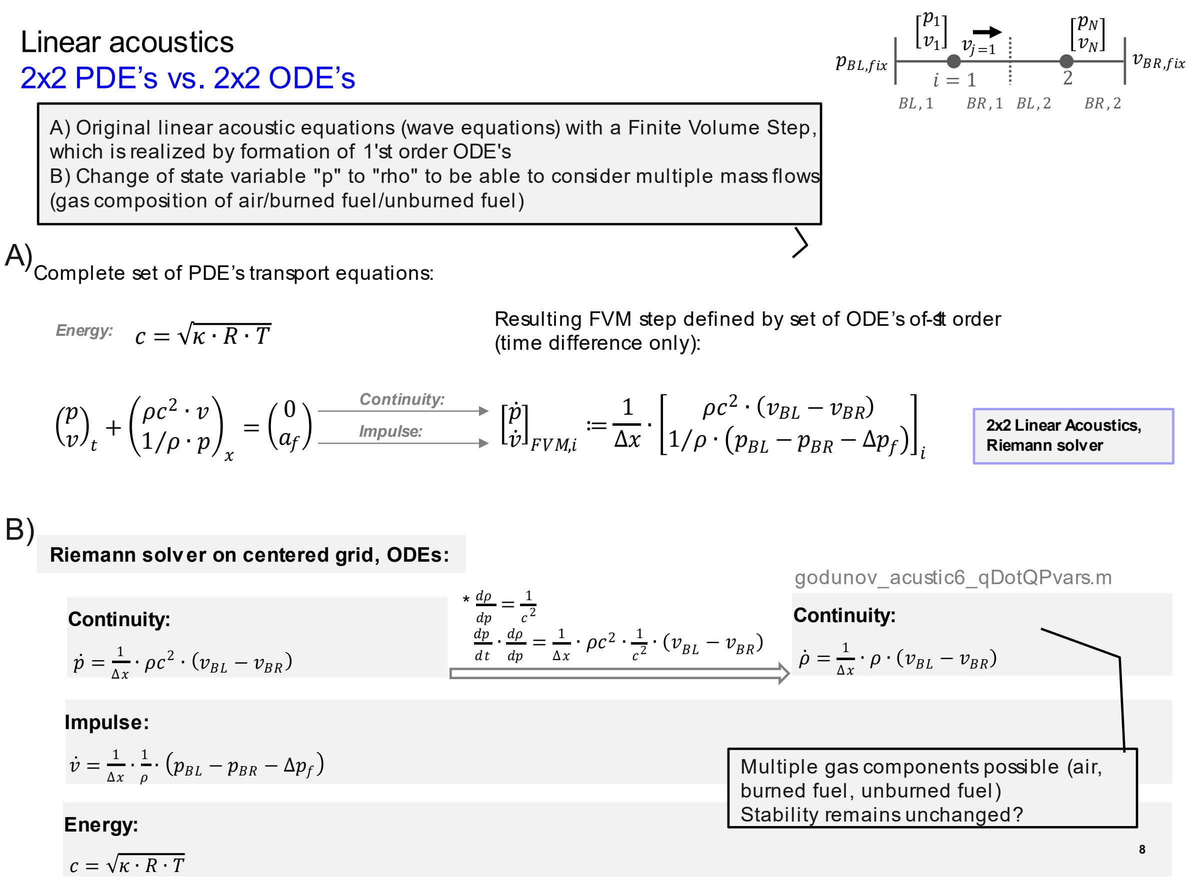

Linear acoustics
2x2 PDE's vs. 2x2 ODE's

A) Original linear acoustic equations (wave equations) with a Finite Volume Step, which is realized by formation of 1'st order ODE's
B) Change of state variable "p" to "rho" to be able to consider multiple mass flows (gas composition of air/burned fuel/unburned fuel)

A) Complete set of PDE's transport equations:

Energy: $c = \sqrt{\kappa \cdot R \cdot T}$

Resulting FVM step defined by set of ODE's of 1st order (time difference only):

$$\begin{pmatrix} p \\ v \end{pmatrix}_t + \begin{pmatrix} \rho c^2 \cdot v \\ 1/\rho \cdot p \end{pmatrix}_x = \begin{pmatrix} 0 \\ a_f \end{pmatrix} \xrightarrow[\text{Impulse:}]{\text{Continuity:}} \begin{bmatrix} \dot{p} \\ \dot{v} \end{bmatrix}_{FVM,i} := \frac{1}{\Delta x} \cdot \begin{bmatrix} \rho c^2 \cdot (v_{BL} - v_{BR}) \\ 1/\rho \cdot (p_{BL} - p_{BR} - \Delta p_f) \end{bmatrix}_i$$

2x2 Linear Acoustics, Riemann solver

B) **Riemann solver on centered grid, ODEs:**

godunov_acustic6_qDotQPvars.m

Continuity:

$\dot{p} = \frac{1}{\Delta x} \cdot \rho c^2 \cdot (v_{BL} - v_{BR})$

$$* \frac{d\rho}{dp} = \frac{1}{c^2}$$

$$\frac{dp}{dt} \cdot \frac{d\rho}{dp} = \frac{1}{\Delta x} \cdot \rho c^2 \cdot \frac{1}{c^2} \cdot (v_{BL} - v_{BR}) \Longrightarrow$$

Continuity:

$\dot{\rho} = \frac{1}{\Delta x} \cdot \rho \cdot (v_{BL} - v_{BR})$

Impulse:

$\dot{v} = \frac{1}{\Delta x} \cdot \frac{1}{\rho} \cdot (p_{BL} - p_{BR} - \Delta p_f)$

Multiple gas components possible (air, burned fuel, unburned fuel)
Stability remains unchanged?

Energy:

$c = \sqrt{\kappa \cdot R \cdot T}$

8

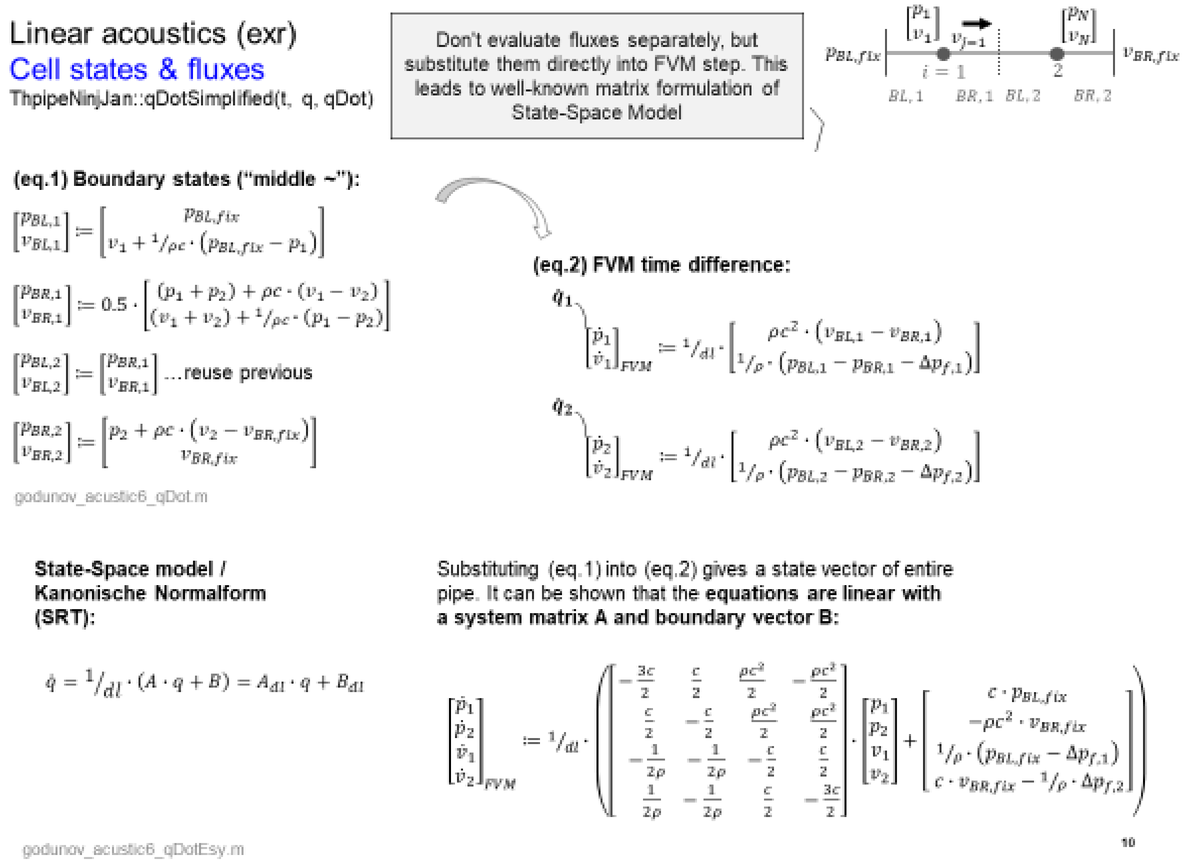

Linear acoustics (exr)
Cell states & fluxes

ThpipeNinjJan::qDotSimplified(t, q, qDot)

Don't evaluate fluxes separately, but substitute them directly into FVM step. This leads to well-known matrix formulation of State-Space Model

(eq.1) Boundary states ("middle ~"):

$$\begin{bmatrix} p_{BL,1} \\ v_{BL,1} \end{bmatrix} := \begin{bmatrix} p_{BL,fix} \\ v_1 + {}^1/_{\rho c} \cdot (p_{BL,fix} - p_1) \end{bmatrix}$$

$$\begin{bmatrix} p_{BR,1} \\ v_{BR,1} \end{bmatrix} := 0.5 \cdot \begin{bmatrix} (p_1 + p_2) + \rho c \cdot (v_1 - v_2) \\ (v_1 + v_2) + {}^1/_{\rho c} \cdot (p_1 - p_2) \end{bmatrix}$$

$$\begin{bmatrix} p_{BL,2} \\ v_{BL,2} \end{bmatrix} := \begin{bmatrix} p_{BR,1} \\ v_{BR,1} \end{bmatrix} \text{ ...reuse previous}$$

$$\begin{bmatrix} p_{BR,2} \\ v_{BR,2} \end{bmatrix} := \begin{bmatrix} p_2 + \rho c \cdot (v_2 - v_{BR,fix}) \\ v_{BR,fix} \end{bmatrix}$$

godunov_acustic6_qDot.m

(eq.2) FVM time difference:

$$\overbrace{\begin{bmatrix} \dot{p}_1 \\ \dot{v}_1 \end{bmatrix}_{FVM}}^{q_1} := {}^1/_{dl} \cdot \begin{bmatrix} \rho c^2 \cdot (v_{BL,1} - v_{BR,1}) \\ {}^1/_\rho \cdot (p_{BL,1} - p_{BR,1} - \Delta p_{f,1}) \end{bmatrix}$$

$$\overbrace{\begin{bmatrix} \dot{p}_2 \\ \dot{v}_2 \end{bmatrix}_{FVM}}^{q_2} := {}^1/_{dl} \cdot \begin{bmatrix} \rho c^2 \cdot (v_{BL,2} - v_{BR,2}) \\ {}^1/_\rho \cdot (p_{BL,2} - p_{BR,2} - \Delta p_{f,2}) \end{bmatrix}$$

State-Space model / Kanonische Normalform (SRT):

$$\dot{q} = {}^1/_{dl} \cdot (A \cdot q + B) = A_{dl} \cdot q + B_{dl}$$

Substituting (eq.1) into (eq.2) gives a state vector of entire pipe. It can be shown that the **equations are linear with a system matrix A and boundary vector B:**

$$\begin{bmatrix} \dot{p}_1 \\ \dot{p}_2 \\ \dot{v}_1 \\ \dot{v}_2 \end{bmatrix}_{FVM} := {}^1/_{dl} \cdot \left(\begin{bmatrix} -\frac{3c}{2} & \frac{c}{2} & \frac{\rho c^2}{2} & -\frac{\rho c^2}{2} \\ \frac{c}{2} & -\frac{c}{2} & \frac{\rho c^2}{2} & \frac{\rho c^2}{2} \\ -\frac{1}{2\rho} & -\frac{1}{2\rho} & -\frac{c}{2} & \frac{c}{2} \\ \frac{1}{2\rho} & -\frac{1}{2\rho} & \frac{c}{2} & -\frac{3c}{2} \end{bmatrix} \cdot \begin{bmatrix} p_1 \\ p_2 \\ v_1 \\ v_2 \end{bmatrix} + \begin{bmatrix} c \cdot p_{BL,fix} \\ -\rho c^2 \cdot v_{BR,fix} \\ {}^1/_\rho \cdot (p_{BL,fix} - \Delta p_{f,1}) \\ c \cdot v_{BR,fix} - {}^1/_\rho \cdot \Delta p_{f,2} \end{bmatrix} \right)$$

godunov_acustic6_qDotEsy.m

10

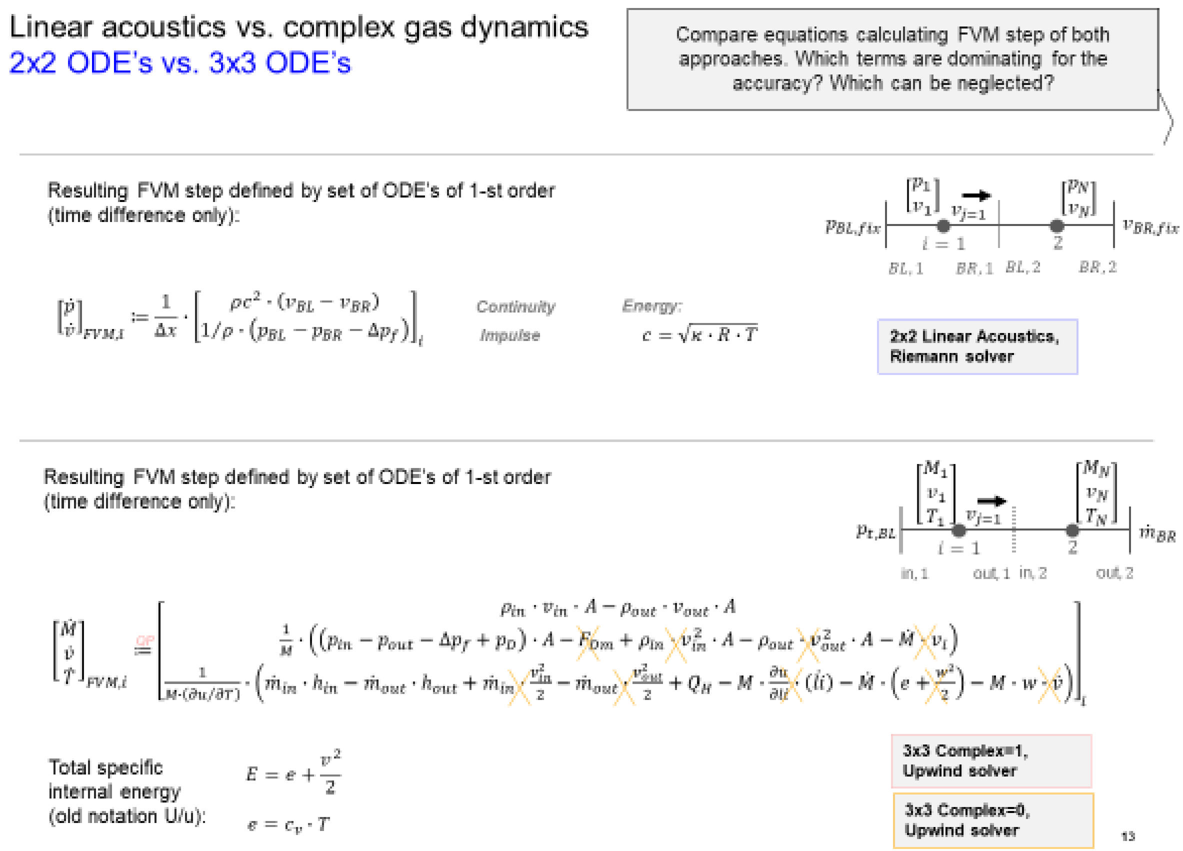

Linear acoustics vs. complex gas dynamics

2x2 ODE's vs. 3x3 ODE's

Compare equations calculating FVM step of both approaches. Which terms are dominating for the accuracy? Which can be neglected?

Resulting FVM step defined by set of ODE's of 1-st order (time difference only):

$$\begin{bmatrix}\dot{p}\\ \dot{v}\end{bmatrix}_{FVM,i} := \frac{1}{\Delta x}\cdot\begin{bmatrix}\rho c^2\cdot(v_{BL}-v_{BR})\\ 1/\rho\cdot(p_{BL}-p_{BR}-\Delta p_f)\end{bmatrix}_i$$

Continuity

Impulse

Energy:

$$c=\sqrt{\kappa\cdot R\cdot T}$$

2x2 Linear Acoustics, Riemann solver

Resulting FVM step defined by set of ODE's of 1-st order (time difference only):

$$\begin{bmatrix}\dot{M}\\ \dot{v}\\ \dot{T}\end{bmatrix}_{FVM,i} \overset{QP}{:=} \begin{bmatrix}\rho_{in}\cdot v_{in}\cdot A-\rho_{out}\cdot v_{out}\cdot A\\ \frac{1}{M}\cdot\left((p_{in}-p_{out}-\Delta p_f+p_D)\cdot A-\cancel{F_{Dm}}+\rho_{in}\cancel{\cdot v_{in}^2}\cdot A-\rho_{out}\cancel{\cdot v_{out}^2}\cdot A-\dot{M}\cancel{\cdot v_i}\right)\\ \frac{1}{M\cdot(\partial u/\partial T)}\cdot\left(\dot{m}_{in}\cdot h_{in}-\dot{m}_{out}\cdot h_{out}+\dot{m}_{in}\cancel{\cdot\frac{v_{in}^2}{2}}-\dot{m}_{out}\cancel{\cdot\frac{v_{out}^2}{2}}+Q_H-M\cdot\cancel{\frac{\partial u}{\partial ll}}\cdot(\dot{ll})-\dot{M}\cdot\left(e+\cancel{\frac{w^2}{2}}\right)-M\cdot w\cancel{\cdot\dot{v}}\right)\end{bmatrix}_i$$

Total specific internal energy (old notation U/u):

$$E=e+\frac{v^2}{2}$$

$$e=c_v\cdot T$$

3x3 Complex=1, Upwind solver

3x3 Complex=0, Upwind solver

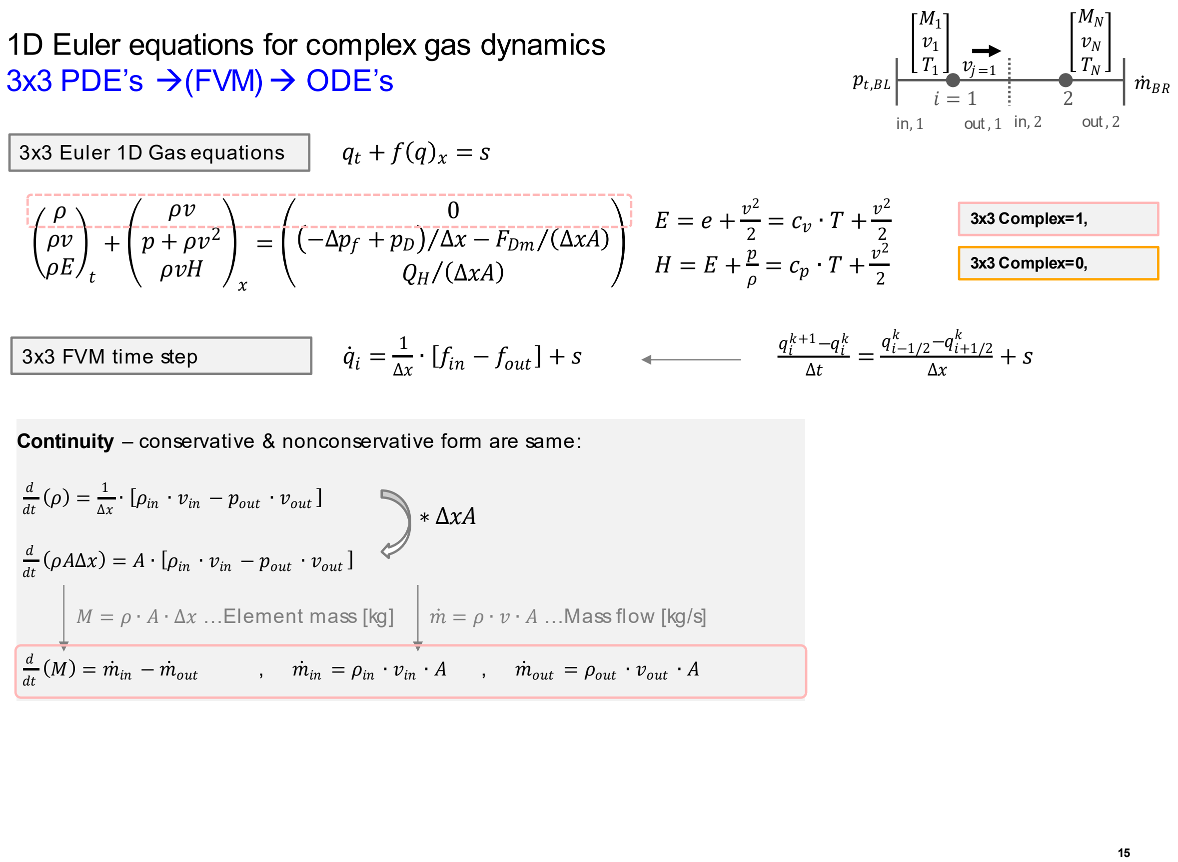

1D Euler equations for complex gas dynamics

3x3 PDE's →(FVM)→ ODE's

3x3 Euler 1D Gas equations

$$q_t+f(q)_x=s$$

$$\begin{pmatrix}\rho\\ \rho v\\ \rho E\end{pmatrix}_t+\begin{pmatrix}\rho v\\ p+\rho v^2\\ \rho vH\end{pmatrix}_x=\begin{pmatrix}0\\ (-\Delta p_f+p_D)/\Delta x-F_{Dm}/(\Delta xA)\\ Q_H/(\Delta xA)\end{pmatrix}$$

$$E=e+\frac{v^2}{2}=c_v\cdot T+\frac{v^2}{2}$$

$$H=E+\frac{p}{\rho}=c_p\cdot T+\frac{v^2}{2}$$

3x3 Complex=1,

3x3 Complex=0,

3x3 FVM time step

$$\dot{q}_i=\frac{1}{\Delta x}\cdot[f_{in}-f_{out}]+s \longleftarrow \frac{q_i^{k+1}-q_i^k}{\Delta t}=\frac{q_{i-1/2}^k-q_{i+1/2}^k}{\Delta x}+s$$

Continuity – conservative & nonconservative form are same:

$$\frac{d}{dt}(\rho)=\frac{1}{\Delta x}\cdot[\rho_{in}\cdot v_{in}-p_{out}\cdot v_{out}]$$

$$* \Delta xA$$

$$\frac{d}{dt}(\rho A\Delta x)=A\cdot[\rho_{in}\cdot v_{in}-p_{out}\cdot v_{out}]$$

$M=\rho\cdot A\cdot\Delta x$ …Element mass [kg]

$\dot{m}=\rho\cdot v\cdot A$ …Mass flow [kg/s]

$$\frac{d}{dt}(M)=\dot{m}_{in}-\dot{m}_{out}\quad,\quad \dot{m}_{in}=\rho_{in}\cdot v_{in}\cdot A\quad,\quad \dot{m}_{out}=\rho_{out}\cdot v_{out}\cdot A$$

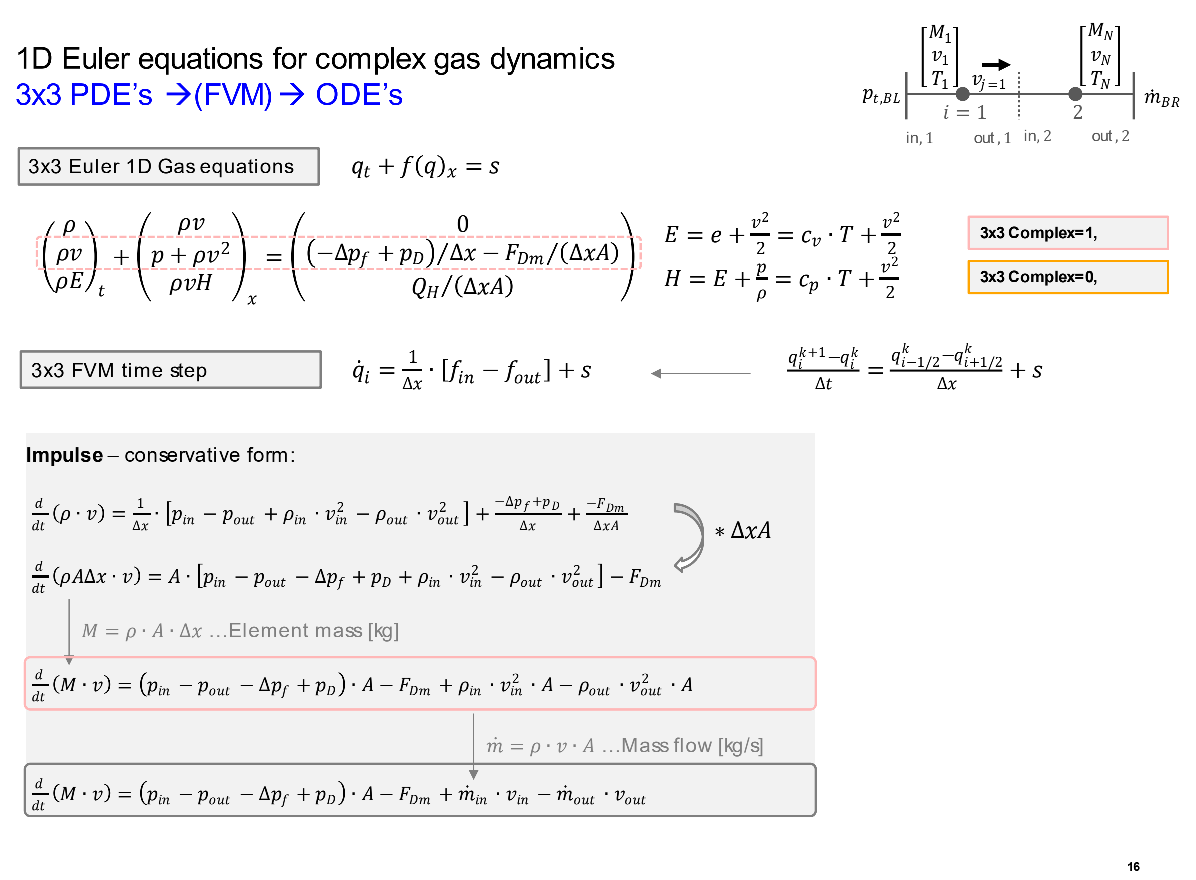

1D Euler equations for complex gas dynamics

3x3 PDE's →(FVM) → ODE's

3x3 Euler 1D Gas equations $q_t + f(q)_x = s$

$$\begin{pmatrix} \rho \\ \rho v \\ \rho E \end{pmatrix}_t + \begin{pmatrix} \rho v \\ p + \rho v^2 \\ \rho v H \end{pmatrix}_x = \begin{pmatrix} 0 \\ (-\Delta p_f + p_D)/\Delta x - F_{Dm}/(\Delta x A) \\ Q_H/(\Delta x A) \end{pmatrix}$$

$$E = e + \frac{v^2}{2} = c_v \cdot T + \frac{v^2}{2}$$

$$H = E + \frac{p}{\rho} = c_p \cdot T + \frac{v^2}{2}$$

3x3 Complex=1,

3x3 Complex=0,

3x3 FVM time step $\dot{q}_i = \frac{1}{\Delta x} \cdot [f_{in} - f_{out}] + s \longleftarrow \frac{q_i^{k+1} - q_i^k}{\Delta t} = \frac{q_{i-1/2}^k - q_{i+1/2}^k}{\Delta x} + s$

Impulse – conservative form:

$$\frac{d}{dt}(\rho \cdot v) = \frac{1}{\Delta x} \cdot \left[p_{in} - p_{out} + \rho_{in} \cdot v_{in}^2 - \rho_{out} \cdot v_{out}^2\right] + \frac{-\Delta p_f + p_D}{\Delta x} + \frac{-F_{Dm}}{\Delta x A}$$

$* \Delta x A$

$$\frac{d}{dt}(\rho A \Delta x \cdot v) = A \cdot \left[p_{in} - p_{out} - \Delta p_f + p_D + \rho_{in} \cdot v_{in}^2 - \rho_{out} \cdot v_{out}^2\right] - F_{Dm}$$

$M = \rho \cdot A \cdot \Delta x$ …Element mass [kg]

$$\frac{d}{dt}(M \cdot v) = (p_{in} - p_{out} - \Delta p_f + p_D) \cdot A - F_{Dm} + \rho_{in} \cdot v_{in}^2 \cdot A - \rho_{out} \cdot v_{out}^2 \cdot A$$

$\dot{m} = \rho \cdot v \cdot A$ …Mass flow [kg/s]

$$\frac{d}{dt}(M \cdot v) = (p_{in} - p_{out} - \Delta p_f + p_D) \cdot A - F_{Dm} + \dot{m}_{in} \cdot v_{in} - \dot{m}_{out} \cdot v_{out}$$

16

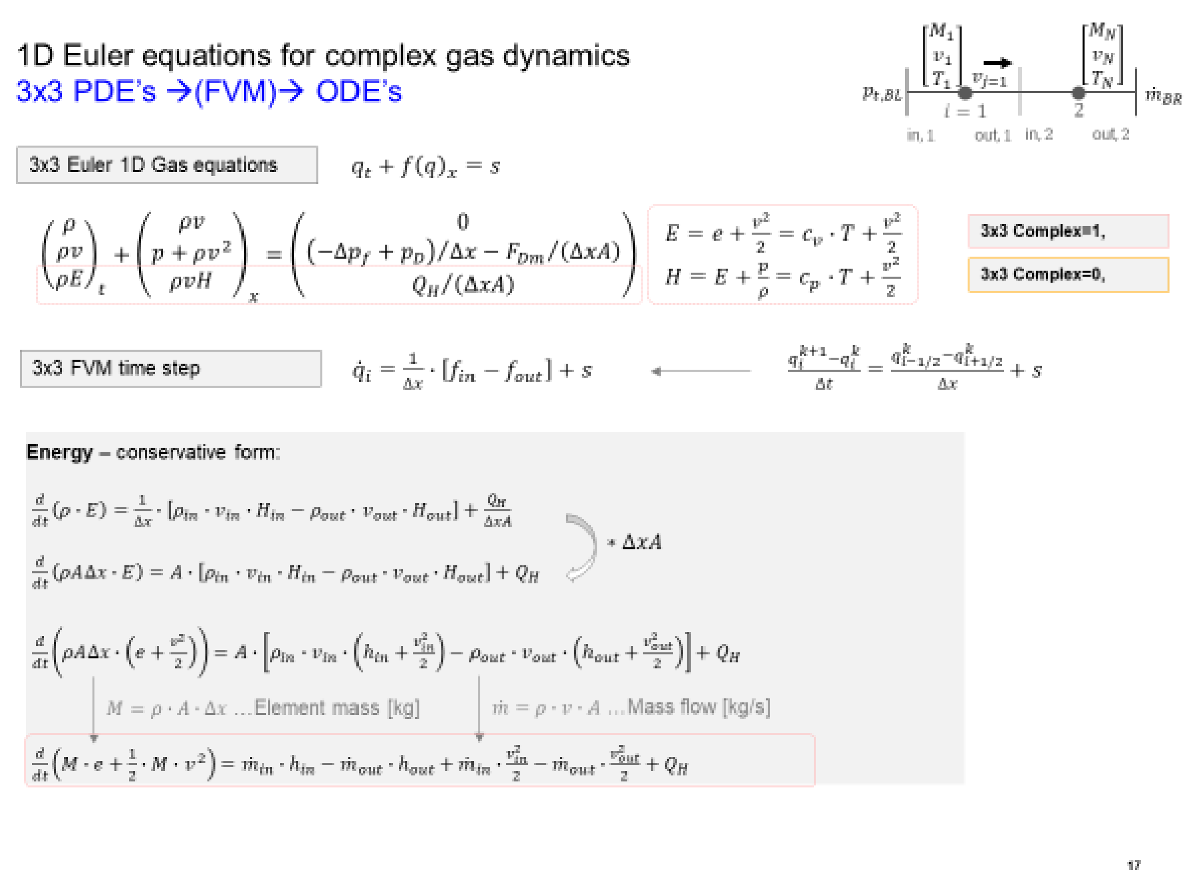

1D Euler equations for complex gas dynamics

3x3 PDE's →(FVM)→ ODE's

3x3 Euler 1D Gas equations $q_t + f(q)_x = s$

$$\begin{pmatrix} \rho \\ \rho v \\ \rho E \end{pmatrix}_t + \begin{pmatrix} \rho v \\ p + \rho v^2 \\ \rho v H \end{pmatrix}_x = \begin{pmatrix} 0 \\ (-\Delta p_f + p_D)/\Delta x - F_{Dm}/(\Delta x A) \\ Q_H/(\Delta x A) \end{pmatrix}$$

$$E = e + \frac{v^2}{2} = c_v \cdot T + \frac{v^2}{2}$$

$$H = E + \frac{p}{\rho} = c_p \cdot T + \frac{v^2}{2}$$

3x3 Complex=1,

3x3 Complex=0,

3x3 FVM time step $\dot{q}_i = \frac{1}{\Delta x} \cdot [f_{in} - f_{out}] + s \longleftarrow \frac{q_i^{k+1} - q_i^k}{\Delta t} = \frac{q_{i-1/2}^k - q_{i+1/2}^k}{\Delta x} + s$

Energy – conservative form:

$$\frac{d}{dt}(\rho \cdot E) = \frac{1}{\Delta x} \cdot \left[\rho_{in} \cdot v_{in} \cdot H_{in} - \rho_{out} \cdot v_{out} \cdot H_{out}\right] + \frac{Q_H}{\Delta x A}$$

$* \Delta x A$

$$\frac{d}{dt}(\rho A \Delta x \cdot E) = A \cdot \left[\rho_{in} \cdot v_{in} \cdot H_{in} - \rho_{out} \cdot v_{out} \cdot H_{out}\right] + Q_H$$

$$\frac{d}{dt}\left(\rho A \Delta x \cdot \left(e + \frac{v^2}{2}\right)\right) = A \cdot \left[\rho_{in} \cdot v_{in} \cdot \left(h_{in} + \frac{v_{in}^2}{2}\right) - \rho_{out} \cdot v_{out} \cdot \left(h_{out} + \frac{v_{out}^2}{2}\right)\right] + Q_H$$

$M = \rho \cdot A \cdot \Delta x$ …Element mass [kg] $\dot{m} = \rho \cdot v \cdot A$ …Mass flow [kg/s]

$$\frac{d}{dt}\left(M \cdot e + \frac{1}{2} \cdot M \cdot v^2\right) = \dot{m}_{in} \cdot h_{in} - \dot{m}_{out} \cdot h_{out} + \dot{m}_{in} \cdot \frac{v_{in}^2}{2} - \dot{m}_{out} \cdot \frac{v_{out}^2}{2} + Q_H$$

17

Complex 1D gas dynamics
3x3 ODE's, derivation of state changes

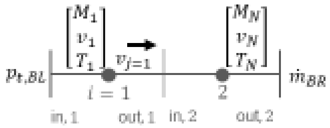

3x3 Complex=1, Upwind solver

3x3 Complex=0, Upwind solver

Upwind ½ space staggered grid in/out=UPS(v$_i$, r$_i$,r$_{i+1}$), ODEs:

Continuity – conservative form:

$$\frac{d}{dt}(M) = \dot{m}_{in} - \dot{m}_{out} \quad , \quad \dot{m}_{in} = \rho_{in}\cdot v_{in}\cdot A \quad , \quad \dot{m}_{out} = \rho_{out}\cdot v_{out}\cdot A$$

Impulse – conservative form:

$$\frac{d}{dt}(\overset{\times}{M}\cdot v) = \left(p_{in} - p_{out} - \Delta p_f + p_D\right)\cdot A - F_{\cancel{D}m} + \rho_{in}\cdot \cancel{v}_{in}^2\cdot A - \rho_{out}\cdot \cancel{v}_{out}^2\cdot A$$

Energy – conservative form:

$$\frac{d}{dt}\left(M\cdot e + \frac{1}{2}\cdot M \cancel{\cdot v^2}\right) = \dot{m}_{in}\cdot h_{in} - \dot{m}_{out}\cdot h_{out} + \dot{m}_{in}\cancel{\cdot}\frac{v_{in}^2}{2} - \dot{m}_{out}\cancel{\cdot}\frac{v_{out}^2}{2} + Q_H$$

Total specific internal energy (old notation U/u):

$$E = e + \frac{v^2}{2}$$

$$e = c_v\cdot T$$

Continuity – nonconservative form: $\rho_{in} = \rho_{ups(i-1,i)}$ $\quad v_{in} := v_i$ $\quad \rho_{out} := \rho_{ups(i,i+1)}$ $\quad v_{out} := v_{i+1}$

$$\dot{M} \overset{QP}{=} \rho_{in}\cdot v_{in}\cdot A - \rho_{out}\cdot v_{out}\cdot A \qquad \dot{\rho} = \frac{1}{\Delta x}\cdot\left(\rho_{in}\cdot v_{in} - \rho_{out}\cdot v_{out}\right)$$

Impulse – nonconservative form:

$$\dot{v} \overset{QP}{=} \frac{1}{M}\cdot\left(\left(p_{in} - p_{out} - \Delta p_f + p_D\right)\cdot A - F_{\cancel{D}m} + \rho_{in}\cdot \cancel{v}_{in}^2\cdot A - \rho_{out}\cdot \cancel{v}_{out}^2\cdot A - \dot{M}\cancel{\cdot v_i}\right)$$

Energy – nonconservative form:

$$\dot{T} \overset{QP}{=} \frac{1}{M\cdot(\partial e/\partial T)}\cdot\left(\dot{m}_{in}\cdot h_{in} - \dot{m}_{out}\cdot h_{out} + \dot{m}_{in}\cancel{\cdot}\frac{v_{in}^2}{2} - \dot{m}_{out}\cancel{\cdot}\frac{v_{out}^2}{2} + Q_H - M\cdot\frac{\partial e}{\partial u}\cancel{\cdot}(\dot{u}) - \dot{M}\cdot\left(e + \cancel{\frac{w^2}{2}}\right) - M\cdot w\cancel{\cdot}\dot{v}\right)$$

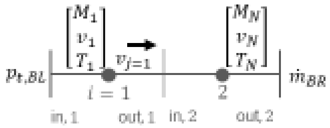

3x3 Complex=1, Upwind solver

3x3 Complex=0, Upwind solver

Continuity:

$$\frac{d}{dt}(M) = \dot{m}_{in} - \dot{m}_{out} \quad , \quad \dot{m}_{in} = \rho_{in}\cdot v_{in}\cdot A \quad , \quad \dot{m}_{out} = \rho_{out}\cdot v_{out}\cdot A$$

$$\dot{M} = \dot{m}_{in} - \dot{m}_{out}$$

$$\dot{M} = ups(v_i, \rho_{i-1}, \rho_i)\cdot v_i\cdot A - ups(v_{i+1}, \rho_i, \rho_{i+1})\cdot v_{i+1}\cdot A \qquad \rho_i = M_i\cdot\left({}^{1}/_{V_{el}}\right)$$

$$\dot{M} \overset{QP}{=} \rho_{ups(i-1,i)}\cdot v_i\cdot A - \rho_{ups(i,i+1)}\cdot v_{i+1}\cdot A$$

$$\updownarrow$$

$$\dot{M}_i = \dot{\rho}_i\cdot V_{el} \qquad / \quad V_{el} = A\cdot\Delta x$$

$$\dot{\rho} = \frac{1}{\Delta x}\cdot\left(\rho_{ups(i-1,i)}\cdot v_i - \rho_{ups(i,i+1)}\cdot v_{i+1}\right)$$

Variables see for e.g. in qDot_AirpipeN2.m

Impulse:

$$\frac{d}{dt}(\overset{\times}{M}\cdot v) = \left(p_{in} - p_{out} - \Delta p_f + p_D\right)\cdot A - F_{Dm} + \rho_{in}\cdot v_{in}^2\cdot A - \rho_{out}\cdot v_{out}^2\cdot A$$

$$\dot{v} \overset{QP}{=} \frac{1}{M}\cdot\left(\left(p_{in} - p_{out} - \Delta p_f + p_D\right)\cdot A - F_{\cancel{D}m} + \rho_{in}\cdot \cancel{v}_{in}^2\cdot A - \rho_{out}\cdot \cancel{v}_{out}^2\cdot A - \dot{M}\cancel{\cdot v_i}\right)$$

$$M = \rho\cdot V_{el} = \rho\cdot A\cdot\Delta x$$

$$\dot{M} = \dot{\rho}\cdot V_{el} = \dot{\rho}\cdot A\cdot\Delta x$$

$$\dot{v} = \frac{1}{\rho}\cdot\left(\left(p_{in} - p_{out} - \Delta p_f + p_D\right)\cdot\frac{1}{\Delta x} - F_{Dm} + \rho_{in}\cdot v_{in}^2\cdot\frac{1}{\Delta x} - \rho_{out}\cdot v_{out}^2\cdot\frac{1}{\Delta x} - \dot{\rho}\cdot v_i\right)$$

$$\dot{v} = \frac{1}{\rho}\cdot\left(\left(p_{in} - p_{out} - \Delta p_f + p_D + \rho_{in}\cdot v_{in}^2 - \rho_{out}\cdot v_{out}^2\right)\cdot\frac{1}{\Delta x} - F_{Dm} - \dot{\rho}\cdot v_i\right)$$

Variables see for e.g. in qDot_AirpipeN2.m

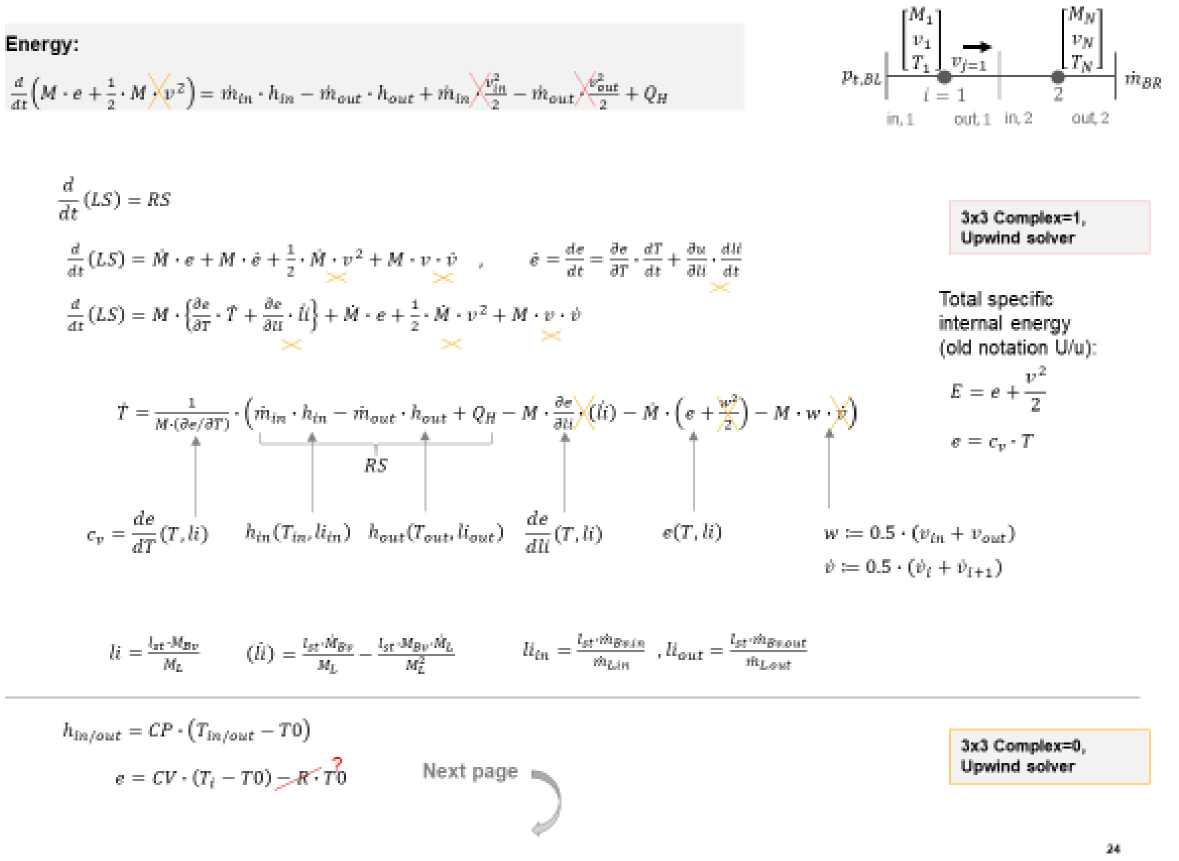

Energy:

$$\frac{d}{dt}\left(M\cdot e+\frac{1}{2}\cdot M\cdot\cancel{v^2}\right)=\dot m_{in}\cdot h_{in}-\dot m_{out}\cdot h_{out}+\dot m_{in}\cdot\cancel{\frac{v_{in}^2}{2}}-\dot m_{out}\cdot\cancel{\frac{v_{out}^2}{2}}+Q_H$$

$$\frac{d}{dt}(LS)=RS$$

$$\frac{d}{dt}(LS)=\dot M\cdot e+M\cdot\dot e+\frac{1}{2}\cdot\dot M\cdot\cancel{v^2}+M\cdot v\cdot\cancel{\dot v}\quad,\qquad \dot e=\frac{de}{dt}=\frac{\partial e}{\partial T}\cdot\frac{dT}{dt}+\frac{\partial u}{\partial li}\cdot\cancel{\frac{dli}{dt}}$$

$$\frac{d}{dt}(LS)=M\cdot\left\{\frac{\partial e}{\partial T}\cdot\dot T+\cancel{\frac{\partial e}{\partial li}}\cdot\dot{li}\right\}+\dot M\cdot e+\frac{1}{2}\cdot\cancel{\dot M}\cdot v^2+M\cdot\cancel{v}\cdot\dot v$$

3x3 Complex=1,
Upwind solver

Total specific internal energy (old notation U/u):

$$E=e+\frac{v^2}{2}$$

$$e=c_v\cdot T$$

$$\dot T=\frac{1}{M\cdot(\partial e/\partial T)}\cdot\left(\underbrace{\dot m_{in}\cdot h_{in}-\dot m_{out}\cdot h_{out}+Q_H}_{RS}-M\cdot\frac{\partial e}{\partial li}\cancel{\cdot}(\dot{li})-\dot M\cdot\left(e+\cancel{\frac{w^2}{2}}\right)-M\cdot w\cdot\cancel{\dot v}\right)$$

$$c_v=\frac{de}{dT}(T,li)\qquad h_{in}(T_{in},li_{in})\qquad h_{out}(T_{out},li_{out})\qquad \frac{de}{dli}(T,li)\qquad e(T,li)$$

$$w\coloneqq 0.5\cdot(v_{in}+v_{out})$$
$$\dot v\coloneqq 0.5\cdot(\dot v_i+\dot v_{i+1})$$

$$li=\frac{l_{st}\cdot M_{Bv}}{M_L}\qquad (\dot{li})=\frac{l_{st}\cdot\dot M_{Bv}}{M_L}-\frac{l_{st}\cdot M_{Bv}\cdot\dot M_L}{M_L^2}\qquad li_{in}=\frac{l_{st}\cdot\dot m_{Bv,in}}{\dot m_{L,in}}\ ,li_{out}=\frac{l_{st}\cdot\dot m_{Bv,out}}{\dot m_{L,out}}$$

$$h_{in/out}=CP\cdot\left(T_{in/out}-T0\right)$$

$$e=CV\cdot(T_i-T0)\cancel{-R\cdot T0}^{\,?}$$

Next page

3x3 Complex=0,
Upwind solver

24

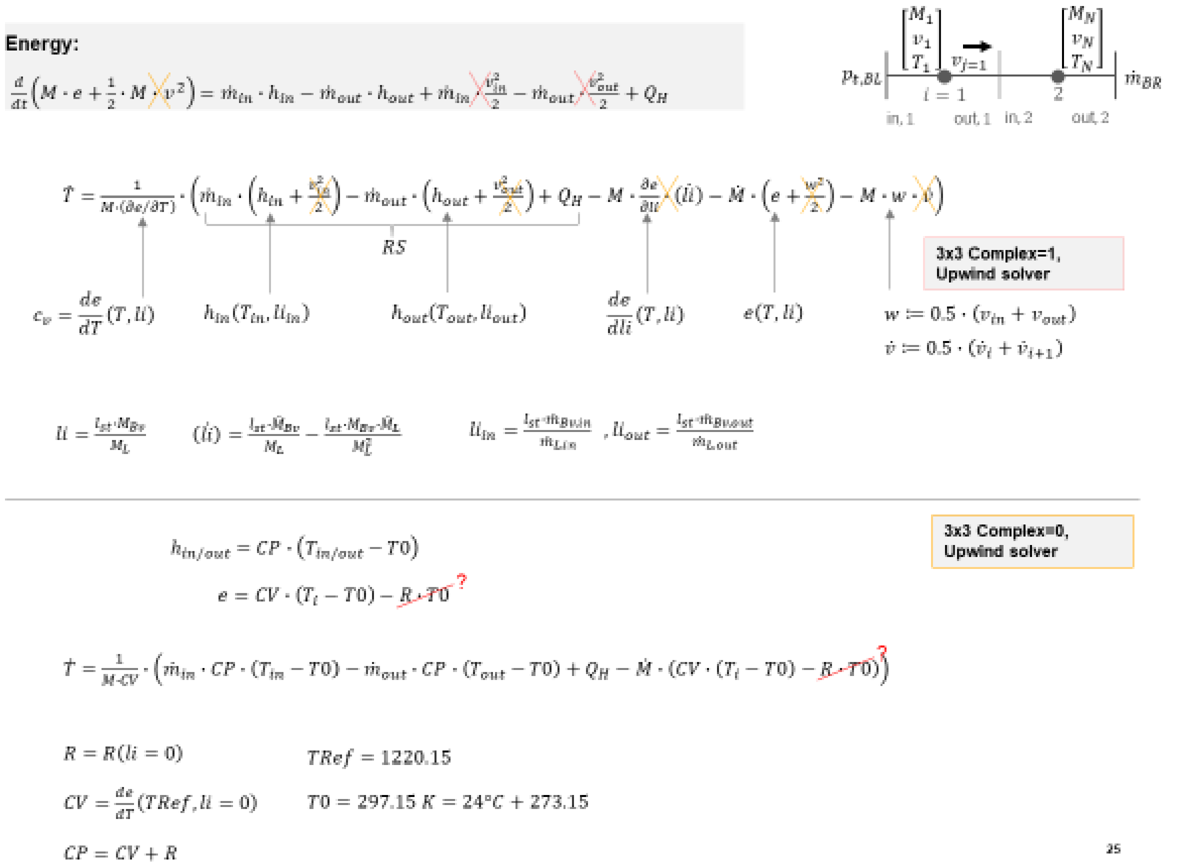

Energy:

$$\frac{d}{dt}\left(M\cdot e+\frac{1}{2}\cdot M\cdot\cancel{v^2}\right)=\dot m_{in}\cdot h_{in}-\dot m_{out}\cdot h_{out}+\dot m_{in}\cdot\cancel{\frac{v_{in}^2}{2}}-\dot m_{out}\cdot\cancel{\frac{v_{out}^2}{2}}+Q_H$$

$$\dot T=\frac{1}{M\cdot(\partial e/\partial T)}\cdot\left(\underbrace{\dot m_{in}\cdot\left(h_{in}+\cancel{\frac{v_{in}^2}{2}}\right)-\dot m_{out}\cdot\left(h_{out}+\cancel{\frac{v_{out}^2}{2}}\right)+Q_H}_{RS}-M\cdot\frac{\partial e}{\partial li}\cancel{\cdot}(\dot{li})-\dot M\cdot\left(e+\cancel{\frac{w^2}{2}}\right)-M\cdot w\cdot\cancel{\dot v}\right)$$

3x3 Complex=1,
Upwind solver

$$c_v=\frac{de}{dT}(T,li)\qquad h_{in}(T_{in},li_{in})\qquad h_{out}(T_{out},li_{out})\qquad \frac{de}{dli}(T,li)\qquad e(T,li)$$

$$w\coloneqq 0.5\cdot(v_{in}+v_{out})$$
$$\dot v\coloneqq 0.5\cdot(\dot v_i+\dot v_{i+1})$$

$$li=\frac{l_{st}\cdot M_{Bv}}{M_L}\qquad (\dot{li})=\frac{l_{st}\cdot\dot M_{Bv}}{M_L}-\frac{l_{st}\cdot M_{Bv}\cdot\dot M_L}{M_L^2}\qquad li_{in}=\frac{l_{st}\cdot\dot m_{Bv,in}}{\dot m_{L,in}}\ ,li_{out}=\frac{l_{st}\cdot\dot m_{Bv,out}}{\dot m_{L,out}}$$

3x3 Complex=0,
Upwind solver

$$h_{in/out}=CP\cdot\left(T_{in/out}-T0\right)$$

$$e=CV\cdot(T_i-T0)-\cancel{R\cdot T0}^{\,?}$$

$$\dot T=\frac{1}{M\cdot CV}\cdot\left(\dot m_{in}\cdot CP\cdot(T_{in}-T0)-\dot m_{out}\cdot CP\cdot(T_{out}-T0)+Q_H-\dot M\cdot(CV\cdot(T_i-T0)-\cancel{R\cdot T0})^{?}\right)$$

$$R=R(li=0)\qquad TRef=1220.15$$

$$CV=\frac{de}{dT}(TRef,li=0)\qquad T0=297.15\ K=24°C+273.15$$

$$CP=CV+R$$

25

2 Appendix – Stationary Database

Following section shows engine characteristic 2-dimensional maps obtained from steady-state measurements in dependence on engine speed (nE) and break specific mean effective pressure (BMEP).

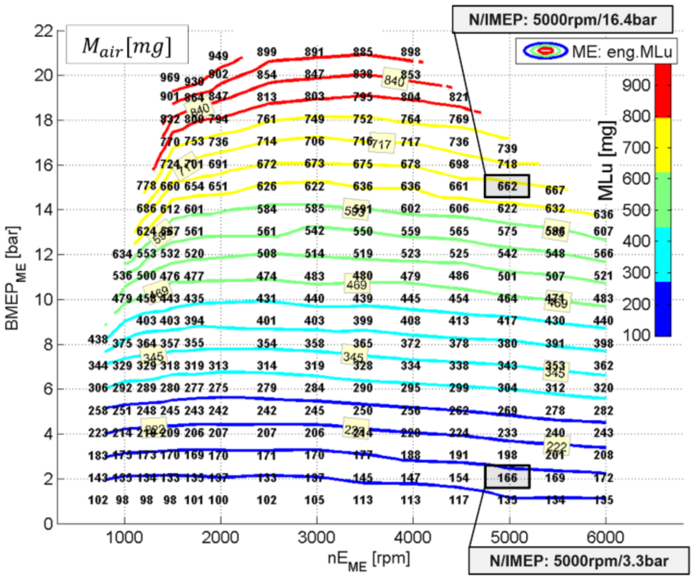

Fig. 55 Calculated trapped in-cylinder air-mass ($M_{Air,unburned} = M_{inj} * c_S * lambda_{brett}$, $c_S = 14.2$) obtained from steady-state experiment

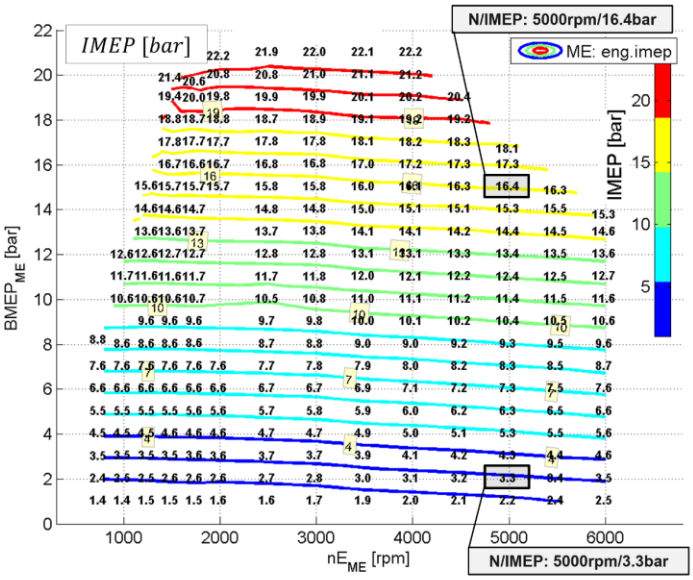

Fig. 56 Cylinder indicated mean effective pressure obtained from steady-state experiment

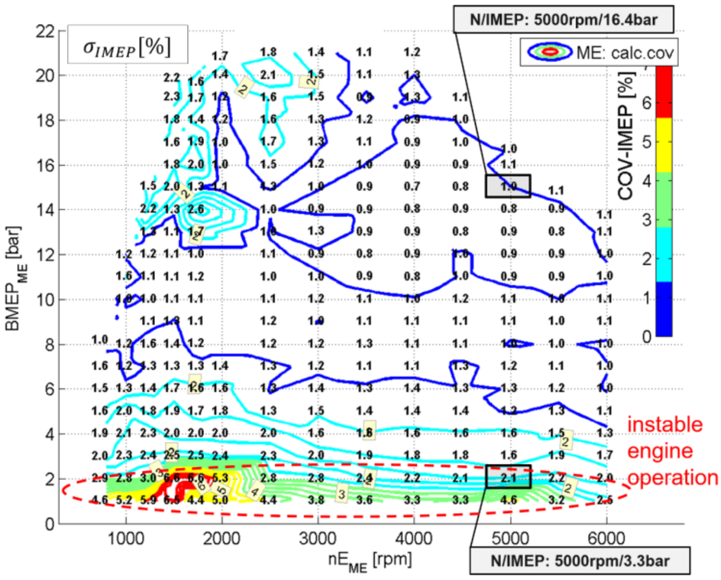

Fig. 57 Standard deviation of indicated mean effective pressure (covariance-IMEP) as a mass for stability of steady-state engine operating conditions (based on 100 engine cycles)

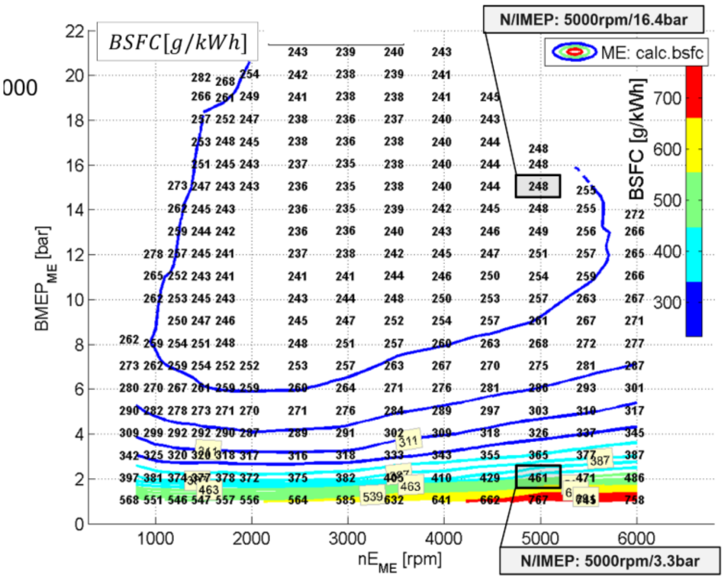

Fig. 58 Break specific fuel consumption (BSFC = mp$_{inj}$ / P$_{eng}$ * 1000) obtained from steady-state experiment

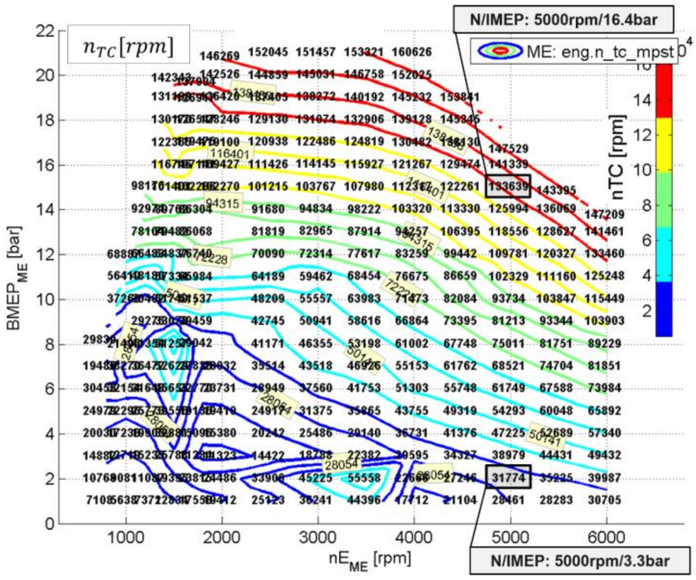

Fig. 59 Turbocharger shaft speed obtained from steady-state experiment

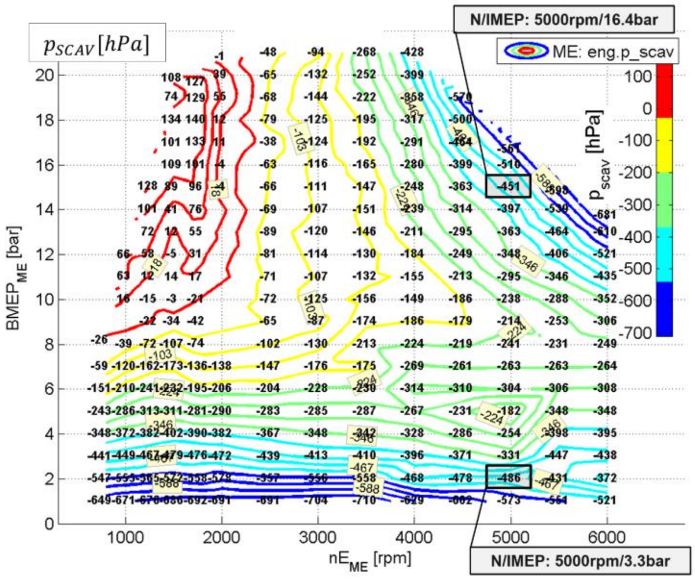

Fig. 60 Calculated scavenging pressure difference ($p_{SCAV} = p_{22} – p_3$) obtained from steady-state experiment

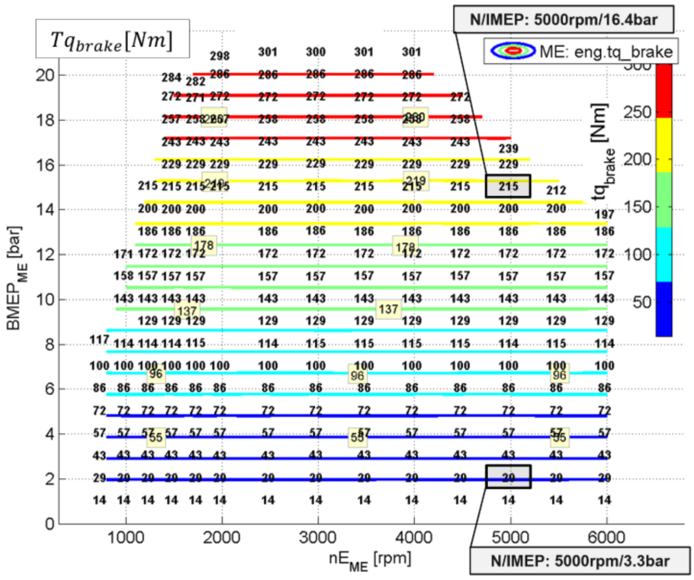

Fig. 61 Engine break torque obtained from steady-state experiment

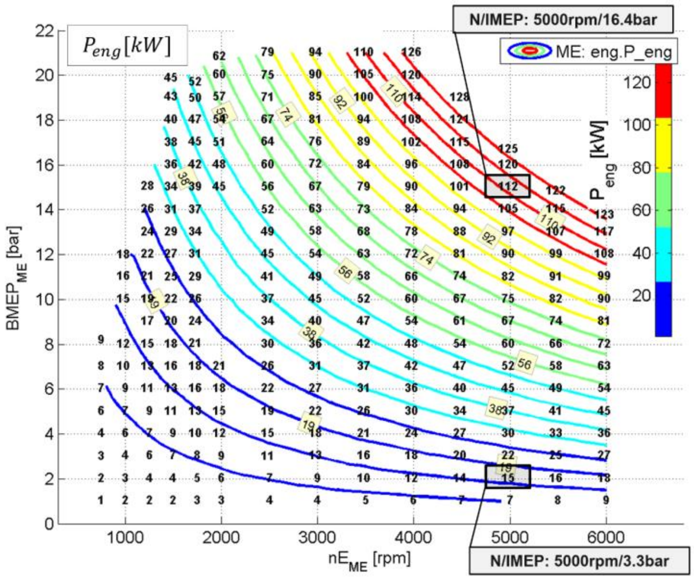

Fig. 62 Engine brake power obtained from steady-state experiment

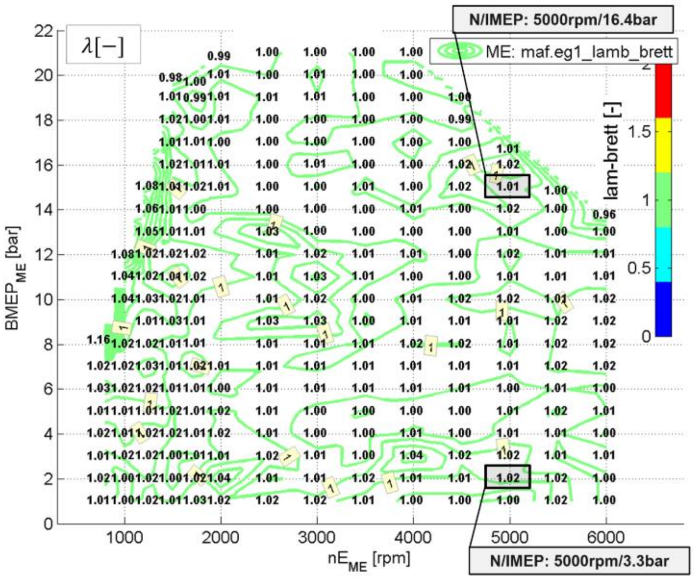

Fig. 63 Calculated exhaust air-fuel equivalence ratio (calculated by Brettschneider formula based on exhaust emissions) obtained from steady-state experiment

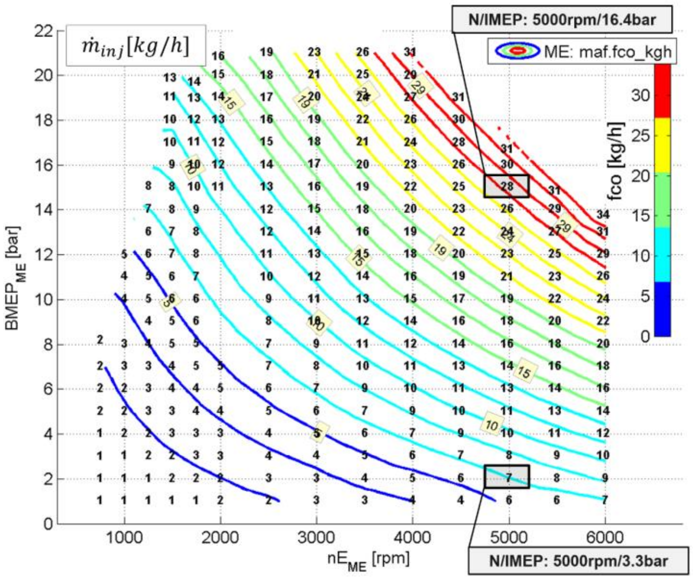

Fig. 64 Injected mass flow rate (= fuel consumption) obtained from steady-state experiment

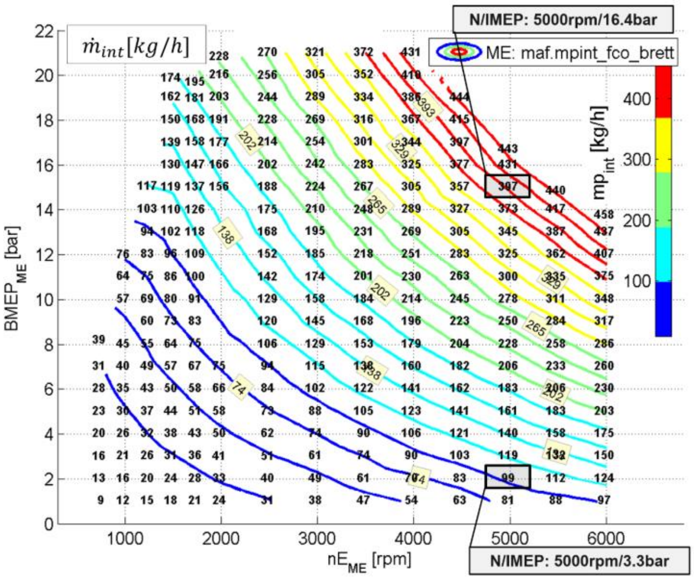

Fig. 65 Calculated intake mass flow rate obtained from steady-state experiment

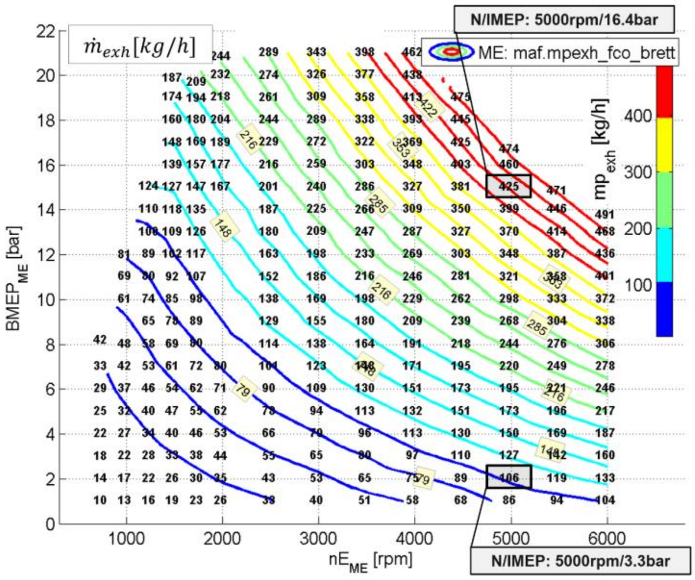

Fig. 66 Calculated exhaust mass flow rate obtained from steady-state experiment

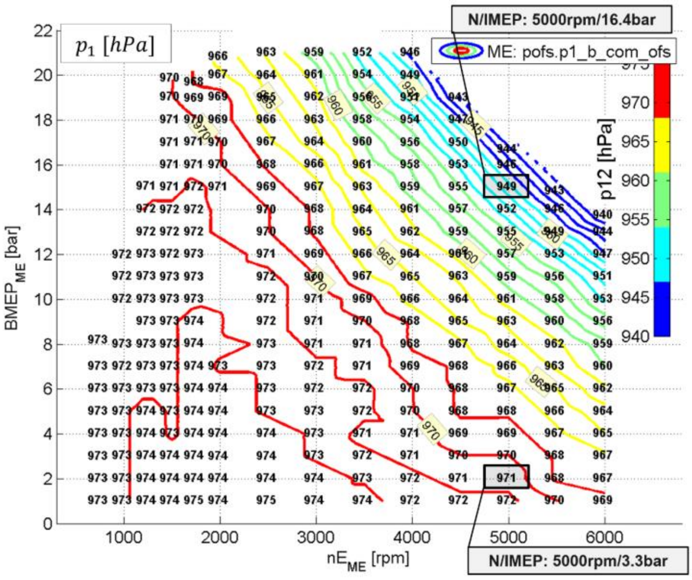

Fig. 67 Pressure before compressor obtained from steady-state experiment

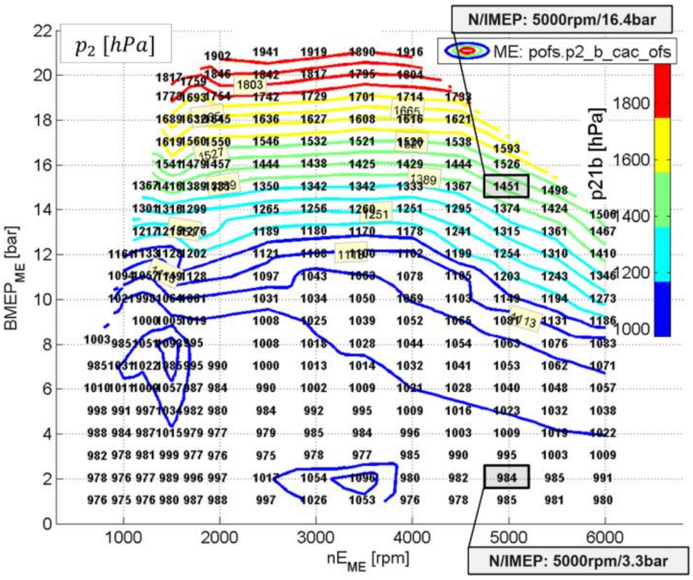

Fig. 68 Pressure after compressor (= pressure before charge air cooler) obtained from steady-state experiment

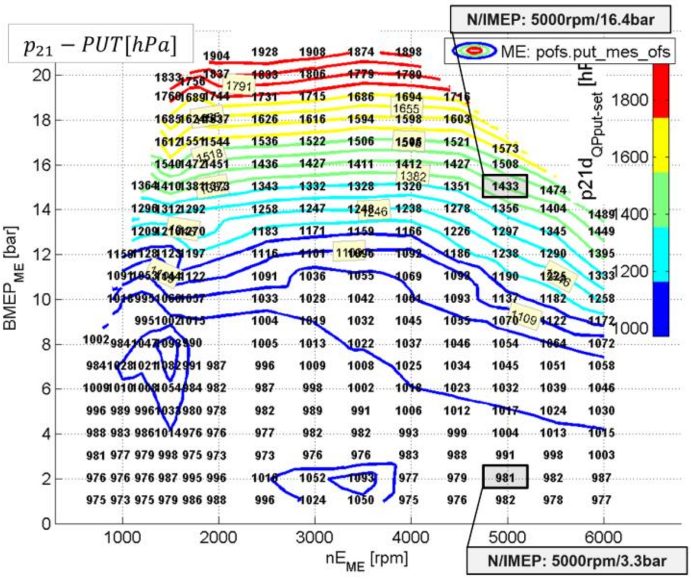

Fig. 69 Pressure after charge air cooler (= pressure upstream throttle) obtained from steady-state experiment

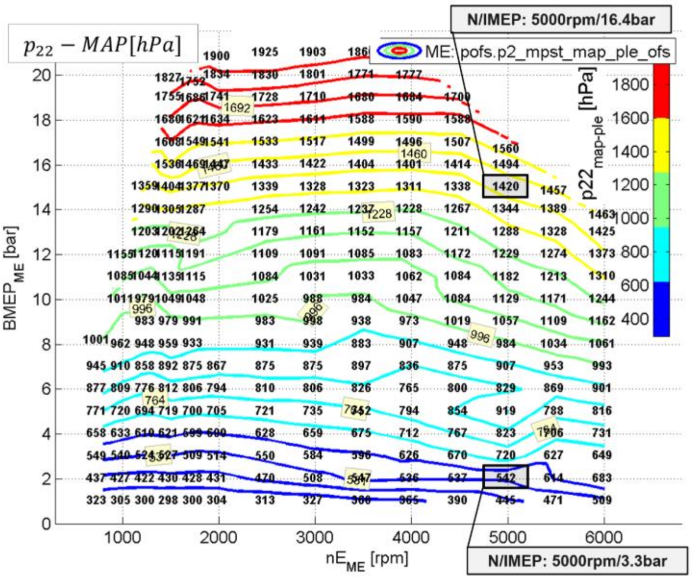

Fig. 70 Time averaged intake manifold pressure (engine setpoint pressure) obtained from steady-state experiment

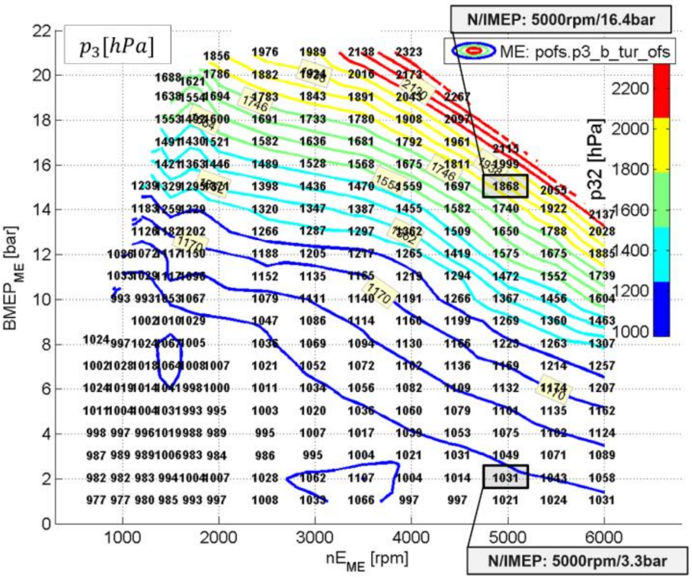

Fig. 71 Pressure before turbine (= pressure in exhaust manifold) obtained from steady-state experiment

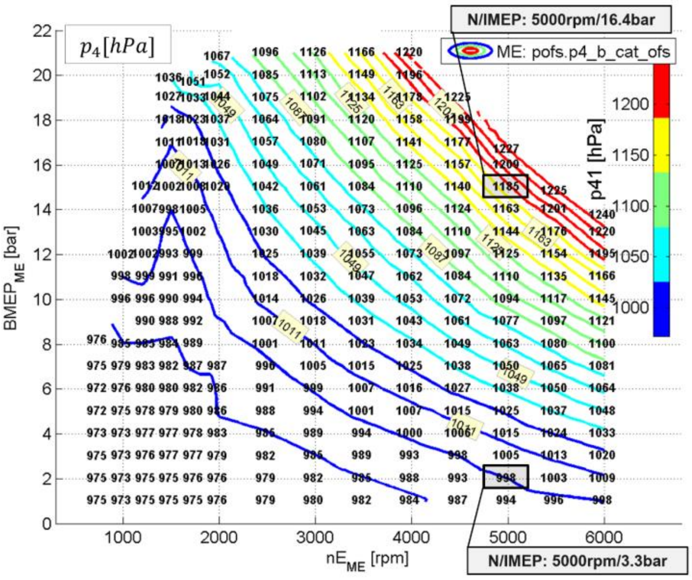

Fig. 72 Pressure after turbine (= pressure before 3-way catalyst) obtained from steady-state experiment

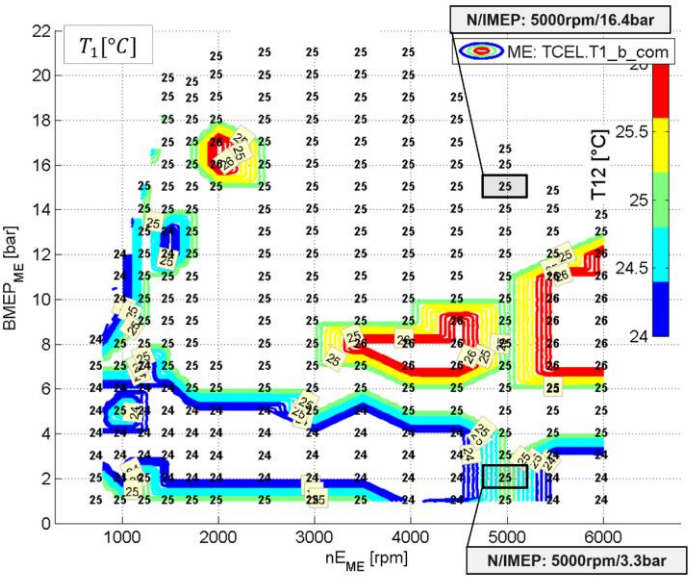

Fig. 73 Temperature before compressor obtained from steady-state experiment

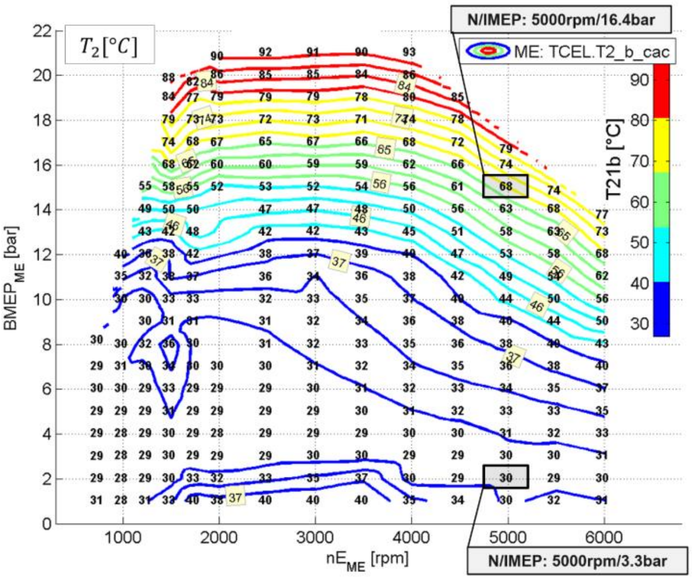

Fig. 74 Temperature after compressor obtained from steady-state experiment

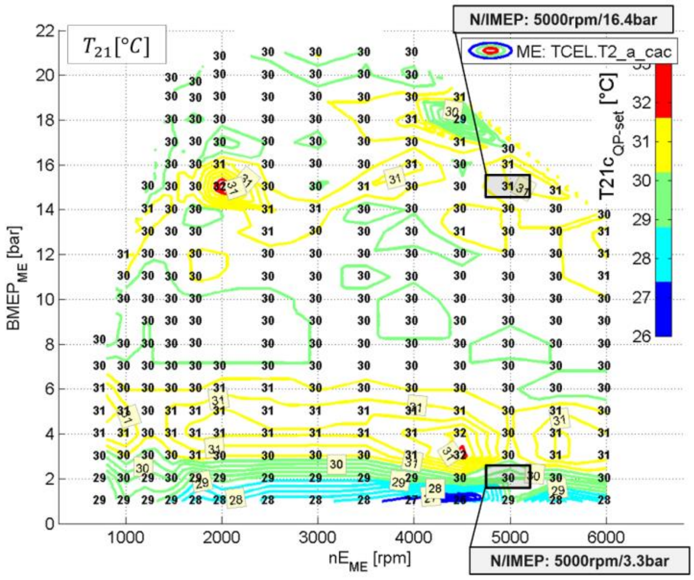

Fig. 75 Temperature after charge air cooler (engine setpoint temperature = ca. 30°C) obtained from steady-state experiment

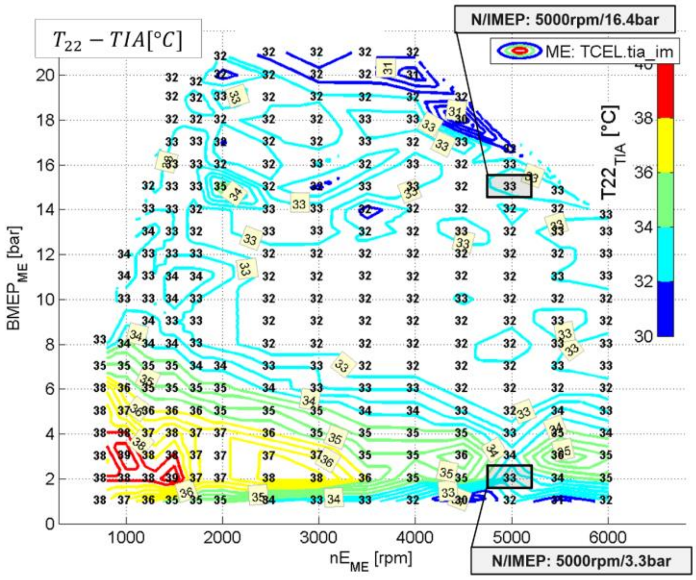

Fig. 76 Intake manifold temperature (ECU sensor) obtained from steady-state experiment

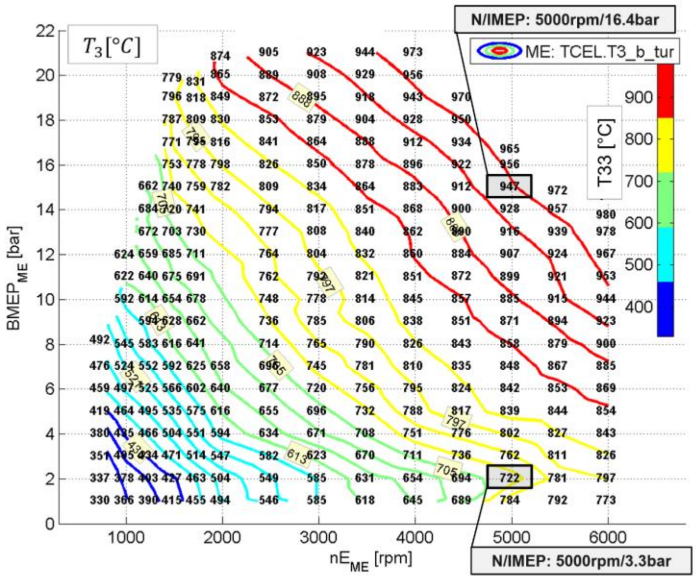

Fig. 77 Temperature before turbine obtained from steady-state experiment

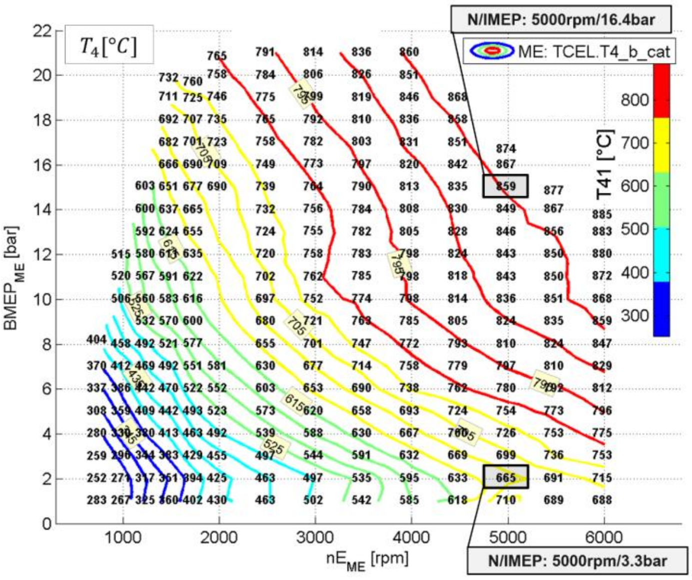

Fig. 78 Temperature after turbine obtained from steady-state experiment

3 Appendix – Model Accuracy of M1

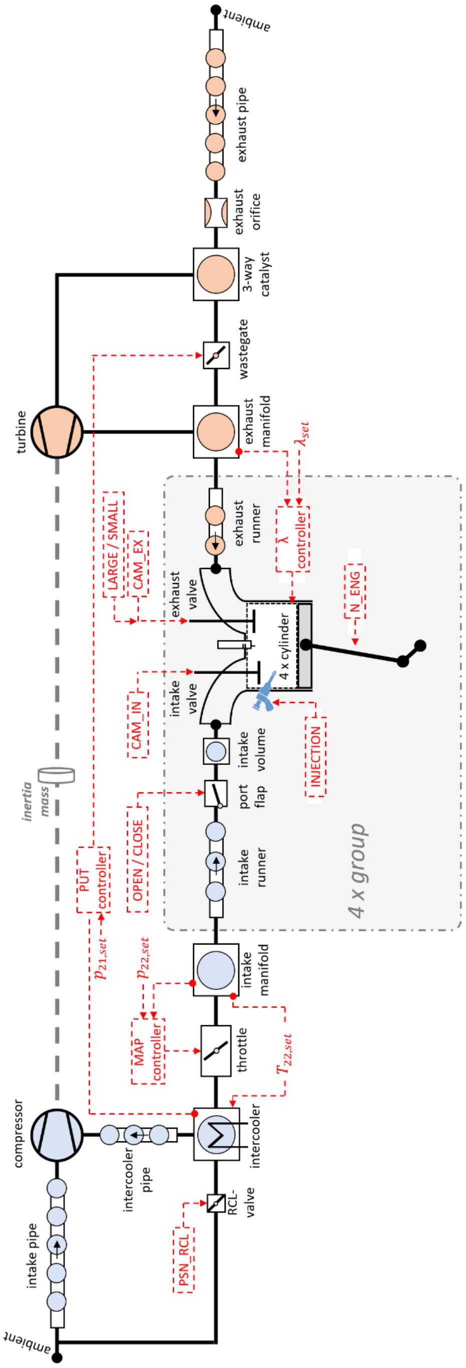

Fig. 79 Layout of detailed 1D model (238 ODEs, ∆t=30µs, RT=43, RMSE=5.3%err)

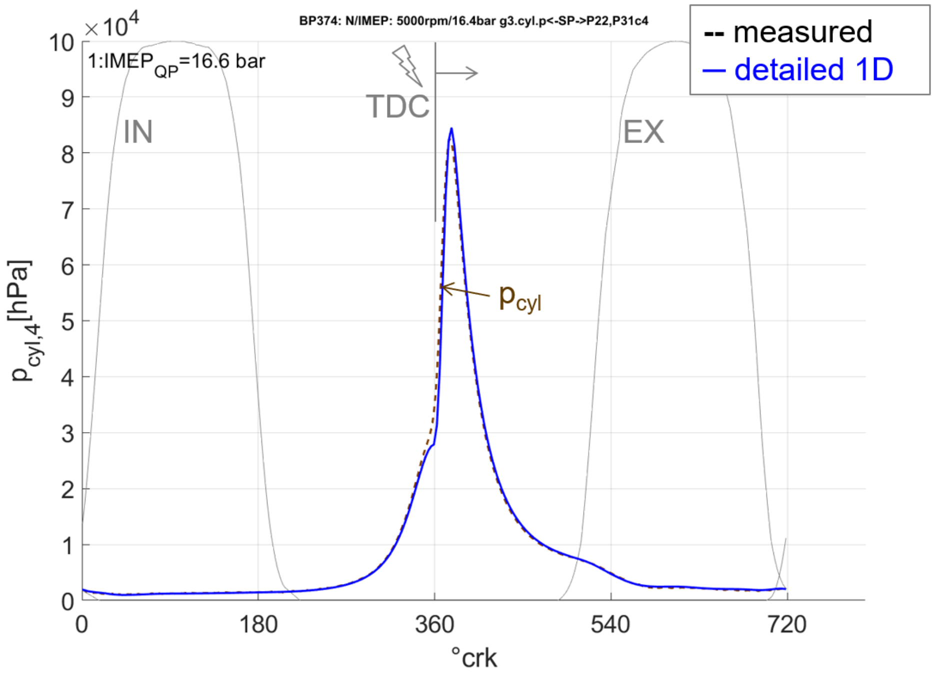

Fig. 80 Cylinder pressure of detailed 1D model compared to data from high-pressure indication system (M1: 234 ODEs, Δt=30µs, RT=41, RMSE=5.3%err)

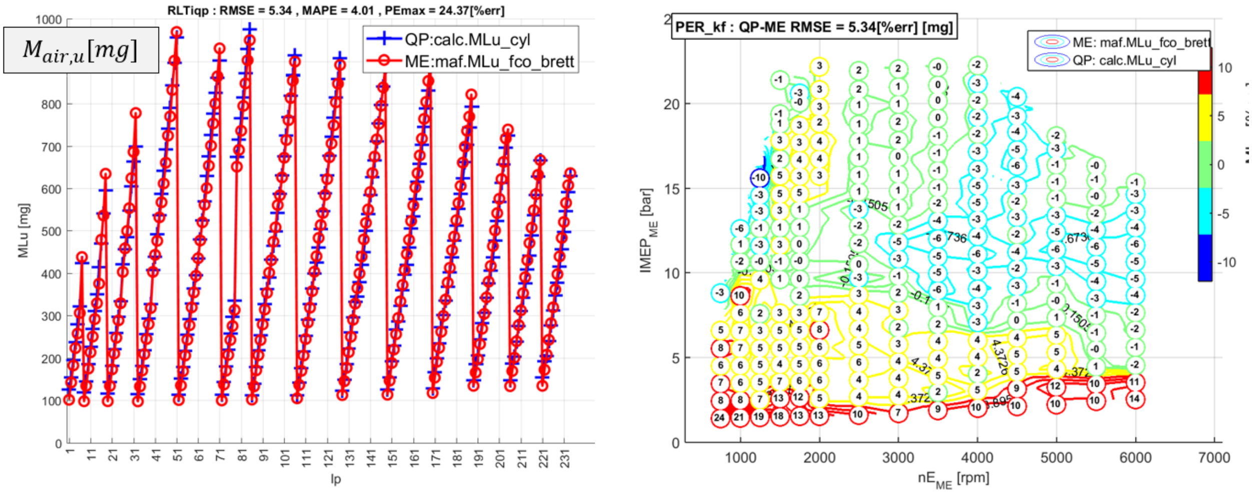

Fig. 81 Model deviation of cylinder trapped fresh air-mass compared to measurements (Model M1, RMSE($M_{Air,unburned}$) = 5.3%err)

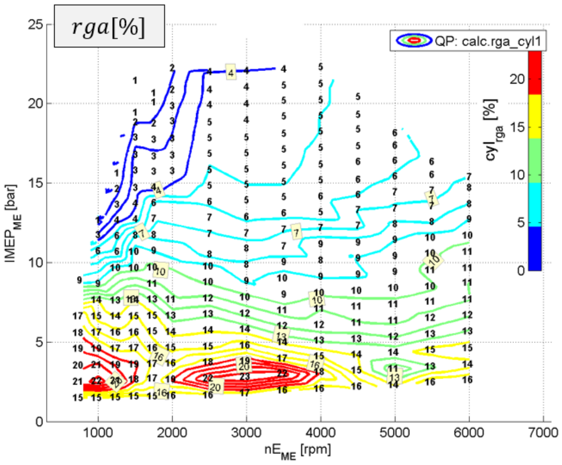

Fig. 82 Model cylinder residual gas fraction - no measurement available (Model M4)

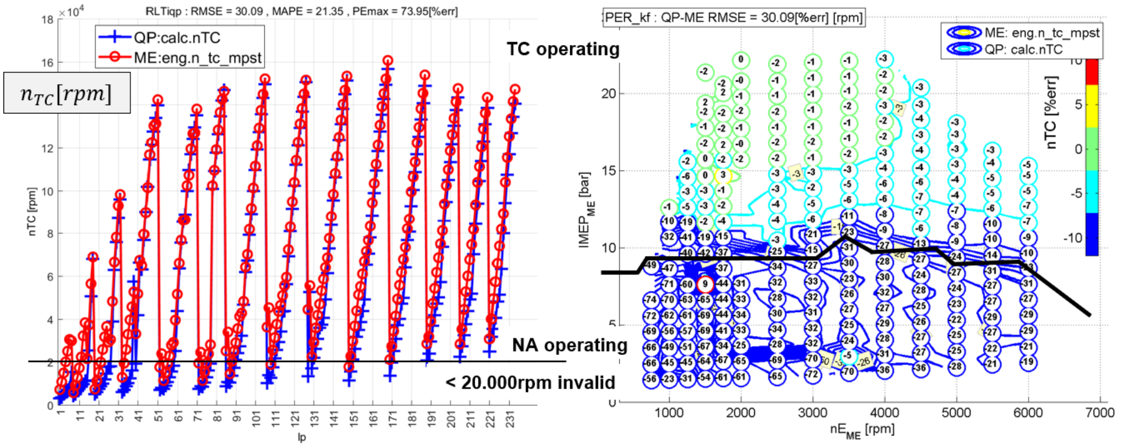

Fig. 83 Model deviation of turbocharger shaft speed compared to measurements (Model M1, RMSE(n_{TC}) = ca. 5%err @TC and 30% to 56% @NA)

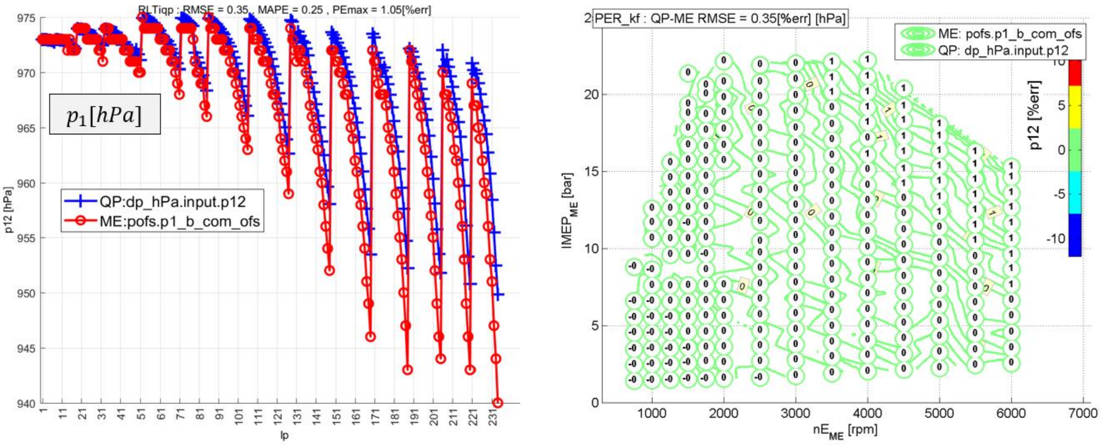

Fig. 84 Model deviation of air filter outlet average pressure (compressor upstream) compared to measurements (Model M1, RMSE(p_1) = 0.3%err)

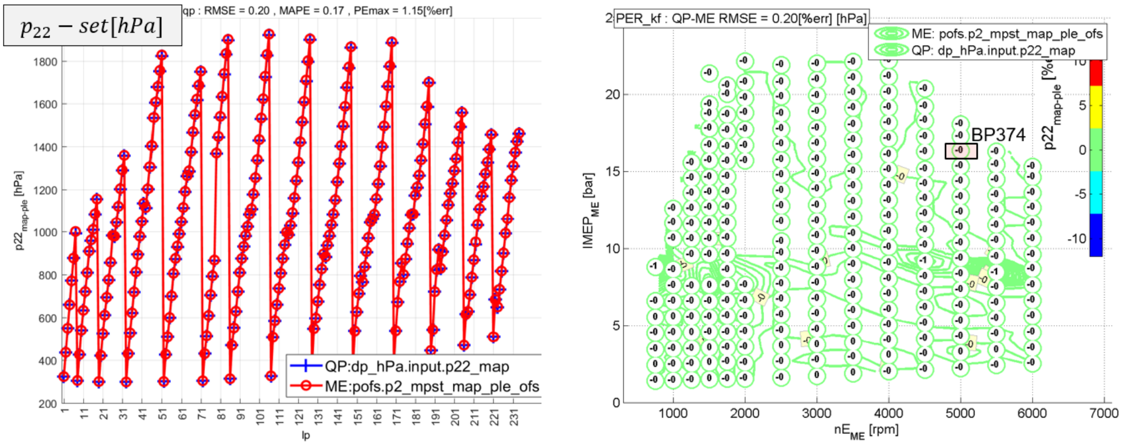

Fig. 85 Model deviation of manifold average setpoint pressure (downstream throttle) compared to measurements (Model M1, RMSE(p_{22}-set) = 0.2%err)

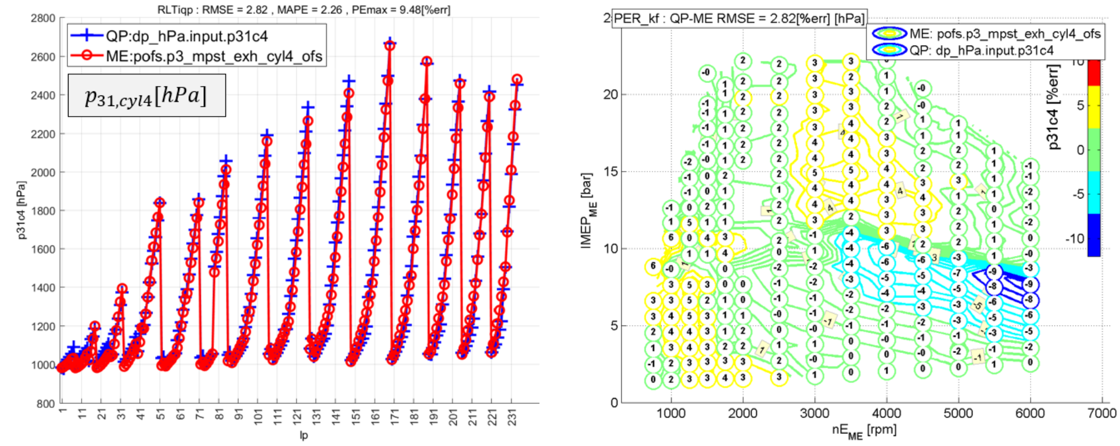

Fig. 86 Model deviation of exhaust runner average pressure, outlet cylinder 4 compared to measurements (Model M1, RMSE($p_{31,cyl4}$) = 2.8%err)

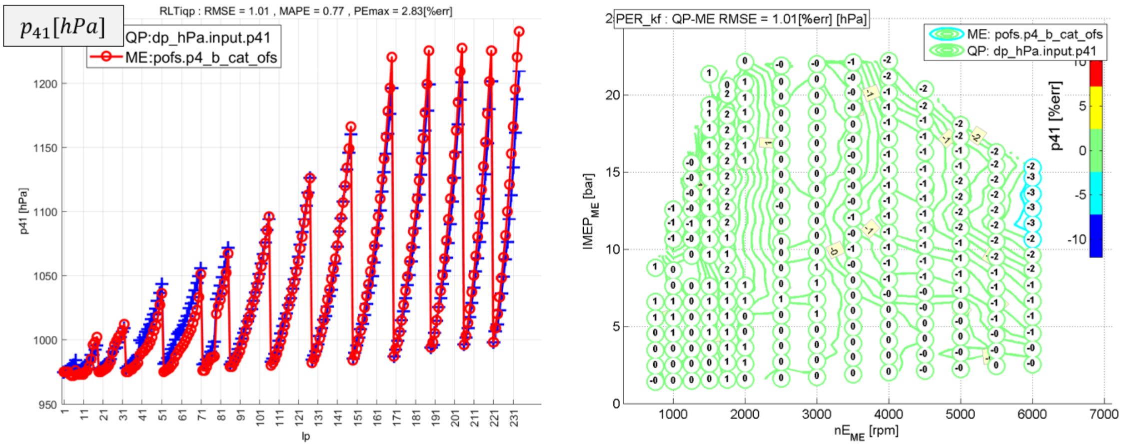

Fig. 87 Model deviation of turbine outlet average pressure (catalyst upstream) compared to measurements (Model M1, RMSE(p_{41}) = 1.0%err)

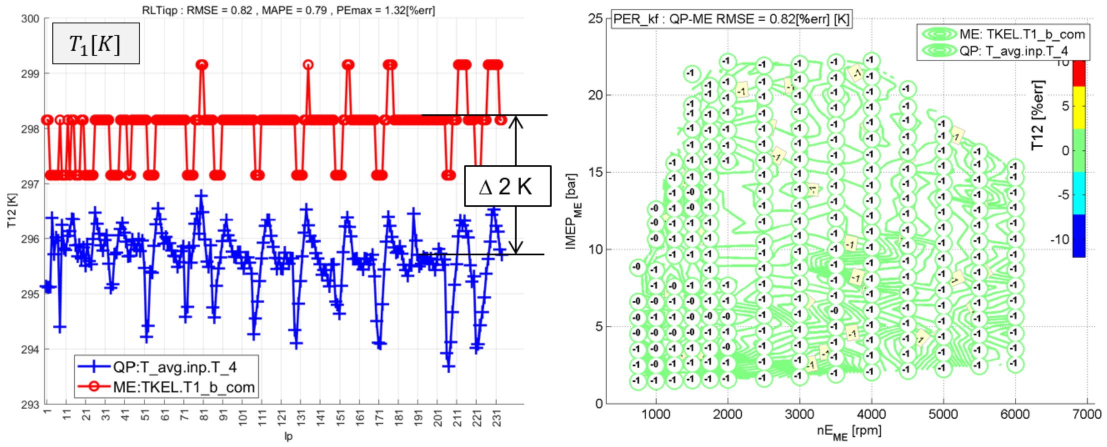

Fig. 88 Model deviation of air filter outlet time averaged temperature (compressor upstream) compared to measurements (Model M1, RMSE(T_1) = 0.8%err)

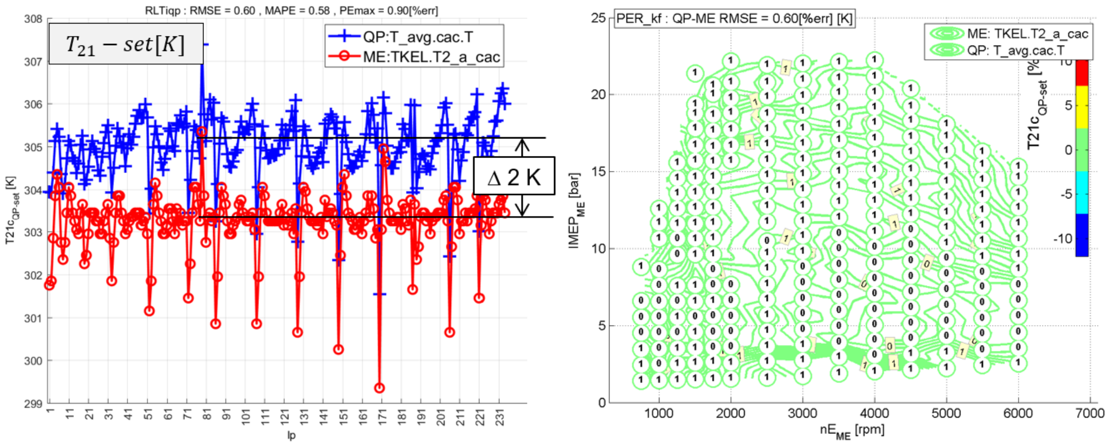

Fig. 89 Model deviation of charge air cooler outlet temperature compared to measurements (Model M1, RMSE(T_{21}) = 0.6%err)

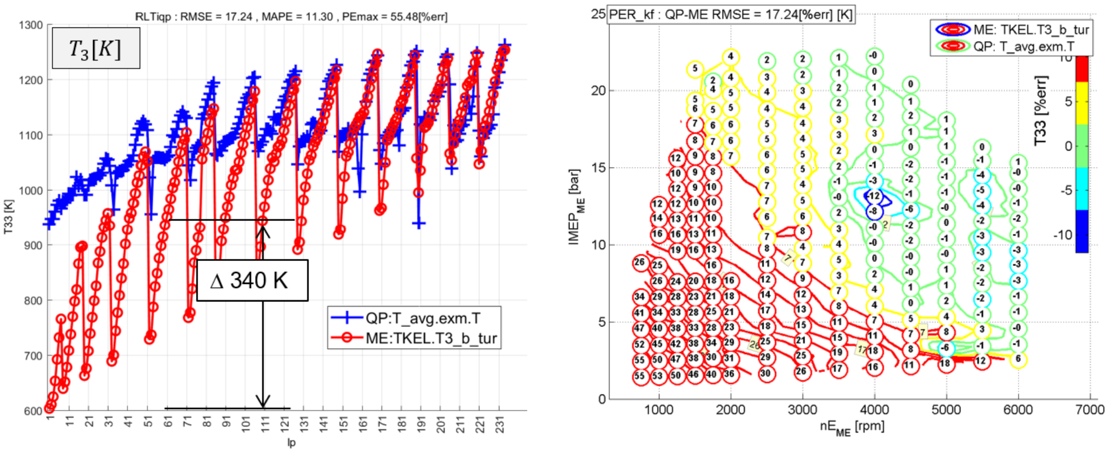

Fig. 90 Model deviation of exhaust manifold time averaged temperature (turbine inlet) compared to measurements (Model M1, RMSE(T_3) = 17%err)

…

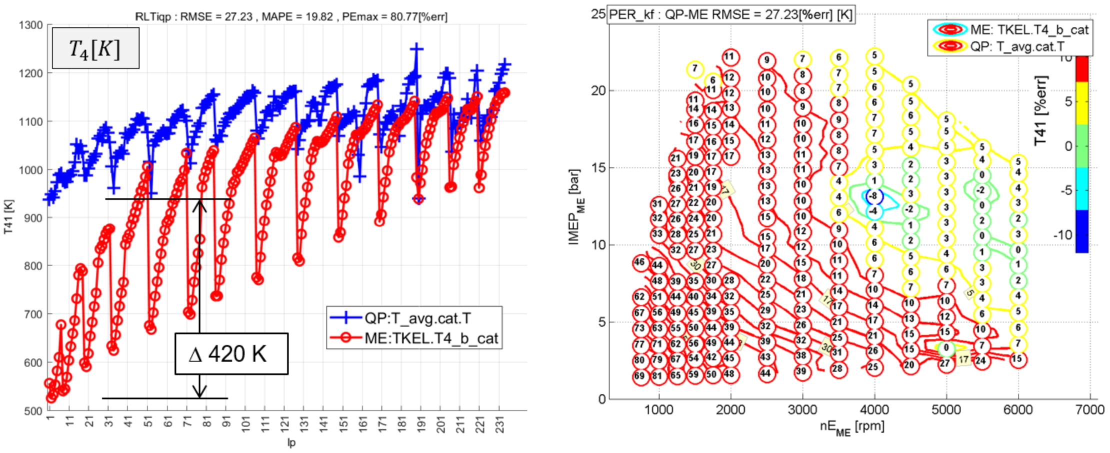

Fig. 91 Model deviation of turbine outlet time averaged temperature (catalyst upstream) to measurements (Model M1, RMSE(T_4) = 27%err)

4 Appendix – ODEs / CPU Load by Components

Model comparison – number of solved differential equations for each component					
	M1: Σ234 ODEs	**M2: Σ190 ODEs**	**M3: Σ69 ODEs**	**M4: Σ44 ODEs**	**M4a): Σ26 ODEs**
intercooler	4	4	4	4	4
intake manifold	4	4	4	4	4
intake volume (4x)	16	16	16	0	0
exhaust manifold	4	4	4	4	4
catalyst	4	0	4	0	0
cylinder (4x)	16	16	16	16	4
RCL-valve	1	1	1	1	1
throttle	1	1	1	1	1
port flap (4x)	4	4	4	0	0
intake (4x)	4	4	4	4	1
exhaust (4x)	4	4	4	4	1
wastegate	1	1	1	1	1
exhaust orifice	1	0	1	0	0
mass	2	2	2	2	2
turbine	0	0	0	0	0
compressor	1	1	1	1	1
intake pipe	25	25	0	0	0
intercooler pipe	15	15	0	0	0
intake runner (4x)	60	60	0	0	0
exhaust runner (4x)	40	16	0	0	0
exhaust pipe	25	10	0	0	0
lookup IN/EX (8x)	0	0	0	0	0
PIController PUT/MAP (2x)	2	2	2	2	2
gain (13x)	0	0	0	0	0
add (11x)	0	0	0	0	0
	Real-time factor on target ECU (240MHz)				
CPU 240MHz, Δt=30µs	**RT=41**	RT=27	RT=17	RT=11	RT=6
CPU 240MHz, Δt=40µs	instable	**RT=20**	RT=13	RT=8	RT=5
CPU 240MHz, Δt=300µs	instable	instable	**RT=1.7**	**RT=1.1**	**RT a)=0.6**
	Assumptions for extrapolation of real-time factor				
a) M4: Σ26ODEs	Calculate only first cylinder with ODEs, last 3 cylinders are assumed as a time-delayed signal of the first cylinder				

Tab. 9 Overview of resulting real-time factors in dependence on the number of solved differential equations in the models

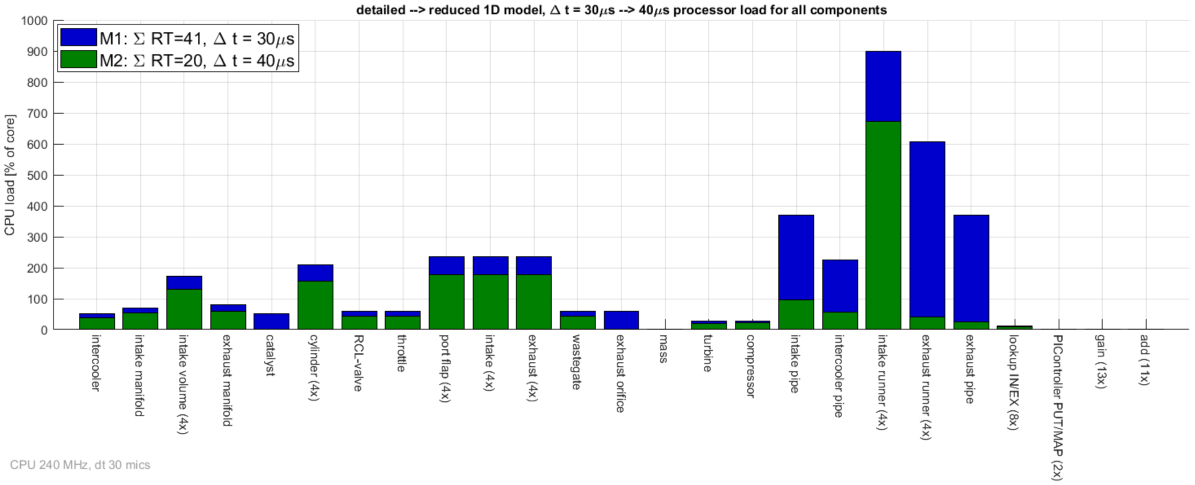

Fig. 92 Comparison of offline estimated processor load of detailed 1D model (M1: 234 ODEs, Δt=30μs, RT=41, RMSE=5.3%err) with reduced 1D model (M2: 190 ODEs, Δt=40μs, RT=20, RMSE=5.2%err) for each model component

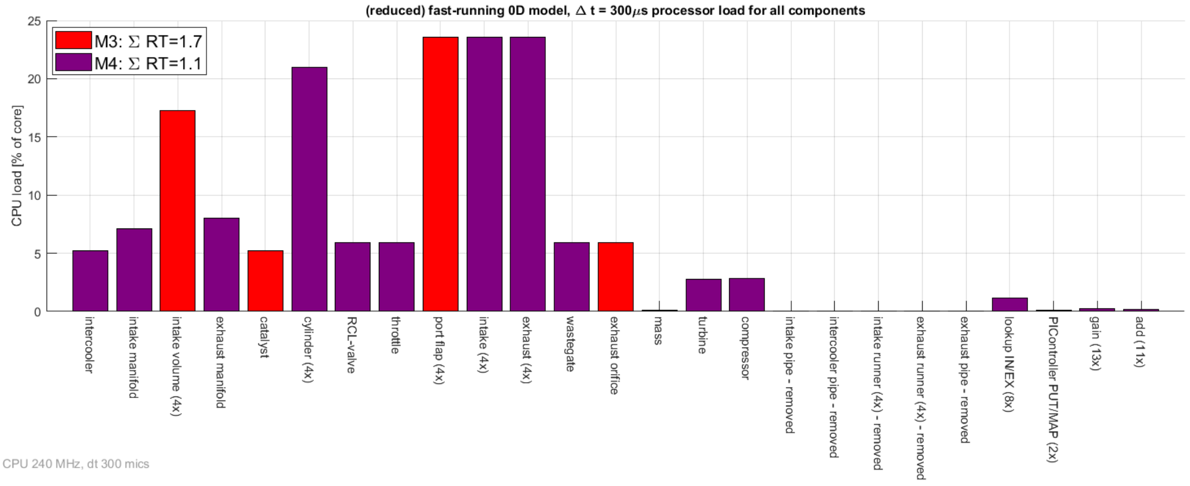

Fig. 93 Comparison of offline estimated processor load of fast-running 0D model (M3: 69 ODEs, Δt=300μs, RT=1.7, RMSE=7.4%err) with reduced fast-running 0D model (M4: 44 ODEs, Δt=300μs, RT=1.1, RMSE=7.4%err) for each model component